



**TECHNIQUES FOR REDUCED ORDER MODELING OF AEROELASTIC
STRUCTURES WITH DEFORMING GRIDS**

DISSERTATION

John S.R. Anttonen, Major, USAF

AFIT/DS/ENY/01-01

**DEPARTMENT OF THE AIR FORCE
AIR UNIVERSITY**

AIR FORCE INSTITUTE OF TECHNOLOGY

Wright-Patterson Air Force Base, Ohio

APPROVED FOR PUBLIC RELEASE; DISTRIBUTION UNLIMITED

Report Documentation Page

Report Date 9 Nov 2001	Report Type Final	Dates Covered (from... to) 01 Sep 1999 - 01 Oct 2001
Title and Subtitle Techniques for Reduced Order Modeling of Aeolastic Structures with Deforming Grids	Contract Number	
	Grant Number	
	Program Element Number	
Author(s) Major John Anttonen	Project Number	
	Task Number	
	Work Unit Number	
Performing Organization Name(s) and Address(es) Air Force Institute of Technology AFIT/ENY 2950 P Street, Bldg 640 Wright-Patterson AFB, OH 45433-7765	Performing Organization Report Number AFIT/DS/ENY/01-01	
Sponsoring/Monitoring Agency Name(s) and Address(es) Air Force Research Laboratory AFRL/VSD 2210 8th Street, Bldg 146 Wright-Patterson AFB, OH 45433-7531	Sponsor/Monitor's Acronym(s) AFRL/VASD	
	Sponsor/Monitor's Report Number(s)	
Distribution/Availability Statement Approved for public release, distribution unlimited		
Supplementary Notes		
Abstract Reduced order modeling (ROM) seeks to make the modeling of aeroelastic behavior practical by reducing computation time for design codes. Deforming grids are often used in aeroelastic problems to account for the deformation of the structure. Proper Orthogonal Decomposition (POD/ROM) is a ROM technique that operates in an index-space for computations, not accounting for changes in grid dynamics, and must be modified to reflect grid deformation properly. To investigate and account for the effects of grid deformation on POD/ROM, a new algorithm is developed that incorporates modifications to the usual formulation. Evaluation of the new algorithm is accomplished through application to three fluid-structure models, each adding an increased level of grid dynamics. Deforming grid POD/ROMs are found to require more modes for an accurate solution than POD/ROM for rigidly moving grids. In addition, for deforming grids, POD/ROMs are less accurate when the grid deformation is significantly altered from the deformations seen in the development of the POD/ROM. A technique, called Multi-POD, is developed that evaluates the relative grid motion between how the POD/ROM is created and how it is executed. The Multi-POD technique determines the current relative grid deformation and selects the best POD/ROM from those available.		

Subject Terms Proper Orthogonal Decomposition, POD, Reduced Order Modeling, ROM, POD/ROM, Deforming Grids	
Report Classification unclassified	Classification of this page unclassified
Classification of Abstract unclassified	Limitation of Abstract UU
Number of Pages 157	

AFIT/DS/ENY/01-01

TECHNIQUES FOR REDUCED ORDER
MODELING OF AEROELASTIC STRUCTURES
WITH DEFORMING GRIDS

DISSERTATION
John S. R. Anttonen
Major, USAF

AFIT/DS/ENY/01-01

Approved for public release; distribution unlimited

Report Documentation Page

Report Date 9 Nov 2001	Report Type Final	Dates Covered (from... to) 01 Sep 1999 - 01 Oct 2001
Title and Subtitle Techniques for Reduced Order Modeling of Aeolastic Structures with Deforming Grids	Contract Number	
	Grant Number	
	Program Element Number	
Author(s) Major John Anttonen	Project Number	
	Task Number	
	Work Unit Number	
Performing Organization Name(s) and Address(es) Air Force Institute of Technology AFIT/ENY 2950 P Street, Bldg 640 Wright-Patterson AFB, OH 45433-7765	Performing Organization Report Number AFIT/DS/ENY/01-01	
Sponsoring/Monitoring Agency Name(s) and Address(es) Air Force Research Laboratory AFRL/VSD 2210 8th Street, Bldg 146 Wright-Patterson AFB, OH 45433-7531	Sponsor/Monitor's Acronym(s) AFRL/VASD	
	Sponsor/Monitor's Report Number(s)	
Distribution/Availability Statement Approved for public release, distribution unlimited		
Supplementary Notes		
Abstract Reduced order modeling (ROM) seeks to make the modeling of aeroelastic behavior practical by reducing computation time for design codes. Deforming grids are often used in aeroelastic problems to account for the deformation of the structure. Proper Orthogonal Decomposition (POD/ROM) is a ROM technique that operates in an index-space for computations, not accounting for changes in grid dynamics, and must be modified to reflect grid deformation properly. To investigate and account for the effects of grid deformation on POD/ROM, a new algorithm is developed that incorporates modifications to the usual formulation. Evaluation of the new algorithm is accomplished through application to three fluid-structure models, each adding an increased level of grid dynamics. Deforming grid POD/ROMs are found to require more modes for an accurate solution than POD/ROM for rigidly moving grids. In addition, for deforming grids, POD/ROMs are less accurate when the grid deformation is significantly altered from the deformations seen in the development of the POD/ROM. A technique, called Multi-POD, is developed that evaluates the relative grid motion between how the POD/ROM is created and how it is executed. The Multi-POD technique determines the current relative grid deformation and selects the best POD/ROM from those available.		

Subject Terms Proper Orthogonal Decomposition, POD, Reduced Order Modeling, ROM, POD/ROM, Deforming Grids	
Report Classification unclassified	Classification of this page unclassified
Classification of Abstract unclassified	Limitation of Abstract UU
Number of Pages 157	

The views expressed in this dissertation are those of the author and do not reflect the official policy or position of the Department of Defense or the United States Government.

AFIT/DS/ENY/01-01

TECHNIQUES FOR REDUCED ORDER
MODELING OF AEROELASTIC STRUCTURES
WITH DEFORMING GRIDS

DISSERTATION

Presented to the Faculty of the School of Engineering
of the Air Force Institute of Technology

Air University

In Partial Fulfillment of the
Requirements for the Degree of
Doctor of Philosophy

John S. R. Anttonen, B.S., M.S., PE

Major, USAF

October, 2001

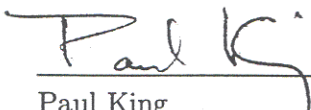
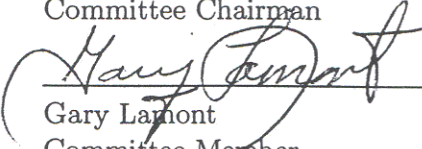
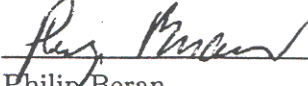
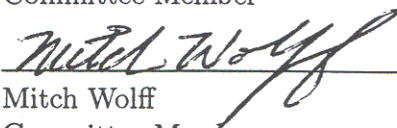
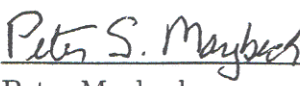
Approved for public release; distribution unlimited


TECHNIQUES FOR REDUCED ORDER
MODELING OF AEROELASTIC STRUCTURES
WITH DEFORMING GRIDS

John S. R. Anttonen, B.S., M.S., PE

Major, USAF

Approved:

	<u>10/11/01</u>
Paul King Committee Chairman	Date
	<u>10/11/01</u>
Gary Lamont Committee Member	Date
	<u>10/11/01</u>
Philip Beran Committee Member	Date
	<u>10/11/01</u>
Mitch Wolff Committee Member	Date
	<u>10/11/01</u>
Peter Maybeck Dean's Representative	Date



Robert A. Calico, Jr
Dean

Acknowledgements

I would like to express my sincere appreciation to my faculty advisor, Dr. Paul King, and to my research advisor, Dr. Philip Beran, for their guidance and support throughout the course of my research.

I would like to acknowledge the gang in the Ph.D. Bullpen for their support, humor, and laughter. A special thanks goes to Maj. David Lucia and Lt. Col. Ray Maple for their invaluable technical help in this work.

I would like to thank my father for his example and my mother for teaching me to love learning. Finally, I dedicate this work to my wife and two children, without whom I would never have attempted, much less succeeded.

John S. R. Anttonen

Table of Contents

	Page
Acknowledgements	iii
List of Figures	viii
List of Tables	xii
List of Abbreviations	xiii
List of Symbols	xiv
Abstract	xvi
I. Introduction	1-1
1.1 Research Objective	1-4
1.1.1 Thesis	1-7
1.1.2 Approach	1-8
1.1.3 Research Questions	1-8
1.2 Contribution	1-9
1.3 Document Organization	1-9
II. Proper Orthogonal Decomposition	2-1
2.1 Full-Potential Equation	2-3
2.2 POD Implementation with Potential Equation	2-4
III. Deforming Grid Error Estimation	3-1
3.1 Qualitative Error Estimate	3-1
3.2 Deforming Grid Metric	3-1

	Page
IV. Oscillating Panel	4-1
4.1 Application	4-1
4.1.1 Boundary Conditions	4-3
4.1.2 Full-Order Results	4-4
4.2 POD/ROM Results	4-5
4.2.1 Individual POD/ROM	4-8
4.2.2 Blended POD/ROM	4-24
4.2.3 Amplitude Variation	4-27
4.3 Multi-POD	4-29
4.4 Conclusions	4-30
V. Pitching and Plunging Airfoil	5-1
5.1 Application	5-1
5.1.1 Forced Oscillation Case	5-1
5.1.2 Free Pitch and Plunge Case	5-2
5.1.3 Computational Grid	5-4
5.1.4 Domain Filtering	5-4
5.1.5 Full-Order Results for Forced Oscillation	5-7
5.2 POD/ROM Results	5-8
5.2.1 Individual POD/ROM	5-8
5.2.2 Blended POD/ROM	5-13
5.2.3 Multi-POD	5-18
5.3 Conclusions	5-23
VI. Summary	6-1
6.1 Significant Advances	6-2
6.1.1 Static vs. Deforming Grid POD/ROM Analysis	6-2
6.1.2 Multi-POD	6-3

	Page
6.1.3 Application to Aeroelastic Problem	6-3
6.2 Future Work	6-3
Bibliography	BIB-1
Appendix A. Potential Flow Around a Translating Cylinder	A-1
A.1 Model Problem	A-1
A.2 Results	A-4
A.2.1 Rigid Grid Case	A-4
A.2.2 Deforming Grid Case	A-5
A.2.3 Grid Density	A-11
A.3 Conclusions	A-12
Appendix B. Proper Orthogonal Decomposition Theory	B-1
B.1 Derivation	B-1
B.2 Discretized Sample Spaces	B-4
B.3 Optimality	B-5
B.4 Method of Snapshots	B-6
Appendix C. Full-Potential Equation	C-1
C.1 Treatment of $\left(\frac{\rho}{J}\right)_\tau$	C-2
C.2 Treatment of $\left(\frac{\rho U}{J}\right)_\xi$	C-4
C.3 Treatment of $\left(\frac{\rho V}{J}\right)_\eta$	C-6
C.4 Summary of Solution $\left(\frac{\rho}{J}\right)_\tau + \left(\frac{\rho U}{J}\right)_\xi + \left(\frac{\rho V}{J}\right)_\eta = 0$	C-6
C.5 Approximate Factorization	C-7
C.6 Boundary Conditions	C-8
C.6.1 Far-Field	C-8
C.6.2 Body	C-9

	Page
C.6.3 Unsteady Wake	C-10
C.7 Density Biasing	C-11
Appendix D. Validation	D-1
D.1 Steady Flow	D-1
D.2 Unsteady Flow	D-2
D.3 Structural Model	D-4
Appendix E. Pitching and Plunging Airfoil Mode Shapes	E-1
Appendix F. Summary of Computational Runs	F-1
Vita	VITA-1

List of Figures

Figure		Page
1.1.	POD Eigenvalue Magnitude	1-5
1.2.	Contours of Potential Variable (Rigidly Attached Grid)	1-6
1.3.	Contours of Potential Variable (Deforming Grid)	1-7
3.1.	Deforming Grid Domains	3-4
4.1.	Model Problem	4-2
4.2.	Computational Grids	4-3
4.3.	Minimum C_N (full-system)	4-5
4.4.	Pressure Contours for Full-system (part 1, single oscillation)	4-6
4.5.	Pressure Contours for Full-system (part 2, single oscillation)	4-7
4.6.	POD/ROM/RG Modes	4-9
4.7.	POD/ROM/RG Modal Contribution	4-10
4.8.	POD/ROM/RG vs. Full-Order Solution Pressure Contours (part 1) ($f = 0.1, A = 0.1$)	4-11
4.9.	POD/ROM/RG vs. Full-Order Solution (part 2) ($f = 0.1, A = 0.1$)	4-12
4.10.	Minimum C_N (Individual POD/ROM/DG, 15 modes)	4-13
4.11.	POD/ROM/DG vs. Full-Order Solution Pressure Contour (part 1) ($f = 0.1, A = 0.1$)	4-14
4.12.	POD/ROM/DG vs. Full-Order Solution Pressure Contour (part 2) ($f = 0.1, A = 0.1$)	4-15
4.13.	POD/ROM/DG vs. Full-Order Solution Pressure Contour (part 1) ($f = 0.5, A = 0.1$)	4-16
4.14.	POD/ROM/DG vs. Full-Order Solution Pressure Contour (part 2) ($f = 0.5, A = 0.1$)	4-17
4.15.	POD/ROM/DG vs. Full-Order Solution Pressure Contour (part 1) ($f = 1.0, A = 0.1$)	4-18

Figure		Page
4.16.	POD/ROM/DG vs. Full-Order Solution Pressure Contour (part 2) ($f = 1.0$, $A = 0.1$)	4-19
4.17.	POD/ROM/DG Modes ($f = 0.1$, $A = 0.1$)	4-20
4.18.	POD/ROM/DG Modes ($f = 0.5$, $A = 0.1$)	4-21
4.19.	POD/ROM/DG Modes ($f = 1.0$, $A = 0.1$)	4-22
4.20.	POD/ROM/DG Modal Contribution	4-23
4.21.	Maximum Density Error ($A = 0.1$, 0.1 hz)	4-24
4.22.	Minimum C_N (Blended POD, trained at $A = 0.1$, run at $A = 0.1$, 15 modes)	4-25
4.23.	POD/ROM/B10 (Blended, $A = 1.0$)	4-26
4.24.	POD/ROM/B10 Modal Contribution	4-27
4.25.	Minimum C_N (Blended POD, trained at $A = 0.1$, run at $A = 0.05$, 15 modes)	4-28
4.26.	Minimum C_N (Blended POD, trained at $A = 0.1$, run at $A = 0.15$, 15 modes)	4-28
4.27.	Corrolated Grid Error and Density Error, after 8 oscillations (Blended POD, trained at $A = 0.1$, run at $A = 0.15$, 15 modes)	4-30
4.28.	Multi-POD (Two POD; trained at $A = 0.1$ and $A = 0.15$, 15 modes)	4-31
5.1.	Pitching and Plunging Airfoil Model Problem	5-2
5.2.	Pitching and Plunging 2-D System	5-2
5.3.	C-Grid	5-5
5.4.	Example of Grid Deformation ($h_{\max} = 0.1$, $a_{\max} = 2.0$ deg)	5-6
5.5.	Grid Domains	5-7
5.6.	Full-Order (Fixed Plunge, Varying Pitch)	5-9
5.7.	Full-Order (Varying Plunge, Fixed Pitch)	5-10
5.8.	Individual POD/ROM (Fixed Plunge, Varing Pitch, 20 modes) . .	5-11
5.9.	Individual POD/ROM (Varying Plunge, Fixed Pitch, 20 modes) . .	5-12
5.10.	Individual POD/ROM Modes ($h_{\max} = 0\%$, $\alpha_{\max} = 1.0$ deg, $f = 0.02$)	5-14

Figure		Page
5.11.	Individual POD/ROM Modes ($h_{\max} = 0\%$, $\alpha_{\max} = 1.0$ deg, $f = 0.1$)	5-14
5.12.	Individual POD/ROM Modal Contributions	5-15
5.13.	Blended POD/ROM (Fixed Plunge, Varying Pitch, 25 Modes) . . .	5-16
5.14.	Blended POD/ROM (Trained at $h = 0\%$, Run at $h = 10\%$, $f = 0.06$, $a = 1.0$ deg, 25 modes)	5-17
5.15.	Blended POD/ROM Accuracy vs. Number of Modes	5-17
5.16.	Blended POD/ROM Modes ($h_{\max} = 0\%$)	5-19
5.17.	Blended POD/ROM Modes ($h_{\max} = 10\%$)	5-20
5.18.	Blended POD/ROM Modes ($h_{\max} = 20\%$)	5-21
5.19.	Blended POD/ROM Modal Contributions	5-22
5.20.	Multi-POD, Damped Case ($\bar{u} = 2.0$)	5-22
5.21.	Multi-POD, Unstable Case ($\bar{u} = 5.0$)	5-23
5.22.	Blended POD (Trained at $h_{\max} = 10\%$), Unstable Case ($\bar{u} = 5.0$) .	5-24
A.1.	Grid Cases for Translating Cylinder	A-2
A.2.	Grid Sub-Cases for Deformation	A-3
A.3.	POD/ROM/RG vs. Analytical Solution (Maximum value of Ψ , lines are identical)	A-4
A.4.	POD/ROM/RG Contours of Ψ	A-5
A.5.	Translating Grid Sub-Case POD/ROM/DG Modes	A-6
A.6.	POD/ROM Modal Contribution (Rigid and Deforming Grid Cases)	A-7
A.7.	Translating Grid Sub-Case POD/ROM/DG Contours of Ψ	A-7
A.8.	Rotating Sub-Case POD/ROM/DG Modes	A-9
A.9.	Rotating Grid Sub-Case POD/ROM/DG Contours of Ψ	A-10
A.10.	Translating/Rotating Sub-Case POD/ROM/DG Modes	A-14
A.11.	Translating/Rotating Grid Sub-Case POD/ROM/DG Contours of Ψ	A-15
A.12.	Max value of Stream Function by mode	A-15
A.13.	Max value of Stream Function by mode	A-16

Figure		Page
D.1.	Sub-Sonic Cases	D-3
D.2.	Trans-Sonic Cases	D-3
D.3.	Unsteady Case	D-4
D.4.	Flutter Onset	D-5
E.1.	Individual POD/ROM Modes ($h = 0, a = 1.0$ deg, $f = 0.02$, 20 modes)	E-2
E.2.	Individual POD/ROM Modes ($h = 0, a = 1.0$ deg, $f = 0.04$, 20 modes)	E-2
E.3.	Individual POD/ROM Modes ($h = 0, a = 1.0$ deg, $f = 0.06$, 20 modes)	E-3
E.4.	Individual POD/ROM Modes ($h = 0, a = 1.0$ deg, $f = 0.08$, 20 modes)	E-3
E.5.	Individual POD/ROM Modes ($h = 0, a = 1.0$ deg, $f = 0.1$, 20 modes)	E-4
E.6.	Individual POD/ROM Modes ($h = 0, a = 1.0$ deg, $f = 0.06$, 20 modes)	E-4
E.7.	Individual POD/ROM Modes ($h = 10, a = 1.0$ deg, $f = 0.06$, 20 modes)	E-5
E.8.	Individual POD/ROM Modes ($h = 20, a = 1.0$ deg, $f = 0.06$, 20 modes)	E-5
E.9.	Individual POD/ROM Modes ($h = 10, a = 0$ deg, $f = 0.06$, 20 modes)	E-6
E.10.	Individual POD/ROM Modes ($h = 10, a = 1.0$ deg, $f = 0.06$, 20 modes)	E-6
E.11.	Individual POD/ROM Modes ($h = 10, a = 2.0$ deg, $f = 0.06$, 20 modes)	E-7

List of Tables

Table		Page
4.1.	Effect on Error due to Grid Density	4-24
5.1.	PAPA Structural Model Parameters	5-4
5.2.	Computation Times vs. Number of Modes	5-15
A.1.	Maximum Percentage Error of Stream Function	A-11
A.2.	Effect on Error due to Mode Truncation	A-11
A.3.	Effect on Error due to Grid Density	A-11
D.1.	PAPA Structural Model Parameters For Validation	D-4
D.2.	Flutter Onset Cases	D-5
F.1.	Archived File Names and Descriptions	F-3

List of Abbreviations

AoA	Angle of Attack
CFD	Computational Fluid Dynamics
dof	Degrees of Freedom
LCO	Limit Cycle Oscillation
PAPA	Pitching and Plunging Airfoil
TBC	Transpiration Boundary Condition
POD	Proper Orthogonal Decomposition
ROM	Reduced-Order Model
POD/ROM	Reduced-Order Modeling via Proper Orthogonal Decomposition
POD/ROM/DG	POD/ROM on a Deforming Grid
POD/ROM/RG	POD/ROM on a Rigidly Attached Grid
POD/ROM/B	Blended POD/ROM

List of Symbols

POD Symbols

ϕ, Φ	POD function and POD modal matrix
Φ_G	Grid modal matrix
$\omega, \hat{\omega}$	Data variable and ROM variable
ν, V	Eigen-vector and eigenvector matrix
λ, Λ	Eigenvalue and eigenvalue matrix
S	Snapshot matrix
N, M	Number of snapshots and modes

Full Potential Equation Symbols

$\Psi, \hat{\Psi}$	Potential function variable and ROM variable
J	Jacobian
x, y	Grid point locations
t, τ	Time
L_ξ, L_η	Approximate factorization matrices
U, V	Contravariant fluid velocities
u, v	Fluid velocities (non-dimensional)
M_∞	Freestream Mach number
P	Pressure (non-dimensional)
q	Dynamic pressure (non-dimensional)
ρ	Density (non-dimensional)
Γ	Circulation
γ	Ratio of Specific Heats

Aerodynamic - Structural Symbols

C_N	Normal force coefficient
C_l	Lift coefficient

C_m	Moment coefficient
r, A	Panel deflection and maximum amplitude
h	Airfoil plunge
α	Airfoil pitch
f	Oscillation frequency
c, b	Chord and half chord
\bar{u}	Reduced velocity (non-dimensional) $\frac{U_\infty}{b\varpi_\alpha}$
U_∞	Freestream velocity (non-dimensional)
ζ_α, ζ_h	Pitch and Plunge damping ratios
ω_α, ω_h	Pitch and Plunge natural frequency
r_α	Radius of gyration $\frac{I}{m}$
μ_s	Mass ratio

Subscripts

∞	Freestream quantity
max	Peak quantity (magnitude)
ξ, η	Computational Coordinates
h, α	Plunge and Pitch

Abstract

Reduced order modeling (ROM) seeks to make the modeling of aeroelastic behavior practical by reducing computation time for design codes. Deforming grids are often used in aeroelastic problems to account for the deformation of the structure. Proper Orthogonal Decomposition (POD/ROM) is a ROM technique that operates in an index-space for computations, not accounting for changes in grid dynamics, and must be modified to reflect grid deformation properly. As a POD/ROM is developed, fluid dynamics modes are created based on the index relationship between grid points. The modes are then used to recreate the full-order solution. When the relationship between the grid point locations and the index space changes, the created modes are no longer valid because the new grid dynamics are not captured accurately. To investigate and account for the effects of grid deformation on POD/ROM, a new algorithm is developed that incorporates modifications to the usual formulation. Evaluation of the new algorithm is accomplished through application to three fluid-structure models, each adding an increased level of grid dynamics.

The first, an oscillating cylinder, incorporates an analytical potential flow solution as a full-order model. This model completely decouples the grid motion from the solution. Deforming grid POD/ROMs require more modes for an accurate solution than POD/ROM for rigidly moving grids. Degradation in POD/ROM accuracy in transforming the analytical solution to reduced order space is investigated and found to be due solely to grid deformation.

The second model problem, an oscillating panel in cross flow with discretized potential flow equations for the full-order solver, evaluates forced grid motion. This model couples the grid motion to the resulting fluid dynamics but does not couple the fluid dynamics back into the structural model. A POD/ROM of a static grid with a transpiration boundary is compared to a POD/ROM of a deforming grid. Deforming grid POD/ROMs are found to require more modes than static grid POD/ROMs for similar accuracy levels for this model problem. In addition, for deforming grids, POD/ROMs are less accurate

when the grid deformation is significantly altered from the deformations seen in the development of the POD/ROM. As a result, a Multi-POD technique has been developed that evaluates the relative grid motion between how the POD/ROM was created and how it is executed. The Multi-POD technique determines the current relative grid deformation and selects the best POD/ROM from those available.

Finally, Multi-POD is applied to a pitching and plunging airfoil with both forced and free dynamics. In the free dynamic case, the model fully links both structural (grid) dynamics and fluid dynamics. POD/ROMs are trained with forced grid deformation. In cases with free grid deformation, the Multi-POD technique is able to reproduce the free deformation solution very accurately, switching between POD/ROM as necessary.

TECHNIQUES FOR REDUCED ORDER MODELING OF AEROELASTIC STRUCTURES WITH DEFORMING GRIDS

I. Introduction

In the design of aerospace systems, designers and operators are looking for ways to computationally model prospective vehicle configurations quickly. Designers typically use low-fidelity models to generate vehicle designs rapidly, allowing the designer to evaluate a large number of design variations. As the design is finalized, the designer moves to more complete models. However, as increasing performance objectives drive designs to become more complex, the designer is faced with a dilemma: low-fidelity models cannot accurately model even the initial design variations. Higher fidelity models are desired, but are impractical for design due to their large computational expense in both time and hardware. To model a configuration fully, time integration with Computational Fluid Dynamics (CFD) is prohibitively expensive owing to the large number of degrees of freedom (dof) in the problem. Reduced-order modeling (ROM) is one means of developing higher fidelity models that are more efficient to solve, and therefore more attractive to designers. By reducing the dof (independent variables) of the problem, computational times can be decreased by orders of magnitude while still maintaining solution accuracy.

Modeling has two basic attributes: fidelity and complexity. Fidelity is a model's ability to predict the behavior of the system correctly. Sometimes called accuracy, it is a reflection of the degree to which the physics of the modeled system are described by the mathematics contained in the model. Complexity is how difficult the model is to generate and solve, often represented by the number of dof in the discretized, constituent equations. With the growing complexity of computational methods, model reduction has been studied for the analysis of very large problems. For problems with complicated physics, models with higher fidelity usually have a higher complexity. Model reduction seeks to produce an optimal trade-off between fidelity and complexity, producing a suitably

accurate model, while minimizing computational time. One such technique is Proper Orthogonal Decomposition (POD).

POD was introduced by multiple sources in the mid 1940's (1, 2). The concept has been applied in a wide variety of fields: fluid mechanics, uncertainty analysis, image processing, signal analysis, data compression, process identification and control in chemical engineering, and oceanography (3, 4, 5, 6, 7, 8, 9, 10, 11, 12). In its early development, POD was presented as a mathematical method of correlating statistical data (13, 14). Lumley (15) introduced the idea of applying POD to turbulent fluid flow in 1967 as a modeling technique. Reduced-Order Modeling via Proper Orthogonal Decomposition (POD/ROM) for turbulent modeling is still in use today (16). In its application for reduced order models, POD/ROM was based on earlier forms of eigenmode analysis. Using eigenmode analysis as a means of generating a reduced order model for fluid dynamics first appeared in the late 1980's and early 1990's. Dowell presented several papers on the development of eigenmode analysis for ROMs, and his work (17, 18, 19) represented a literature review of the subject area. Eigenmode analysis for ROM of fluid problems has been applied to several areas of interest: classic incompressible and potential flows, compressible potential flow, compressible Euler flow, and unsteady viscous flow. One of the initial papers of eigenmode analysis of classic incompressible and potential flows was presented by Hall (11) in 1994. Hall developed eigenmode based reduced order models for aerodynamic representation of inviscid, incompressible vortex-lattice models, to represent two and three dimensional flows about airfoils. Mahajan, Blahle, and Dowell (20) calculated the eigenvalues of an aeroelastic system modeled with the full-potential equation to investigate aeroelastic stability. Building on the above works, Romanowski and Dowell (21) generated the first successful generation of ROM's for linearized Euler flows and showed a definite improvement in calculation time for complex aeroelastic problems. Florea and Hall (22) then moved on to create reduced order models in the time domain for linearized potential flow about isolated airfoils. In 1999, Hall, Florea and Dowell employed the Lanczos procedure (23) to create a reduced order aerodynamic model in the frequency domain for linearized unsteady potential flows in turbomachinery. POD/ROM was used in 2001 by Thomas, Dowell and Hall for model problems in three dimensions (24).

POD/ROM is a spectral method using modes created by taking snapshots (time dependant data samples from CFD program or experiment, captured at increments in time and representing the dynamics of the fluid system) of the unsteady flow-field data. These snapshots are used to generate fluid modes using an eigen-problem method. If the snapshots sufficiently represent the fluid dynamics of the problem, the POD/ROM will be accurate. The results of POD/ROM could then be used to analyze similar, but not identical, conditions to the initial model. The range of accuracy around the original model represents the fidelity of the POD/ROM.

POD/ROM was first applied to aeroelastic problems in 1996 by Romanowski (25) as a means of generating the basis set for the linearized Euler equations. Dowell, Hall and Romanowski (19) used this implementation in the evaluation of a plunging and rotating airfoil. Later, Ly and Tran (26) used POD/ROM as a method of generating a Galerkin reduced order model for a chemical vapor deposition reactor, showing an efficient approximation of solution for compressible viscous flows coupled with energy and species equations. Iollo, Lanteri and Desideri also developed Galerkin approaches for solving viscous flows (27, 28). In 1999, Beran, Huttsell, Buxton, Noll, and Osswald (4) used POD/ROM to generate a reduced order model for the calculation of limit cycle oscillation of a convection-diffusion-reaction equation. In 2000 and 2001, Beran, Pettit and Mortara used POD/ROM for nonlinear panel response (29, 30). POD/ROM was also expanded to coupled fluids and flow control problems by Arian, Fahl, and Sachs (31).

In 2000, LeGresley and Alonso (32) used POD/ROM for the optimization of an airfoil design. This effort used mesh deformation with POD/ROM, though it did not specifically address it. An Euler solver was used to generate steady state snapshots for various airfoil shapes. A POD/ROM was developed from these snapshots and a least squares optimization used to change the airfoil shape based on input parameters to the POD/ROM. LeGresley and Alonso were able to change their airfoil shapes to meet new input parameters when the airfoil shape changes were small. However, they did not examine any aspect of the deforming grid, nor how it affected the accuracy and convergence properties of their POD/ROM.

1.1 *Research Objective*

The POD/ROM research discussed used either small deformation theory or rigid grids. It is the objective of this research to demonstrate how POD/ROM of fluid dynamics problems is affected in terms of efficiency and effectiveness by the use of deforming grids. Grid deformation is used in CFD to model a variety of moving boundary problems, such as dynamic interaction between airfoils and flaps, and deforming aeroelastic structures. POD/ROM computations are conducted in computational (or index) space and do not directly account for grid deformation. Snapshots taken of the flow-field data are arranged in column (index) form. The order of the data in the column is irrelevant to the process, but must be consistent. In any problem with a deforming grid, the physical location of any data point changes from one snapshot to the next, even though its location in the data column does not. This makes the deforming grid POD/ROM more complex than that of a static grid POD/ROM where the relationship between index space and the physical grid locations is fixed.

To examine this effect a model problem with a steady analytical solution is evaluated: the analytical solution of potential flow about a uniformly translating 2-D cylinder in still fluid (see Appendix A. for full model development). An analytical solution decouples the grid motion from the fluid dynamics. Two grid cases are selected. The first case is a rigid grid fixed to the cylinder and translating with it (no grid deformation). The second case has a fixed outer boundary and the grid is attached to the cylinder as it is translated and rotated within the boundary, causing grid deformation. For each grid case, POD/ROM is applied to snapshots of data obtained by imposing the analytical solution on the grids at selected increments in time. With the analytical solution decoupling the grid dynamics from the fluid dynamics, any difference in the POD/ROM of the two cases can be solely attributed to the grid deformation. The resulting modes created from the snapshots represent the differences in grid dynamics for the two cases. The relative contribution of each mode can be estimated by its percentage contribution to the total eigenvalue energy. This gives an idea of how important individual modes are to the overall POD/ROM solution.

The resulting POD/ROM of the two cases are significantly different. By plotting the modal contribution verses the number of modes, the relative importance of each mode

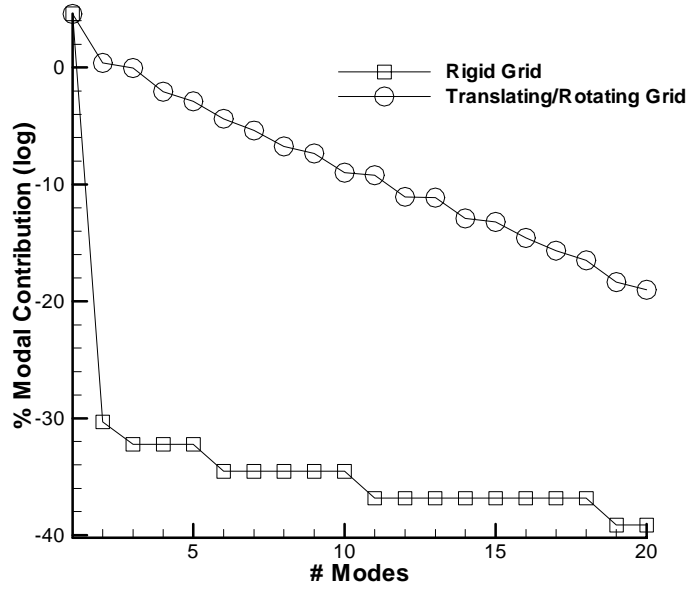
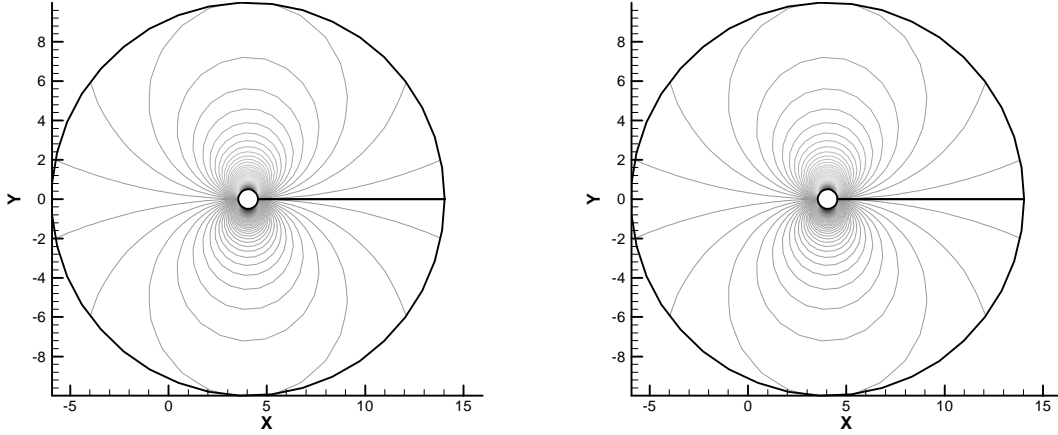


Figure 1.1 POD Eigenvalue Magnitude

can be determined. Differences in the slope of modal contribution verses number of modes highlight differences in POD/ROMs. If modal contribution drops quickly, only the initial modes are of significance. If the slope is more shallow, more modes are necessary for an accurate solution. The POD/ROM for the rigid grid, POD/ROM/RG, has a first mode with 100% of modal contribution (100% of the total energy of the eigenvalues) and the remaining modes are constrained by machine precision. This indicates that the ROM of the analytical solution on a rigid grid is exact. The POD/ROM for the deforming grid, POD/ROM/DG, has a first mode with 99.7% modal contribution. The remaining modes decrease in energy quickly, but are still significant compared to the non-dominant modes of the POD/ROM/RG (Fig. 1.1). Therefore, the POD/ROM/DG is not an exact ROM of the analytical solution. Additional modes are necessary for an accurate solution. By plotting contours of the stream function variable, Ψ , the analytical solution can be compared to the POD/ROM/RG solution. The POD/ROM/RG with one mode is exact (Fig. 1.2) when compared to the analytical solution. The single mode necessary for the POD/ROM/DG is a scalar percentage of the exact solution. The mode can be captured at any time increment



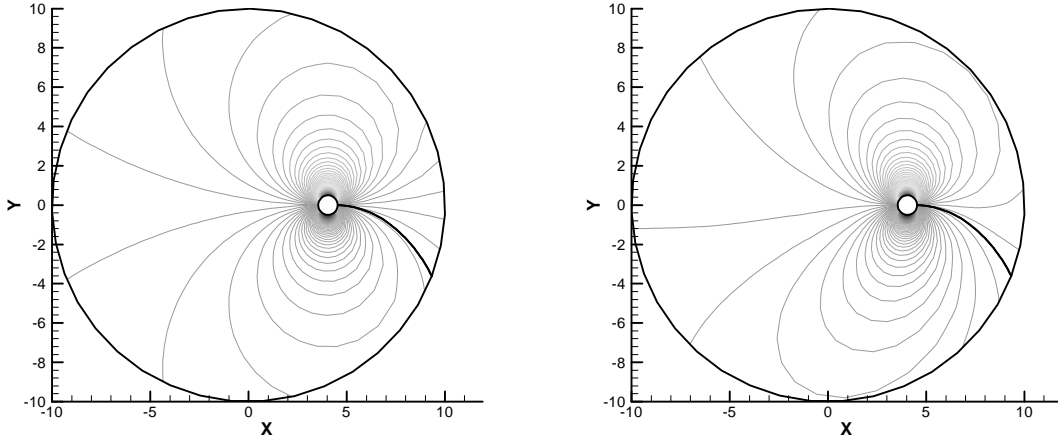
(a) Analytical Solution

(b) POD/ROM with 1 Mode

Figure 1.2 Contours of Potential Variable (Rigidly Attached Grid)

with a single snapshot. In contrast to the POD/ROM/RG, the POD/ROM/DG requires at least 7 modes for a 99% accurate solution. If fewer modes are used the POD/ROM/DG solution degrades. For contours of Ψ , a 4 mode POD/ROM/DG compares poorly to the analytical solution (Fig. 1.3). The principle mode is incorrectly mapped to the deformed grid and results in a skewed solution. The additional modes necessary for an accurate solution map the principle mode to the deformed grid. The additional modes necessary for a POD/ROM/DG over a POD/ROM/RG are solely caused by the addition of grid deformation.

To use a POD/ROM successfully in cases where the deforming grid interacts with the fluid dynamics, the magnitude of the increase in the error needs to be understood and quantified. The model problem described has the fluid dynamics decoupled from the grid motion, however, it clearly demonstrates that grid deformation affects the accuracy of POD/ROM in an analytical problem. In more realistic cases, the fluid dynamics and grid dynamics are coupled, such as in a pitching and plunging airfoil. The coupled nature of the dynamics precludes a simple method of evaluating the error due to the deforming grid.



(a) Analytical Solution

(b) POD/ROM With 4 Modes

Figure 1.3 Contours of Potential Variable (Deforming Grid)

However, the error resulting from a POD/ROM/DG may be estimated by comparing the results to a case for which the grid is static.

POD/ROM are typically accurate about some standard state. Parameters are varied about a standard state, such as angle of attack for an airfoil, and provide the POD/ROM/DG's range of accuracy. In a POD/ROM/DG, the grid deformation itself becomes a parameter. As the POD/ROM/DG is developed by collecting snapshots (called the training period), the modes created are based on the different grid states seen in those snapshots. To be robust, POD/ROM/DG must have some range of accuracy over variations in grid states seen in the snapshots during training. This adds an additional complexity to the creation of a POD/ROM/DG. If the POD/ROM/DG is applied to a grid state not included in the training set, regardless of whether the rest of the parameters are identical, the accuracy is affected. The magnitude of the allowable change in deformation defines the robustness of the POD/ROM/DG.

1.1.1 Thesis. The thesis of this dissertation is that *POD/ROM can be used to simulate fluid flows accurately on deforming grids.*

1.1.2 Approach. The research was decomposed into four steps. The first step was to evaluate POD/ROM with deforming grids, where the fluid solution was independent of the grid. Potential flow around a translating cylinder was selected because it had an analytical solution. This allowed a complete separation between fluid and grid dynamics.

The second step was to develop a ROM for the unsteady full-potential solver. The solver used was the Shankar (33) implicit scheme. The scheme was relatively simple code, allowing more attention to be focused on the deforming grid and its application to a POD/ROM. The POD/ROM implementation was based on the RAPOD computer program developed by Beran (4). RAPOD was modified for a fully implicit scheme based on the work of Dowell, Hall, etc. (34). The Shankar solver was validated using both steady and unsteady experimental data.

The third step was to analyze the effects of the deforming grid on the POD/ROM solution, where the grid dynamics would affect the fluid dynamics. The oscillating panel in cross flow was selected as the model problem. Analysis included comparison to a static grid POD/ROM as well as full-order solutions based on the full-potential solver. Techniques were explored to evaluate the robustness of POD/ROM based on changes in the grid deformation.

The fourth step was to examine a fully coupled structural and fluid dynamics problem. The pitching and plunging airfoil was chosen as a model problem and the techniques developed from the oscillating panel were applied to determine their effectiveness in this more general case. Finally, POD/ROM was tested for a practical problem of free pitch and plunge to determine its utility with deforming grid aeroelastic problems.

1.1.3 Research Questions. Several research questions are addressed in this work:

1. What decrease in accuracy can be expected solely due to the grid deformation for a POD/ROM?
2. What metric can be used to evaluate the accuracy of a POD/ROM on a deforming grid?

3. Can a POD/ROM constructed for a deforming grid be used for a grid with different deformation properties?

1.2 Contribution

The contribution of this research to the body of knowledge is in expanding the application of POD/ROM to a wider variety of problems via relevant model problems. This has been accomplished using a deforming grid that allows for the analysis of moving airfoils, flaps, and structures.

1.3 Document Organization

The remainder of this document is organized according to the approach described in Section 1.1.2. Chapter Two examines the application of Proper Orthogonal Decomposition to the CFD model chosen. Chapter Three looks at deforming grids and error estimation for POD/ROM. Chapters Four and Five address two application problems: the oscillating panel and the pitching and plunging airfoil. Chapter Six summarizes the research findings and provides ideas for future work. The appendices detail the translating cylinder model problem, the theoretical background on POD/ROM, and the derivation and validation of the flow solver.

II. Proper Orthogonal Decomposition

Proper Orthogonal Decomposition (POD), also known as Karhunen-Loève decomposition (1), is an empirical spectral method. Spectral methods use basis to approximate the full-order solution. The basis can be developed through a variety of techniques: trigonometric functions, polynomials, or wavelets for example. The basis is used to generate constant modes that are constant in space and are multiplied by coefficients that are time-dependent to create an expansion to the time-dependent, full-order solution. That is, if ω is a column array representing a set of N variables, it can be represented by a set of M modes, ϕ_m , and a set of reduced-order variables, $\hat{\omega}_m(t)$, such that

$$\omega(t) \approx \sum_{m=1}^M \hat{\omega}_m(t) \phi_m. \quad (2.1)$$

where $N \gg M$. It is the development of the modes, ϕ_m , that differentiates one spectral method from another.

In POD, the basis functions are created from a set of observed data, herein called snapshots. As a result, the POD basis can be made optimal in terms of minimizing the error in recreating the observed data (see Appendix B). This does not mean it will be the optimal basis for all, or even most, full-order cases, only for the snapshots from which the modes are developed. This is one of POD's weaknesses: to be accurate the snapshots must fully represent the dynamics of interest in the fluid model. For instance, data from a CFD model would need to reflect the complexity of the model problem and be complete enough to capture all relevant fluid structures, including non-linear effects. The creation of the snapshot is called the training period. The training period comes at a computational cost and the more complete the set of snapshots, the more expensive the training. However, if the snapshots are not complete the ROM will not be robust to changes in parameters that govern the system behavior. As Beran and Silva (35) noted in their development of POD, the trade-off can be favorable when, after the initial computational investment, a compact ROM can be constructed which can be used many times, and is valid over a useful range of system states. For deforming grid cases, the issue lies in creating a POD/ROM that is useful over a range of deformations.

In POD, the snapshots are linearly combined to form a smaller number of basis vectors. That is, for K snapshots of ω ,

$$\phi_m = \sum_{k=1}^K \omega_k \nu_m^k, \quad (2.2)$$

where ν_m^k is the contribution of the k th snapshot to the m th basis vector. In matrix form Eqn. 2.2 becomes,

$$\Phi = SV, \quad (2.3)$$

where,

$$\Phi = \begin{bmatrix} \uparrow & \uparrow & & \uparrow \\ \phi_1 & \phi_2 & \dots & \phi_m \\ \downarrow & \downarrow & & \downarrow \end{bmatrix}, \quad (2.4)$$

$$S = \begin{bmatrix} \uparrow & \uparrow & & \uparrow \\ \omega_1 & \omega_2 & \dots & \omega_m \\ \downarrow & \downarrow & & \downarrow \end{bmatrix}, \quad (2.5)$$

and

$$V = \begin{bmatrix} \uparrow & \uparrow & & \uparrow \\ v_1^k & v_2^k & \dots & v_m^k \\ \downarrow & \downarrow & & \downarrow \end{bmatrix}, \quad (2.6)$$

Φ is known as the modal matrix, an $(N \times M)$ matrix containing the functions ϕ_m . The snapshot matrix, S , is an $(N \times M)$ matrix containing M snapshots of $\omega(t)$, with the data stored as column vectors in the matrix. The transformation matrix, V , is the $(M \times M)$ matrix that maximizes the projection of the snapshot matrix onto the POD basis. V must be properly scaled to be orthonormal. This leads to the eigenproblem,

$$S^T S V = V \Lambda, \quad (2.7)$$

for eigenvectors, V , and eigenvalues, $\Lambda = \text{diag}(\lambda_m)$ (see Appendix B. for the full development of V). In practice, fewer modes are used than the total number of snapshots,

$M < K$. These are selected based on the relative size of the modal eigenvalues, λ_m , in a technique called truncating. Each eigenmode is normalized and compared to the sum total of all eigenmodes for its modal contribution.

2.1 Full-Potential Equation

The scope of the current work uses the full-potential equation for the governing equation (see Appendix C. for full development). The full-potential equation is an approximation to the Euler equations for which one assumes no rotation in the flow, and thus no entropy production (36). The potential equation has one fluid variable, Ψ , defined as,

$$u = \frac{\partial \Psi}{\partial x}, \quad (2.8)$$

$$v = \frac{\partial \Psi}{\partial y}. \quad (2.9)$$

where u and v are fluid velocities. In a 2-D, body-fitted coordinate system represented by $\tau = t$, $\xi = \xi(x, y, t)$, and $\eta = \eta(x, y, t)$, the unsteady full-potential equation is written as

$$\left(\frac{\rho}{J}\right)_\tau + \left(\frac{\rho U}{J}\right)_\xi + \left(\frac{\rho V}{J}\right)_\eta = 0, \quad (2.10)$$

where the $(R)_\xi$ refers to the derivative of R with respect to ξ . U and V are the contravariant velocities, J is the Jacobian of the metrics and the density, ρ , is represented as

$$\rho = \left\{ 1 - \frac{\gamma - 1}{2} M_\infty^2 [2\Psi_\tau + (U + \xi_\tau) \Psi_\xi + (V + \eta_\tau) \Psi_\eta - 1] \right\}^{\frac{1}{\gamma - 1}}. \quad (2.11)$$

The above equations can be solved by a variety of schemes. The scheme selected was developed by Shankar, et, al. (33) and has the benefit of being very stable and easy to implement with POD. It uses an implicit Newton's method to solve Eqn. 2.10 for a robust and efficient numerical solver with effective treatment of boundary conditions. In summary, the scheme is as follows; Eqn. 2.10 is represented as

$$F(\Psi) = 0, \quad (2.12)$$

where Ψ is the unknown to be solved for at every grid point in the domain for time step $(n + 1)$. The Newton iteration for the solution to Eqn. 2.12 is,

$$F(\Psi_*) + \left(\frac{\partial F}{\partial \Psi} \right)_{\Psi=\Psi_*} (\Psi - \Psi_*) = 0, \quad (2.13)$$

where Ψ_* is the current guess for Ψ at the $(n + 1)$ time step. At convergence, $\Delta\Psi = \Psi - \Psi_*$ will approach zero. The Jacobian matrix, $\left(\frac{\partial F}{\partial \Psi} \right)$, is large $(N \times N)$ but sparse and can be simplified using an approximate factorization creating two linear operators,

$$L_\xi = \left[1 + \Delta\tau U \frac{\partial}{\partial \xi} + \frac{1}{\beta} \frac{\rho}{J} a_{11} \frac{\partial}{\partial \xi} \right], \quad (2.14)$$

$$L_\eta = \left[1 + \Delta\tau V \frac{\partial}{\partial \eta} + \frac{1}{\beta} \frac{\rho}{J} a_{22} \frac{\partial}{\partial \eta} \right], \quad (2.15)$$

where $\beta = \left(\frac{\rho}{J \Delta\tau^2} \right)$, $a_{11} = \xi_x^2 + \xi_y^2$, and $a_{22} = \eta_x^2 + \eta_y^2$. L_ξ and L_η are $(N \times N)$ tridiagonal matrices. Eqn. 2.13 is then solved successive ξ and η sweeps

$$L_\xi L_\eta \Delta\Psi = R, \quad (2.16)$$

$$L_\xi \overline{\Delta\Psi} = R, \quad (2.17)$$

$$L_\eta \Delta\Psi = \overline{\Delta\Psi}, \quad (2.18)$$

where $\overline{\Delta\Psi}$ is an intermediate solution and $R = F(\Psi_*)$ from Eqn. 2.13. The above scheme has been validated for subsonic and transonic flows. It has been compared to steady and unsteady experimental data as well as other CFD codes (see Appendix D.).

2.2 POD Implementation with Potential Equation

POD can be implemented in a fully implicit manner in the above scheme. Following the work of Hall, et al. (34), the reduced order variable in Eqn. 2.1 becomes $\hat{\epsilon}$, for the ξ sweep,

$$\overline{\Delta\Psi} = \Phi \bar{\hat{\epsilon}}. \quad (2.19)$$

Substitution into Eqn. 2.17 yields,

$$L_\xi \Phi \bar{\hat{\epsilon}} = R. \quad (2.20)$$

Applying the transpose of Φ to both sides the above equation,

$$\Phi^T L_\xi \Phi \bar{\epsilon} = \Phi^T R \quad (2.21)$$

produces $\Phi^T L_\xi \Phi$, a square $(M \times M)$ matrix, where M is the number of modes in the POD/ROM. Because $M \ll N$, the matrix $\Phi^T L_\xi \Phi$ can be easily inverted to solve the ξ sweep,

$$\bar{\epsilon} = (\Phi^T L_\xi \Phi)^{-1} \Phi^T R, \quad (2.22)$$

$$\overline{\Delta\Psi} = \Phi (\Phi^T L_\xi \Phi)^{-1} \Phi^T R. \quad (2.23)$$

Tridiagonal techniques require a reordering from row major to column major between the ξ and η sweeps. Likewise, $\overline{\Delta\Psi}$ must be reordered before the next POD step. After reordering, the same POD steps are applied for the η sweep;

$$L_\eta \Delta\Psi = \overline{\Delta\Psi}, \quad (2.24)$$

$$L_\eta \Phi \hat{\epsilon} = \overline{\Delta\Psi}, \quad (2.25)$$

$$\Phi L_\eta \Phi \hat{\epsilon} = \Phi^T \overline{\Delta\Psi}, \quad (2.26)$$

$$\hat{\epsilon} = (\Phi^T L_\eta \Phi)^{-1} \Phi^T \overline{\Delta\Psi}, \quad (2.27)$$

This can then be converted back to the full-order solution used in the Newton's method,

$$\Delta\Psi = \Phi (\Phi^T L_\eta \Phi)^{-1} \Phi^T \overline{\Delta\Psi}. \quad (2.28)$$

Computational savings come from the inversion of $(\Phi^T L_\xi \Phi)$ and $(\Phi^T L_\eta \Phi)$ being less computationally expensive than their corresponding tridiagonal solutions of Eqns. 2.17 and 2.18. The inversion of $(\Phi^T L_\xi \Phi)$ and $(\Phi^T L_\eta \Phi)$ could be done with a weighted pseudo-inverse for more accuracy. Weighting assigns more importance to modes that dominate the fluid dynamics. A weighted POD/ROM technique was presented by Willcox and Perairet in 2001 (37), that demonstrated balanced modes for a small deformation pitching and plunging airfoil, showing good results. However, weighting techniques assume a

level of knowledge about the nature of the model problem and the way the modes affect the fluid dynamics. A user must know which modes to weight heavily. In addition, the weighting would require an additional post processing matrix multiplication, decreasing the efficiency. In the truncation method described, the weighting is binary, and based on the contribution of the eigenmodes.

POD is an excellent technique for developing an optimal reduced-order model, from observed data. In practice, most of the computations for POD are done during the training process and do not impact the execution of the POD/ROM itself. This makes POD/ROM a computationally attractive technique as well. POD/ROM can be conveniently incorporated to the full-potential equation. The application of POD/ROM with the full-potential equation is explored in later chapters through model problems.

III. Deforming Grid Error Estimation

In most aeroelastic problems, the motion of the body is tightly coupled to the resulting fluid dynamics. As a result, it is difficult to separate the effects of grid motion from the coupled POD/ROM. A rigid grid, attached to the body in motion and moving with it, eliminates deformation. The resulting POD/ROM/RG can then be compared to a POD/ROM/DG to determine the exact effects of deformation. However, rigid grid motion is not possible in all problems, such as in the case of a moving flap attached to an airfoil. If an analytical solution is applied to a deforming grid, then the fluid dynamics can be decoupled from the grid motion and a POD/ROM created from only the grid deformation. However, analytical solutions are not available for many problems. To evaluate the effects of grid deformation on POD/ROM, some method of evaluating the quantitative effect of deforming grids on POD/ROM accuracy needs to be developed. Two issues dominate: the degradation of accuracy due to the deforming grid, and the robustness of POD/ROM/DGs.

3.1 *Qualitative Error Estimate*

To estimate degradation of accuracy, one technique of estimating the error for a deforming grid POD/ROM is to limit the amount of deformation for a simplified problem. For instance, in an oscillating panel if the deflection is small enough, the number of deforming grid points can be varied from a limited number near the panel, to more points further out (Fig. 3.1). This allows POD/ROM to be created with nearly identical fluid dynamics but differing deforming regions. The resulting solutions can be compared to their respective full-order solutions. The percentage of deformation and the resulting error for a fixed number of modes can give an estimate of the error resulting solely from grid deformation.

3.2 *Deforming Grid Metric*

To examine the robustness of the POD/ROM on differing grids, a separate technique is needed. In examining the POD process, it is noted that the snapshots taken of the fluid dynamics during the training process represent the range of the modes created. That is,

only fluid structures captured in the training process, or their linear combinations, can be recreated by POD/ROM. Also, the snapshots of the fluid dynamics are arranged in index-space and therefore relationships between the respective snapshot of the grids are lost. Each grid is assumed to be identical to the previous. This is not the case with a deforming grid. Therefore, it is necessary to track the relative deformation of the grids during the training process. The training grids represent the range of grid motion. The grids captured during the training process, or their linear combinations, should have POD/ROM/DG with smaller grid deformation error. If the POD/ROM/DG is run on grids which differ significantly from the training grids, then the grid deformation error increases.

To evaluate how closely the run grids match the training grids, a grid modal matrix can be created from the grid snapshots. Snapshot matrices of the x and y locations for the deforming grid are stored during the training process. The snapshots are based on the perturbation from a default grid to highlight the relative deformation. The grid snapshot matrices are used to create a grid modal matrix, Φ_G , in a fashion similar to the creation of the modal matrix of the POD/ROM/DG. The grid modal matrix represents the range of grid deflections during training. The grid modal matrix is correlated to the POD/ROM/DG, in that the grid snapshots are taken at the same points in time as the fluid snapshots.

An error term can be generated from the grid modal matrix through a pseudo-inverse technique. Assuming that the grid can be represented by a linear combination of the training grids,

$$x \approx \Phi_G \hat{x}, \quad (3.1)$$

where x is the exact value of the run grid. To compute \hat{x} directly, a pseudo-inverse of Φ_G is needed. Using a Generalized Inverse (38), and multiplying both sides of Eqn. 3.1 by the transformed matrix, Φ_G^T produces a square matrix, $\Phi_G^T \Phi_G$ on the RHS,

$$\Phi_G^T x = \Phi_G^T \Phi_G \hat{x}, \quad (3.2)$$

that can be inverted.

$$\hat{x} = (\Phi_G^T \Phi_G)^{-1} \Phi_G^T x. \quad (3.3)$$

Finally, the error of the difference between the training grids and the run grid is determined by substituting \hat{x} into the original approximation for x and subtracting it from the exact run grid x value,

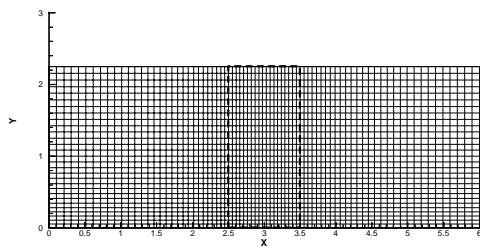
$$error_x = x - \Phi_G (\Phi_G^T \Phi_G)^{-1} \Phi_G^T x \quad (3.4)$$

The term $\Phi_G (\Phi_G^T \Phi_G)^{-1} \Phi_G^T$ represents how closely the run grid is represented by the training grid. The same technique can be used for the other spatial dimensions.

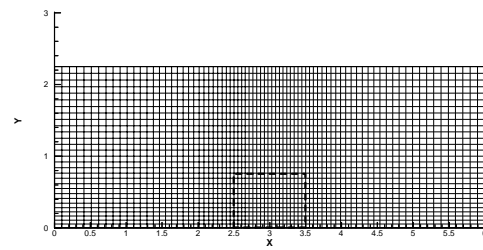
Both the grid modal matrix and the pseudo-inverse need only be generated once; therefore the error evaluation does not add significantly to the overall computation time. Several metrics are considered for correlation to the POD/ROM/DG error: maximum percentage grid error, L_2 norm of the error, and the grid error scaled to the non-dimensional length unit of the problem.

The grid error can be correlated to the error of the POD/ROM by means of running a test case. A POD/ROM is created at one set of grid deformations and then run at a second set of grid deformations. The error of the POD/ROM to the full solution for the second set of grid deformations is due to the misalignment of the modes to the grid point locations. By comparing the relative grid error and the POD/ROM error, the correlation between the errors can be determined. An acceptable level of POD/ROM error is then selected and the corresponding threshold of grid error established. Once the grid error is correlated to the POD/ROM error, the grid error is used as a threshold indicator for the accuracy of the POD/ROM. When the grid error exceeds a certain threshold, the accuracy of the POD/ROM has also exceeded the preset threshold indicating to the user that the POD/ROM should be replaced.

These techniques are the basis for comparing deforming and static grid POD/ROMs. The deforming grid metric is used in the subsequent applications to evaluate robustness of deforming grid POD/ROMs and to determine the best available POD/ROM for any particular grid deformation.



(a) 100 percent Doman



(b) 33 percent Domain

Figure 3.1 Deforming Grid Domains

IV. Oscillating Panel

To evaluate the issues of POD/ROM with a deforming grid, the nonlinear, discrete, full-potential equation in the simulation of unsteady flow over an oscillating panel was analyzed. This application coupled the fluid dynamics and the grid deformation. It required a reduced order model to determine the effects of grid deformation, unlike the translating cylinder model problem (see Appendix A.) that evaluated only the accuracy of the analytical solution projected into a subspace. The panel oscillation was forced and the fluid dynamics were not allowed to alter the grid motion. As a result, the predefined motion of the grid drove the fluid dynamics. The coupled nature of the fluid and grid dynamics made it impossible to evaluate modes solely caused by the grid motion. Therefore, the oscillating panel was modeled both with a deforming grid and a static grid transpiration boundary condition (TBC). This allowed a direct comparison of a POD/ROM on a static grids and deforming grids for a nearly identical problem, showing the effects of grid deformation on POD/ROMs. To evaluate accuracy of the POD/ROM/DG, the number of grid points that were allowed to deform was varied. Some types of problems preclude the use of the transpiration boundary condition or a rigidly moving grid. Therefore, varying the number of deforming grid points was used to provide a qualitative method of evaluating the accuracy of POD/ROM/DG. To evaluate the robustness of POD/ROM on deforming grids, POD/ROM/DGs were used on grids other than their training grids. The training grids were compared to the grids at which POD/ROM/DGs were run. The relative grid error allowed a measure of merit of the training process to be developed and correlated to errors of POD/ROM/DGs.

4.1 Application

Following the work of Pettit and Beran (39), the application of inviscid 2-D flow over an oscillating panel was used to examine POD with deforming grids. The flow-field was assumed to occur in an open channel above an infinite, segmented panel that nominally is in the $y = 0$ coordinate plane, except for a segment between $x = 2.5$ and $x = 3.5$ for which the panel shape was a smoothed parabolic defined by $y(x, t)$. The chord length (measured from start to the end of the panel), c , of the panel was normalized to a value of 1.0. The

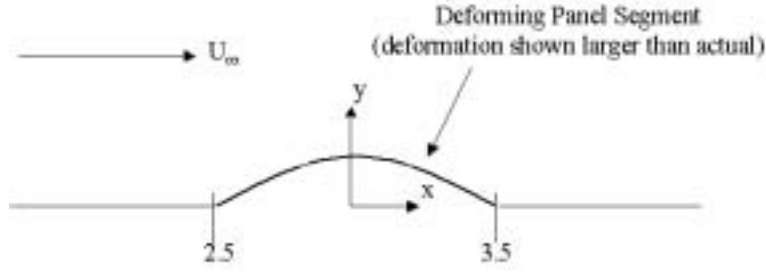


Figure 4.1 Model Problem

channel was 2.25 chord lengths high and the inlet and outlet were 3.0 chord lengths from the center point of the panel. The domain dimensions were sufficient to provide a good solution for the freestream Mach number of 0.5. The Mach number was selected to keep the flow over the deflected panel subsonic to prevent shockwaves. A 80×30 grid was used for the model problem, with 20 grid points evenly spaced on the panel surface (Fig. 4.1). The surface was based on a smoothly varying function used for 2-D experimental wind tunnel tests (40):

$$X(t) = \cos(\theta) - \frac{r(t)}{4} [\cos(\theta) - \cos(3\theta)], \quad (4.1)$$

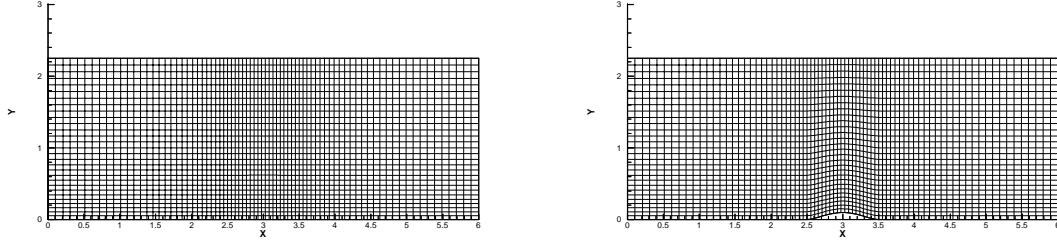
$$Y(t) = \sin(\theta) - \frac{r(t)}{4} [3\sin(\theta) - \sin(3\theta)], \quad (4.2)$$

where θ ranges from $0 \leq \theta \leq \pi$ and $r(t)$ was the time dependant amplitude of the panel at the midpoint, scaled to the chord length. The amplitude was varied based on a cosine function to give a zero panel velocity at the peak and zero deflections,

$$r(t) = A \left[-0.5 \left(\cos \left(2\pi f \frac{t}{t_{\max}} \right) - 2 \right) \right]. \quad (4.3)$$

A was the maximum amplitude of the midpoint on the panel, f was the non-dimensional frequency of oscillation, t was the time, and t_{\max} the maximum time for the test.

The density and velocity were non-dimensionalized using the far-field density, ρ_∞ , and velocity, U_∞ . Pressure was non-dimensionalized using the far-field dynamic pressure, P_∞ (subsequent references to variables assume non-dimensional forms).



(a) Transpiration Boundary Condition Static Grid

(b) Deforming Grid

Figure 4.2 Computational Grids

In the transpiration boundary condition case, the grid was static and undeflected. In the deforming grid case, the grid was smoothly deformed above the panel (Fig. 4.2). The panel was not allowed to dip into negative deflections. At the zero deflection point, the transpiration and the deforming grid cases had identical grids.

4.1.1 Boundary Conditions. Two boundary conditions were used to model the deflecting panel; the transpiration boundary condition and a deforming grid. The transpiration boundary condition is a small disturbance theory model that uses injected fluid (imparted velocity) through an undeflected transpiring panel to simulate a deflection. This allows the transpiration boundary condition grid to remain static. The transpiration boundary condition enforces the exact condition of impermeability of a deflected panel surface by the injection of velocity at the undeflected surface,

$$-u \frac{\partial y_s}{\partial x} + v = \frac{\partial y_s}{\partial t}. \quad (4.4)$$

$\frac{\partial y_s}{\partial x}$ is the slope of the deflected panel and $\frac{\partial y_s}{\partial t}$ the time rate of change of the panel (41). This transfer of boundary conditions is identical to that employed in small-disturbance theory, where one assumes the regularity of the computed solution and small deformation. For the full-potential equation the boundary condition becomes,

$$V = (u - x_\tau) (\Delta y)_\xi J, \quad (4.5)$$

where Δy is difference in the y ordinates of the assumed deflected panel and the actual undeflected surface. The transpiration boundary condition assumes a quasi-static change in the grid, and therefore is limited to low oscillation frequencies for the model problem.

The deforming grid boundary condition physically alters the grid between each iteration to match the new deflection of the panel. This requires that time dependant grid metrics be properly calculated and included in the governing equations. The deforming grid boundary condition enforces the exact condition of impermeability at the deflected panel surface, $V = 0$ (see Appendix C for full development).

4.1.2 Full-Order Results. Full-order results are created during the training process to compare with the POD/ROM results. The model problem is non-linear in both maximum amplitude and oscillation frequency. Fig. 4.3 shows the periodic minimum normal force coefficient, C_N , after the flow is fully developed (approximately ten oscillations) for a variety of oscillation frequencies and amplitudes. Three maximum amplitudes ($A = 0.05, 0.1, 0.15$) and nine oscillation frequencies are used (0.1 to 1.0), for 36 different combinations. The normal force coefficient is defined as,

$$C_N = \frac{\sum \frac{(P_\infty - P)}{Area}}{q_\infty}. \quad (4.6)$$

As the amplitude is increased, the problem moves from subsonic to transonic flow (at about $A = 0.17$). This study is interested in subsonic flow fields and so the amplitude is limited to 0.15. The increasing slope of C_N verses frequency shows increasing non-linear behavior with maximum amplitude. Breakpoints in the slope at frequencies of 0.4 and 0.65 show changes in linear behavior with frequency. To be accurate, a POD/ROM must be able to capture these non-linear behaviors.

In addition matching derived variables, POD/ROMs must be able to simulate the full-order solution in the flow field. Sequences of full-order results are created for pressure contours to evaluated how the frequency affects pressure. Figs. 4.4 and 4.5 show the non-linear effect of frequency for three cases (0.1 in first column, 0.5 in second column, and 1.0 in third column). The figures in each row show identical panel deflection amplitudes

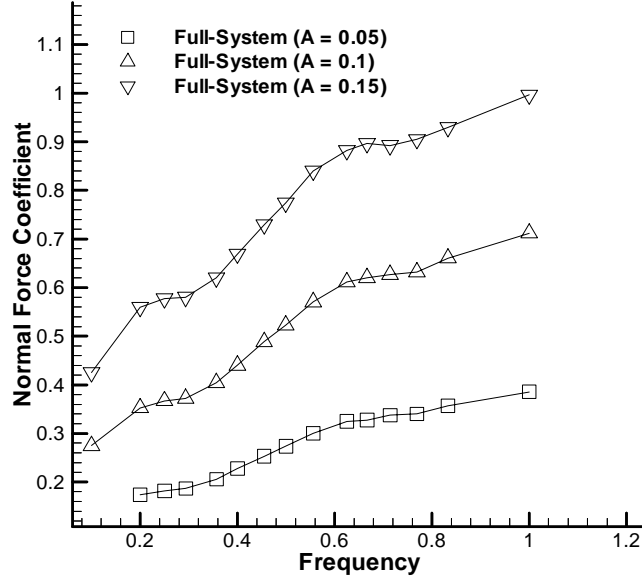
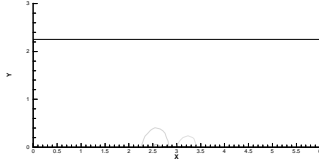


Figure 4.3 Minimum C_N (full-system)

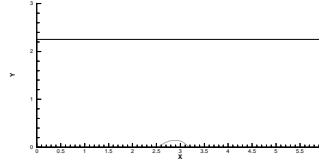
for difference frequencies, and each row is a different increment in time. As the panel is deflected in time the fluid is displaced in a wave that propagates away from the panel. At low oscillation frequencies (below 0.4), the problem is quasi-steady and the flow over the panel dominates the fluid structure. The pressure contours are nearly symmetric and there is little interaction upstream of the panel. As the oscillation frequency is increased, the velocity of the panel approaches that of the freestream fluid and pressure waves are created that interact upstream with the flow field to create non-linearities. The pressure waves are dissipated upstream by the inlet conditions and are passed downstream and out of the flow field. As the frequency increases further, the panel oscillates quickly enough to produce a second pressure wave before the first pressure wave can pass beyond the panel. This results in an amplification of the pressure waves as they combine upstream.

4.2 POD/ROM Results

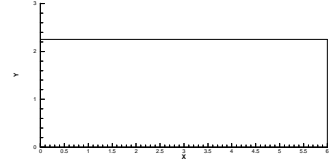
Several experiments were completed using the oscillating panel model problem. First, comparisons were made between the accomplished accuracy of static grids as compared to



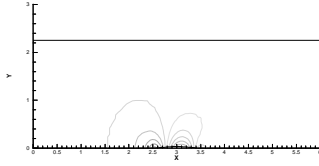
(a) $f = 0.1, A = 0.1, t = 1$



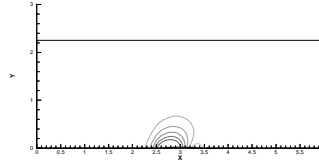
(b) $f = 0.5, A = 0.1, t = 0.2$



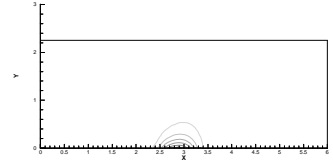
(c) $f = 1, A = 0.1, t = 0.1$



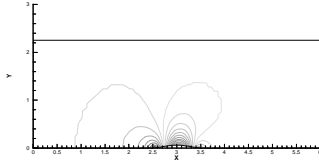
(d) $f = 0.1, A = 0.1, t = 2$



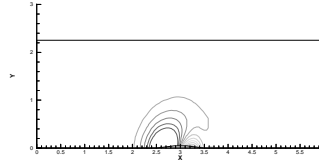
(e) $f = 0.5, A = 0.1, t = 0.4$



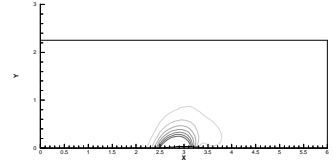
(f) $f = 1, A = 0.1, t = 0.2$



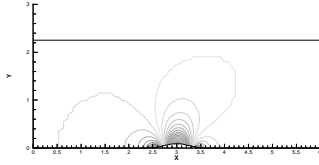
(g) $f = 0.1, A = 0.1, t = 3$



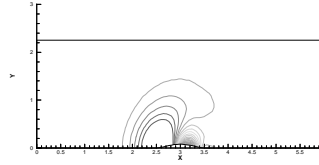
(h) $f = 0.5, A = 0.1, t = 0.6$



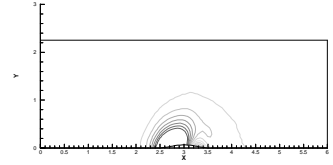
(i) $f = 1, A = 0.1, t = 0.3$



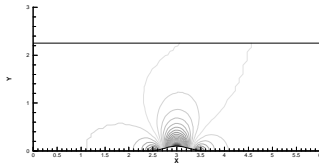
(j) $f = 0.1, A = 0.1, t = 4$



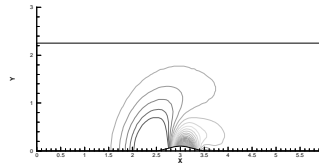
(k) $f = 0.5, A = 0.1, t = 0.8$



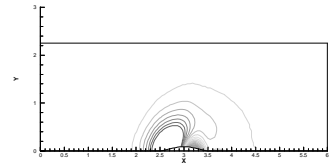
(l) $f = 1, A = 0.1, t = 0.4$



(m) $f = 0.1, A = 0.1, t = 5$

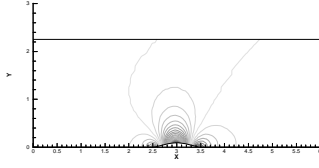


(n) $f = 0.5, A = 0.1, t = 1.0$

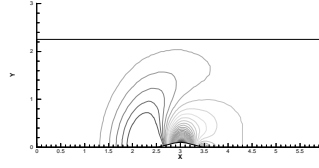


(o) $f = 1, A = 0.1, t = 0.5$

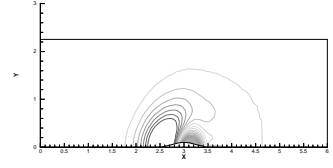
Figure 4.4 Pressure Contours for Full-system (part 1, single oscillation)



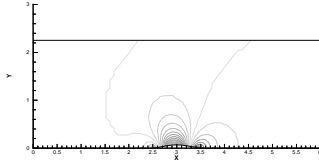
(a) $f = 0.1, A = 0.1, t = 6$



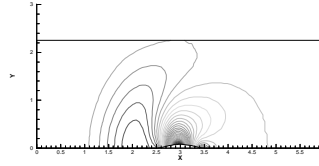
(b) $f = 0.5, A = 0.1, t = 1.2$



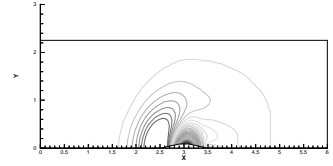
(c) $f = 1, A = 0.1, t = 0.6$



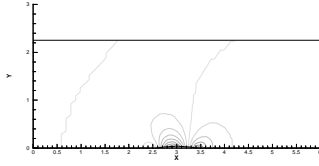
(d) $f = 0.1, A = 0.1, t = 7$



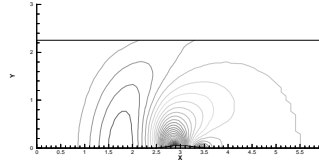
(e) $f = 0.5, A = 0.1, t = 1.4$



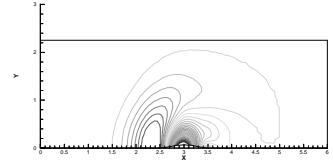
(f) $f = 1, A = 0.1, t = 0.7$



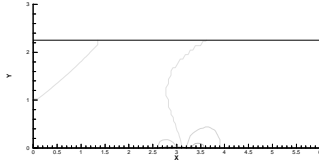
(g) $f = 0.1, A = 0.1, t = 8$



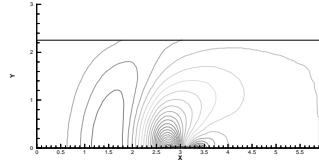
(h) $f = 0.5, A = 0.1, t = 1.6$



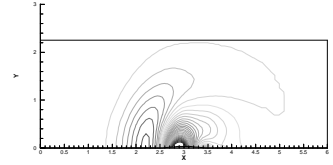
(i) $f = 1, A = 0.1, t = 0.8$



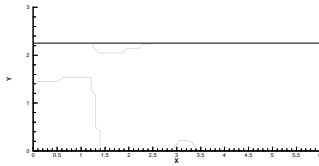
(j) $f = 0.1, A = 0.1, t = 9$



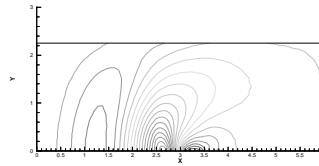
(k) $f = 0.5, A = 0.1, t = 1.8$



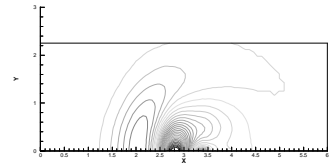
(l) $f = 1, A = 0.1, t = 0.9$



(m) $f = 0.1, A = 0.1, t = 10$



(n) $f = 0.5, A = 0.1, t = 2.0$



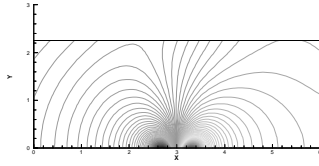
(o) $f = 1, A = 0.1, t = 1.0$

Figure 4.5 Pressure Contours for Full-system (part 2, single oscillation)

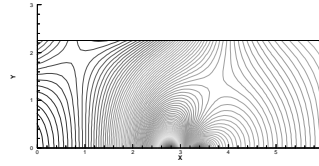
that of deforming grids. Next, POD/ROMs of various amplitudes and frequencies were created and tested to determine their accuracy. Then, these POD/ROMs were combined by merging their snapshot matrices to determine if a single model could be created. Finally, comparisons were made of the accuracy of deforming grid POD/ROMs when run at amplitudes differing from their training amplitudes.

4.2.1 Individual POD/ROM. To evaluate the accuracy of POD/ROMs with deforming grids, POD/ROMs were constructed for the static, POD/ROM/RG, and deforming grid, POD/ROM/DG, cases. A single POD/ROM/RG was taken at a maximum amplitudes (A) of 0.1 and an oscillation frequency, f , of 0.1. The low frequency resulted in a quasi-steady problem, necessary for the TBC to be accurate. Individual POD/ROM/DGs were constructed for deforming grids computed at maximum amplitudes ($A = 0.05, 0.1, 0.15$). At the various amplitudes, nine oscillation frequencies were used ranging from 0.1 to 1.0, creating 36 different POD/ROM/DGs. The POD/ROM/DG were trained for only one oscillation, regardless of frequency of oscillation. During the training period, 20 snapshots were taken. The POD/ROM/DGs were then compared to their respective full-order solutions for fully developed flow (that occurred after approximately ten oscillations).

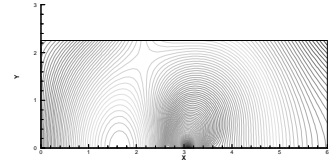
Static Grid: For the quasi-steady frequency of 0.1 and amplitude of 0.1, the POD/ROM/RG was able to reproduce an accurate solution. The primary mode of the static grid case was a scalar fraction of the flow at the largest deflection and accounted for 96% of the total modal contribution (Fig. 4.6). The modes of the POD/ROM/RG show structures similar to wave shapes that propagate upstream (Fig. 4.6 (h), (i), and (l)). The remaining modes decreased in energy rapidly and were negligible zero by the 9th mode (10^{-7}) (Fig. 4.7). The slope of the modal contribution was steep and indicated that relatively few modes were needed for an accurate solution. The POD/ROM/RG were able to reproduce the fluid flow at the fully developed condition (approximately 10 oscillations) very accurately with only 5 modes. This resulted in a reduction from 2400 to 5 dof. The flow field was reproduced with all fluid structures (Figs. 4.8 and 4.9). The results of the pressure contours for the POD/ROM/RG compared well to that of the full-order solution



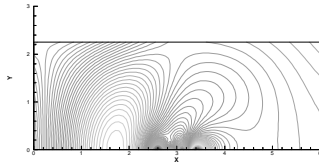
(a) Mode 1



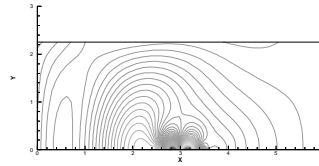
(b) Mode 2



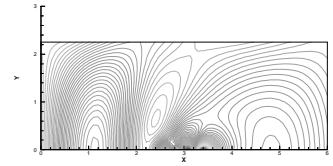
(c) Mode 3



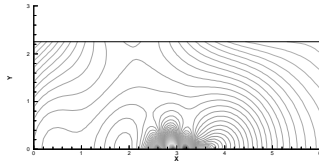
(d) Mode 4



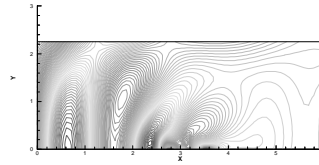
(e) Mode 5



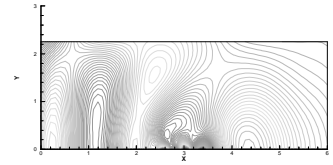
(f) Mode 6



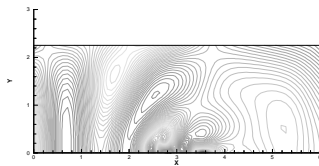
(g) Mode 7



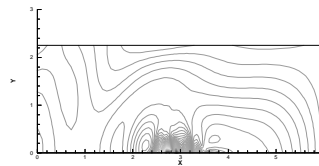
(h) Mode 8



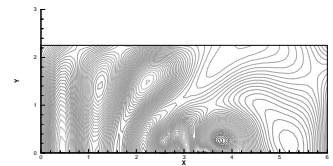
(i) Mode 9



(j) Mode 10



(k) Mode 11



(l) Mode 12

Figure 4.6 POD/ROM/RG Modes

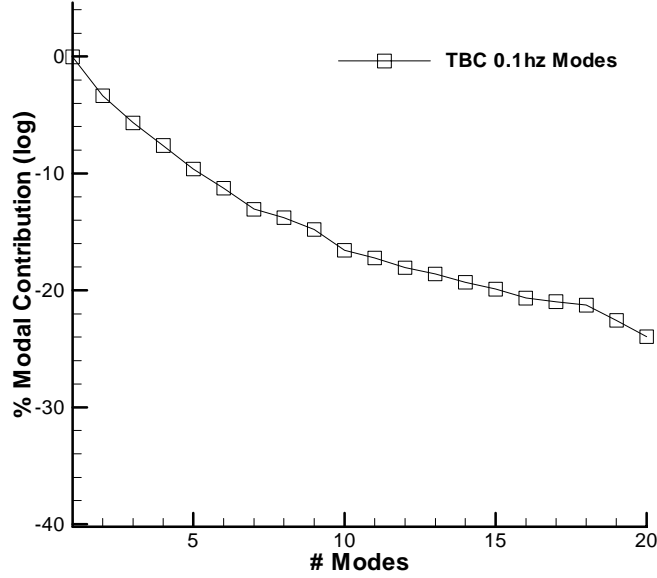
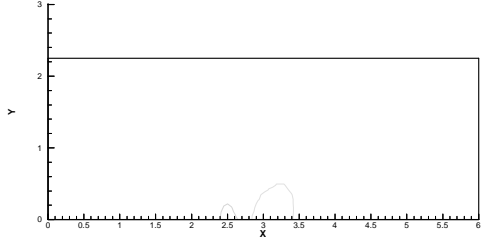


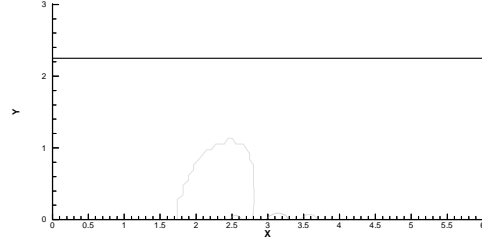
Figure 4.7 POD/ROM/RG Modal Contribution

(POD/ROM/RG in the first column and Full-order in second column) for the same frequency/amplitude combination. The contours of pressure were nearly identical, with only small variations in the far-field contours.

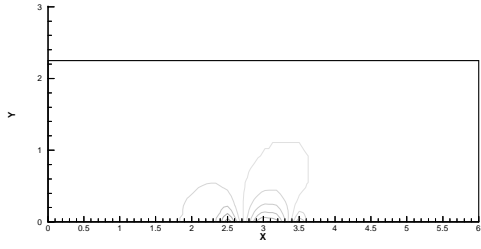
Deforming Grid: The individual POD/ROM/DGs were able to reproduce the deforming grid flow field for the different amplitude/frequency combinations using just 15 modes to an accuracy of 3%, based on density. This equated to an order reduction from 2400 to 15 dof. As the problem became more non-linear in either amplitude or frequency, more modes were necessary for an accurate solution, as shown by the reduction in accuracy for the higher frequency and higher amplitude cases at 15 modes (Fig. 4.10). The accuracy of the more non-linear regions could be improved by using additional modes. The flow field was reproduced with all fluid structures very accurately. The results of the pressure contours for the POD/ROM/DG compared to that of the full-order solution for various frequencies showed good accuracy with only slight deviations in the higher frequency POD/ROM/DG. (Figs. 4.11 to 4.16 for results of $A = 0.1$ and $f = 0.1, 0.5, 1.0$). POD/ROM/RG is shown in the first column and the full-order solution is shown in the



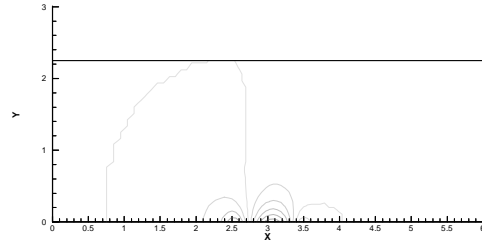
(a) POD/ROM, $t = 1$



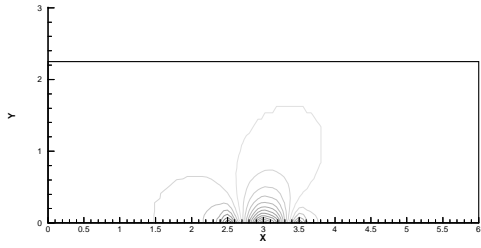
(b) Full System, $t = 1$



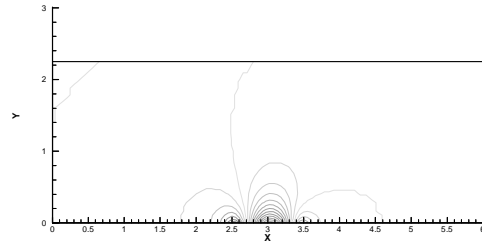
(c) POD/ROM, $t = 2$



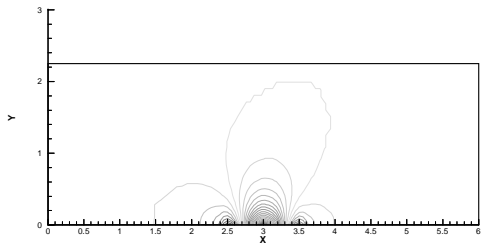
(d) Full System, $t = 2$



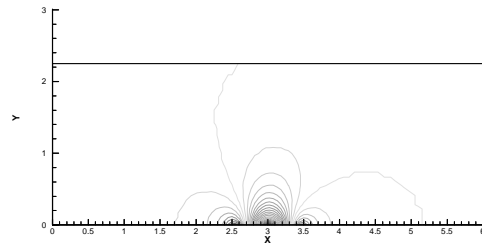
(e) POD/ROM, $t = 3$



(f) Full System, $t = 3$

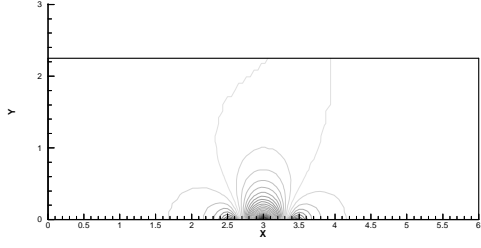


(g) POD/ROM, $t = 4$

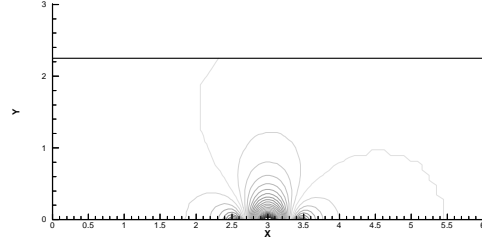


(h) Full System, $t = 4$

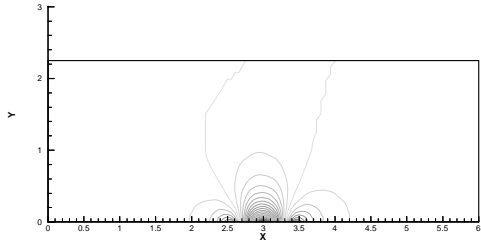
Figure 4.8 POD/ROM/RG vs. Full-Order Solution Pressure Contours (part 1) ($f = 0.1$, $A = 0.1$)



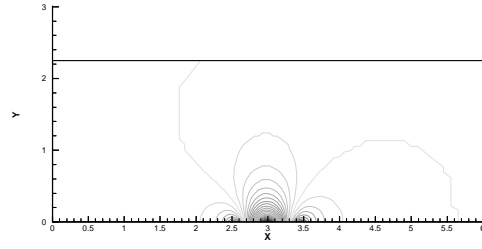
(a) POD/ROM, $t = 5$



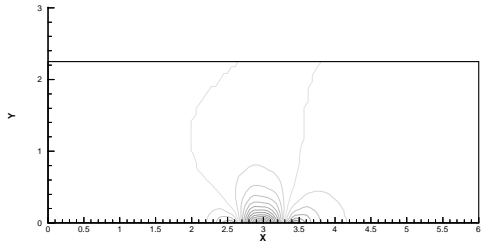
(b) Full System, $t = 5$



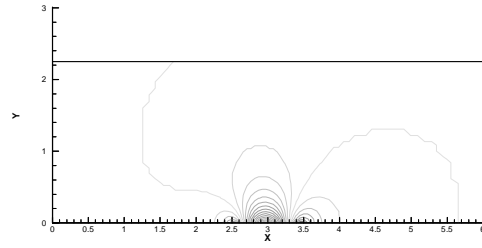
(c) POD/ROM, $t = 6$



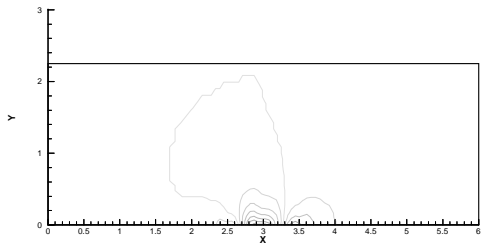
(d) Full System, $t = 6$



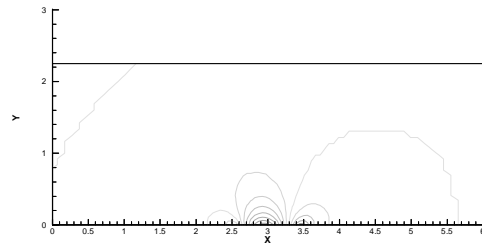
(e) POD/ROM, $t = 7$



(f) Full System, $t = 7$



(g) POD/ROM, $t = 8$



(h) Full System, $t = 8$

Figure 4.9 POD/ROM/RG vs. Full-Order Solution (part 2) ($f = 0.1$, $A = 0.1$)

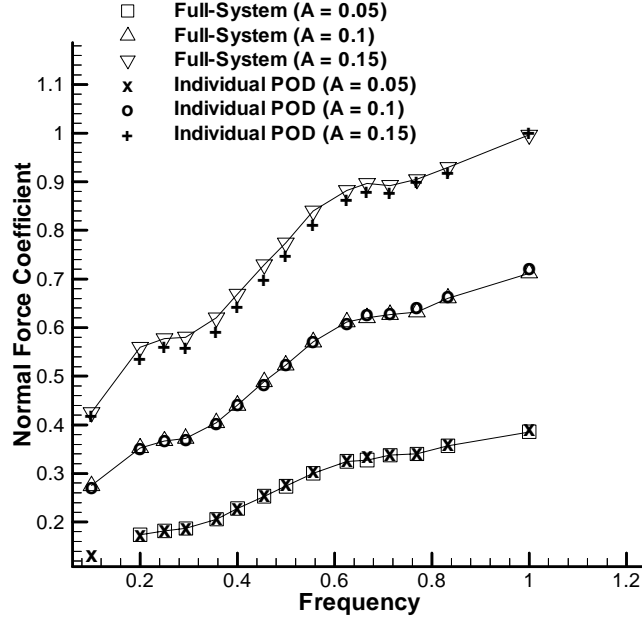
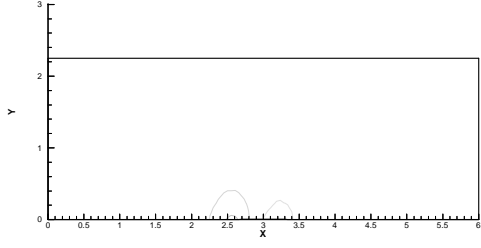


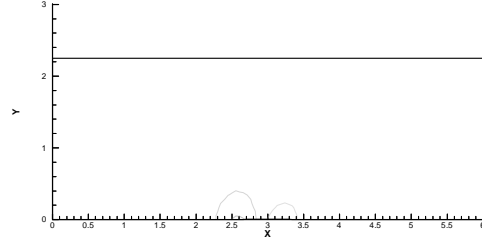
Figure 4.10 Minimum C_N (Individual POD/ROM/DG, 15 modes)

second column for the identical frequency/amplitude combinations. In examining the 0.1 amplitude cases, the modes of the POD/ROM/DG were significantly different from the POD/ROM/RG (Figs. 4.17 to 4.19 for results of $A = 0.1$ and $f = 0.1, 0.5, 1.0$). The $f = 0.1$ POD/ROM/DG primary mode was similar to that of the POD/ROM/RG, but the remaining modes differed in both near and far-field structures. The $f = 0.5$ and $f = 1.0$ POD/ROM/DGs had modes that were unique, with no corresponding similarities to the POD/ROM/RG modes. The modal contribution for the individual POD/ROM/DGs showed the increasing non-linearity caused by the increasing frequency (Fig. 4.20). In the more linear cases (lower frequency), the lower order modes decreased rapidly in energy. In the more non-linear cases (higher frequency), the lower order modes did not decrease in energy as quickly. The primary mode of the $f = 0.1$ POD/ROM/DG contained 81% of the total energy as compared to 70% for the $f = 0.5$ POD/ROM/DG and 69% for the $f = 1.0$ POD/ROM/DG.

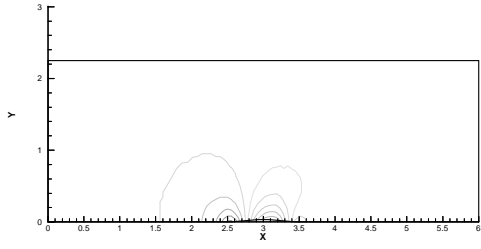
Static vs. Deforming Grid Comparison: The accuracy of both the static grid and deforming grid POD/ROMs was dependent on the number of modes retained, however,



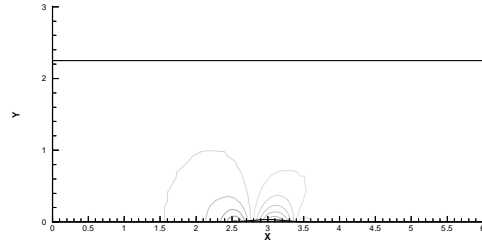
(a) POD/ROM, $t = 1$



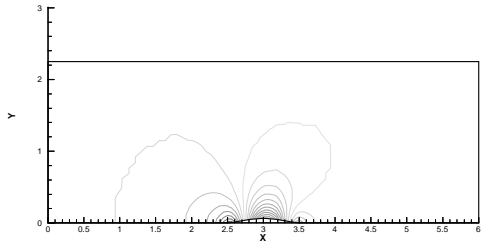
(b) Full System, $t = 1$



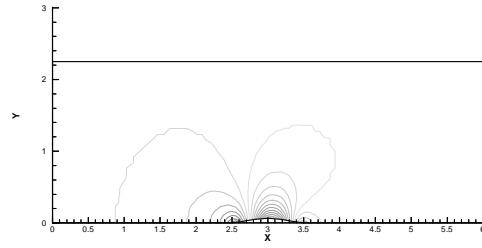
(c) POD/ROM, $t = 2$



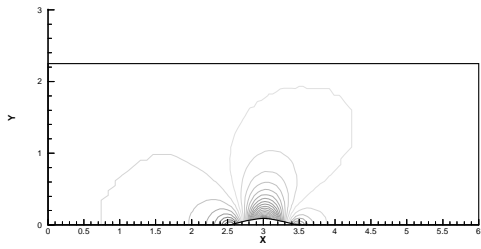
(d) Full System, $t = 2$



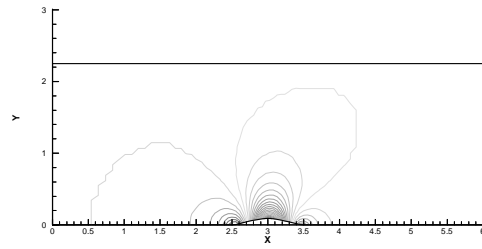
(e) POD/ROM, $t = 3$



(f) Full System, $t = 3$

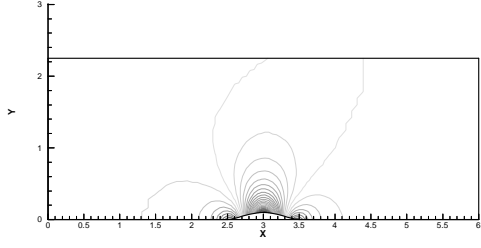


(g) POD/ROM, $t = 4$

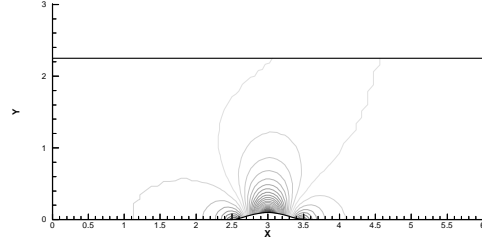


(h) Full System, $t = 4$

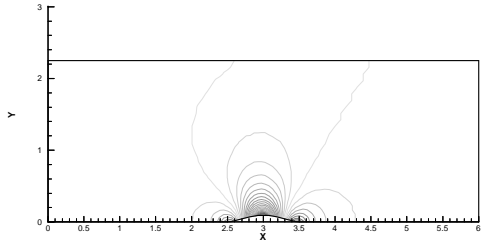
Figure 4.11 POD/ROM/DG vs. Full-Order Solution Pressure Contour (part 1) ($f = 0.1$, $A = 0.1$)



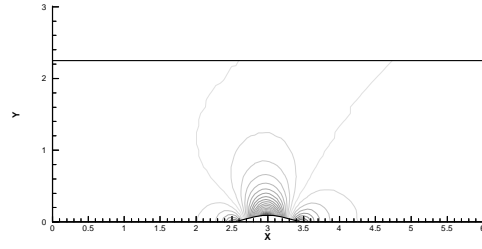
(a) POD/ROM, $t = 5$



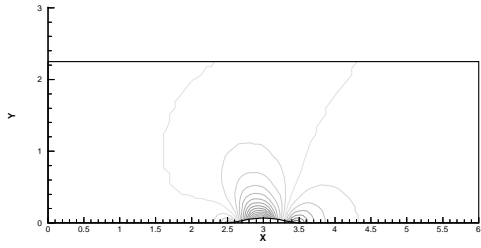
(b) Full System, $t = 5$



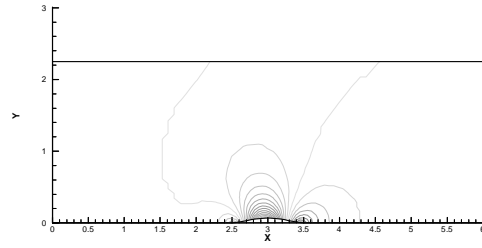
(c) POD/ROM, $t = 6$



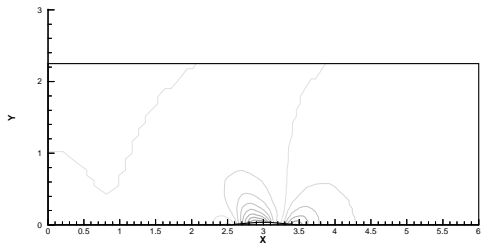
(d) Full System, $t = 6$



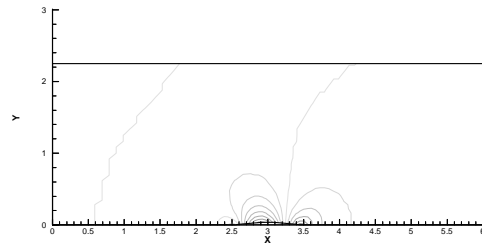
(e) POD/ROM, $t = 7$



(f) Full System, $t = 7$

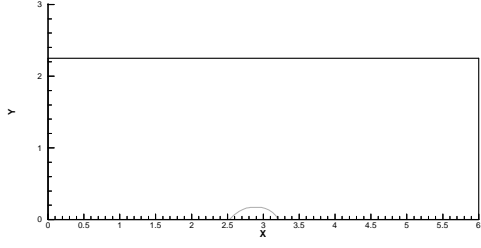


(g) POD/ROM, $t = 8$

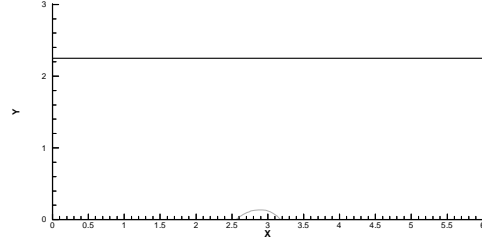


(h) Full System, $t = 8$

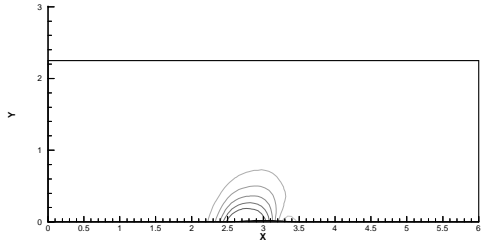
Figure 4.12 POD/ROM/DG vs. Full-Order Solution Pressure Contour (part 2) ($f = 0.1$, $A = 0.1$)



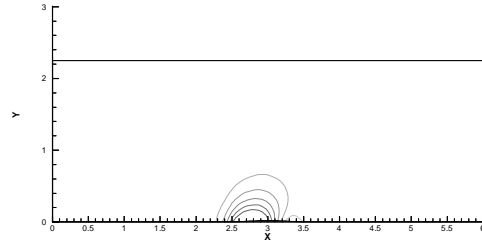
(a) POD/ROM, $t = 0.2$



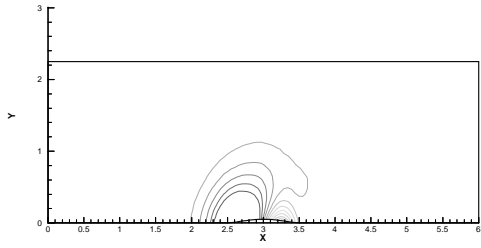
(b) Full System, $t = 0.2$



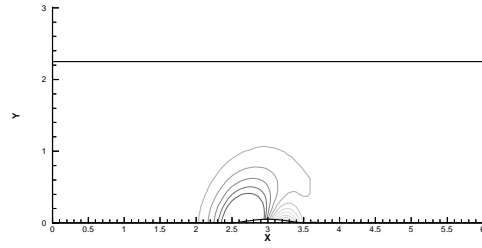
(c) POD/ROM, $t = 0.4$



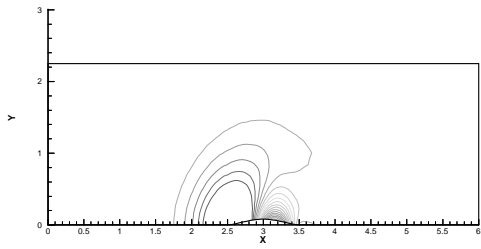
(d) Full System, $t = 0.4$



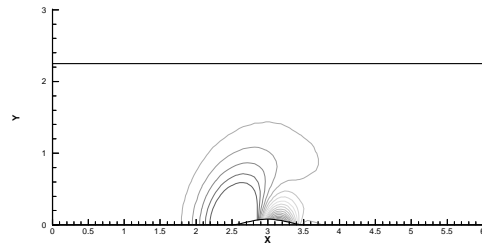
(e) POD/ROM, $t = 0.6$



(f) Full System, $t = 0.6$

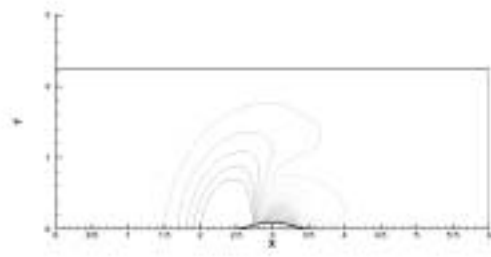


(g) POD/ROM, $t = 0.8$

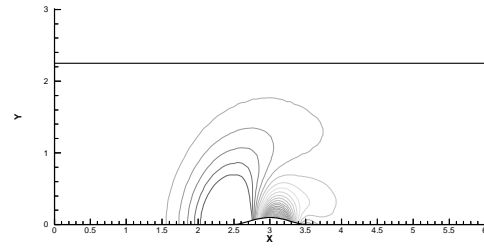


(h) Full System, $t = 0.8$

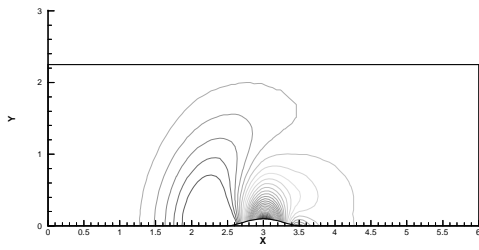
Figure 4.13 POD/ROM/DG vs. Full-Order Solution Pressure Contour (part 1) ($f = 0.5$, $A = 0.1$)



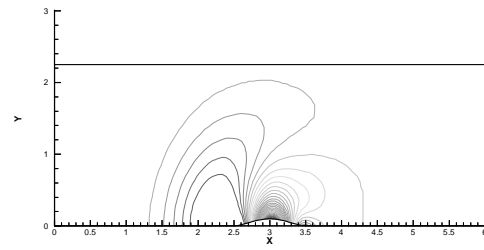
(a) POD/ROM, $t = 1.0$



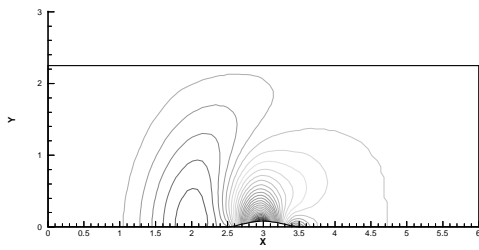
(b) Full System, $t = 1.0$



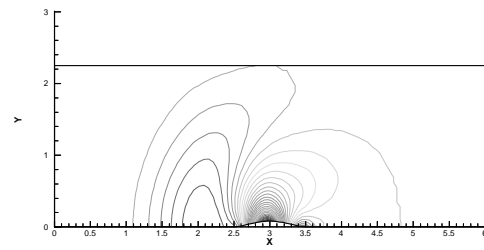
(c) POD/ROM, $t = 1.2$



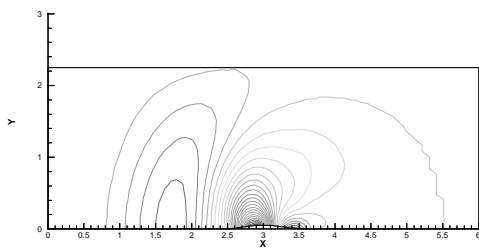
(d) Full System, $t = 1.2$



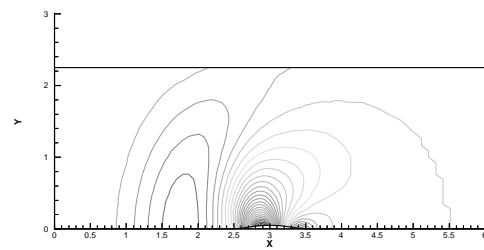
(e) POD/ROM, $t = 1.4$



(f) Full System, $t = 1.4$

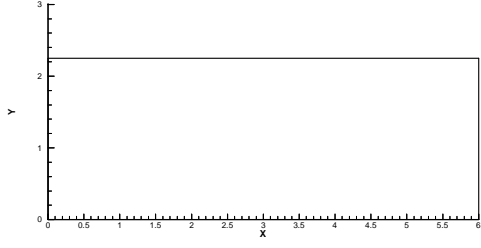


(g) POD/ROM, $t = 1.6$

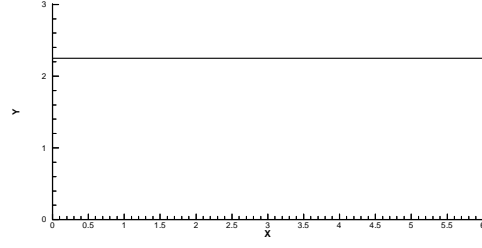


(h) Full System, $t = 1.6$

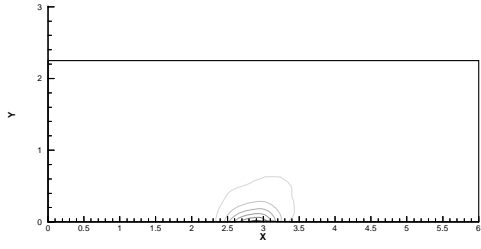
Figure 4.14 POD/ROM/DG vs. Full-Order Solution Pressure Contour (part 2) ($f = 0.5$, $A = 0.1$)



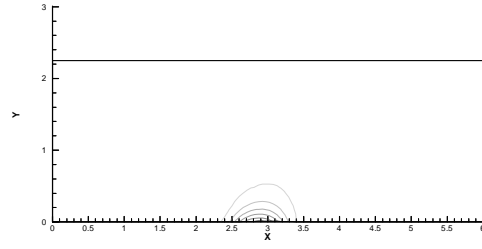
(a) POD/ROM, $t = 0.1$



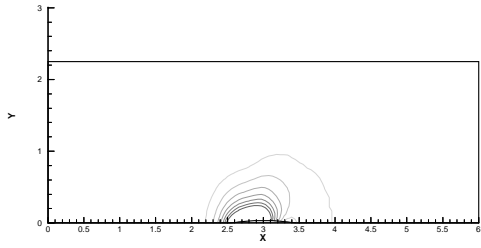
(b) Full System, $t = 0.1$



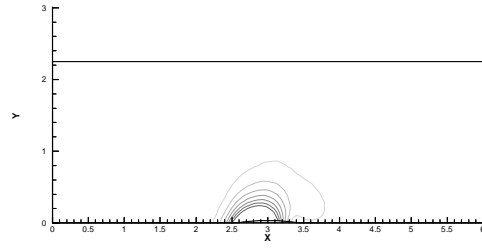
(c) POD/ROM, $t = 0.2$



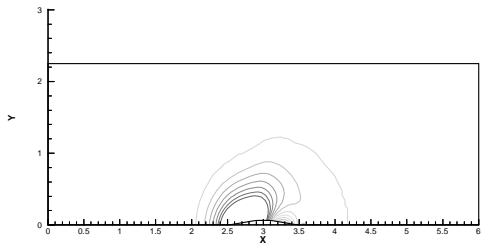
(d) Full System, $t = 0.2$



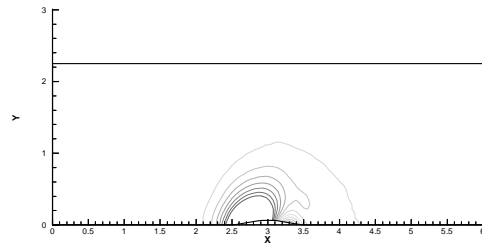
(e) POD/ROM, $t = 0.3$



(f) Full System, $t = 0.3$

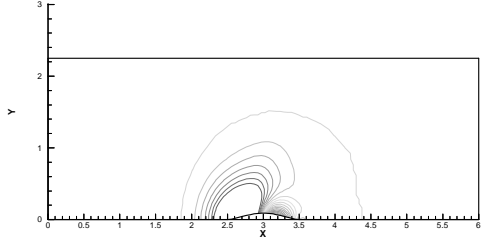


(g) POD/ROM, $t = 0.4$

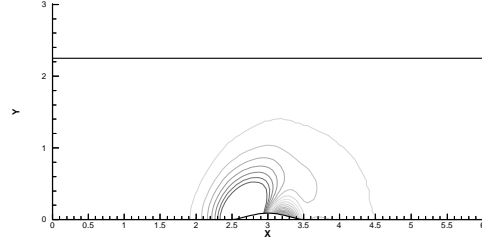


(h) Full System, $t = 0.4$

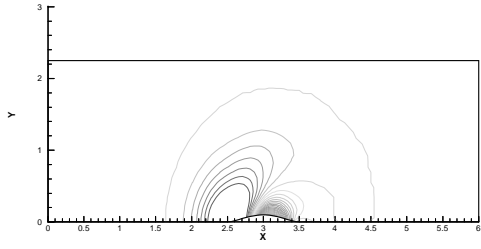
Figure 4.15 POD/ROM/DG vs. Full-Order Solution Pressure Contour (part 1) ($f = 1.0$, $A = 0.1$)



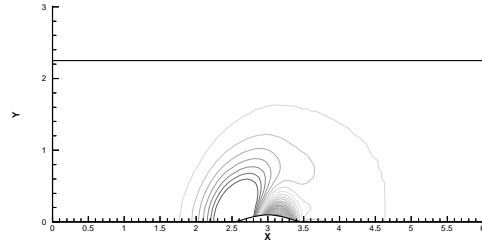
(a) POD/ROM, $t = 0.5$



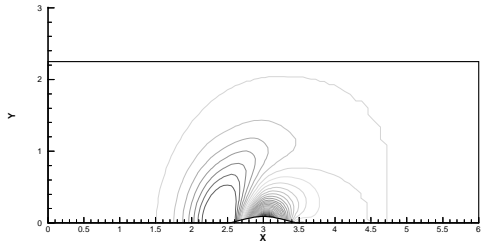
(b) Full System, $t = 0.5$



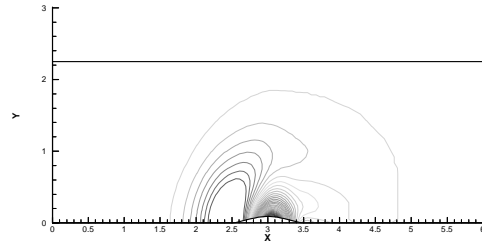
(c) POD/ROM, $t = 0.6$



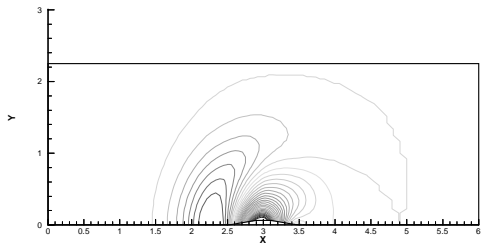
(d) Full System, $t = 0.6$



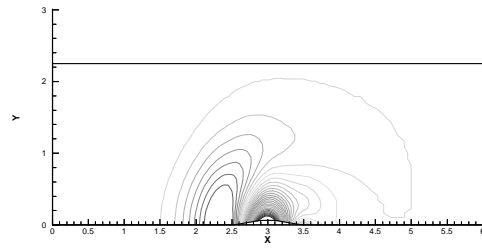
(e) POD/ROM, $t = 0.7$



(f) Full System, $t = 0.7$

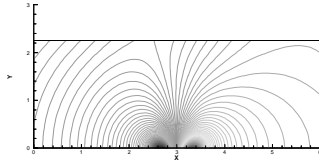


(g) POD/ROM, $t = 0.8$

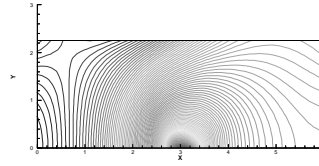


(h) Full System, $t = 0.8$

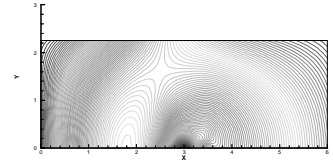
Figure 4.16 POD/ROM/DG vs. Full-Order Solution Pressure Contour (part 2) ($f = 1.0$, $A = 0.1$)



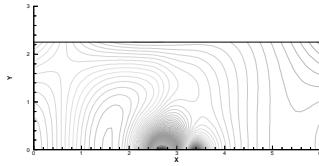
(a) Mode 1



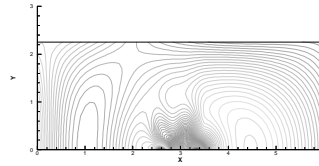
(b) Mode 2



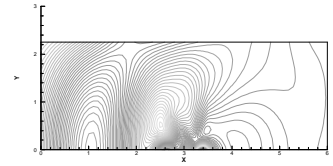
(c) Mode 3



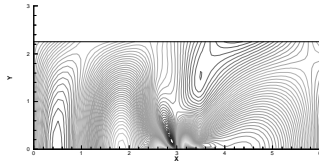
(d) Mode 4



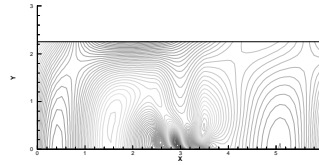
(e) Mode 5



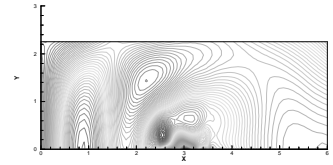
(f) Mode 6



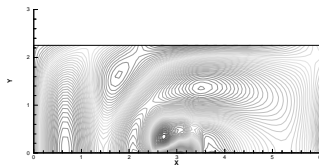
(g) Mode 7



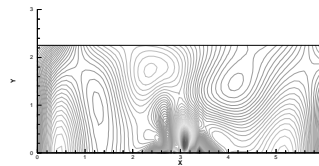
(h) Mode 8



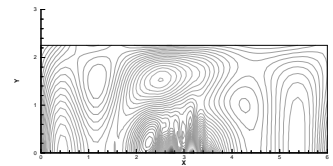
(i) Mode 9



(j) Mode 10

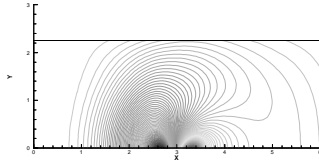


(k) Mode 11

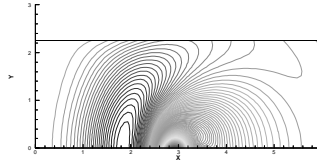


(l) Mode 12

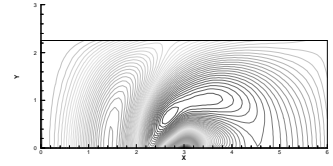
Figure 4.17 POD/ROM/DG Modes ($f = 0.1$, $A = 0.1$)



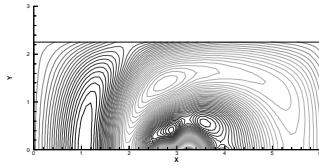
(a) Mode 1



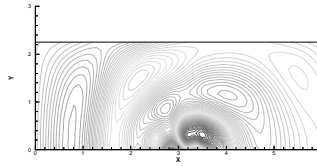
(b) Mode 2



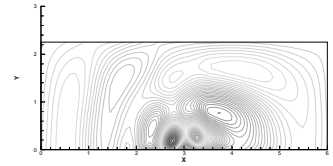
(c) Mode 3



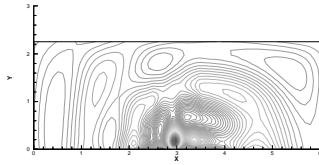
(d) Mode 4



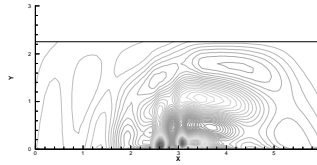
(e) Mode 5



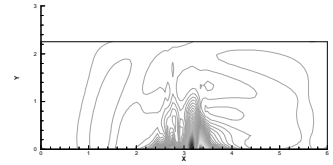
(f) Mode 6



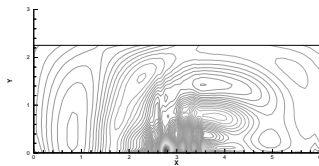
(g) Mode 7



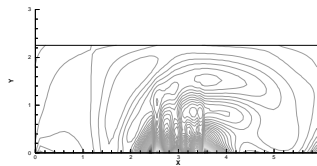
(h) Mode 8



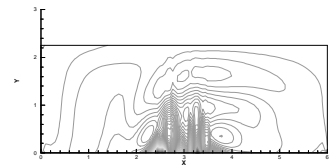
(i) Mode 9



(j) Mode 10



(k) Mode 11



(l) Mode 12

Figure 4.18 POD/ROM/DG Modes ($f = 0.5$, $A = 0.1$)

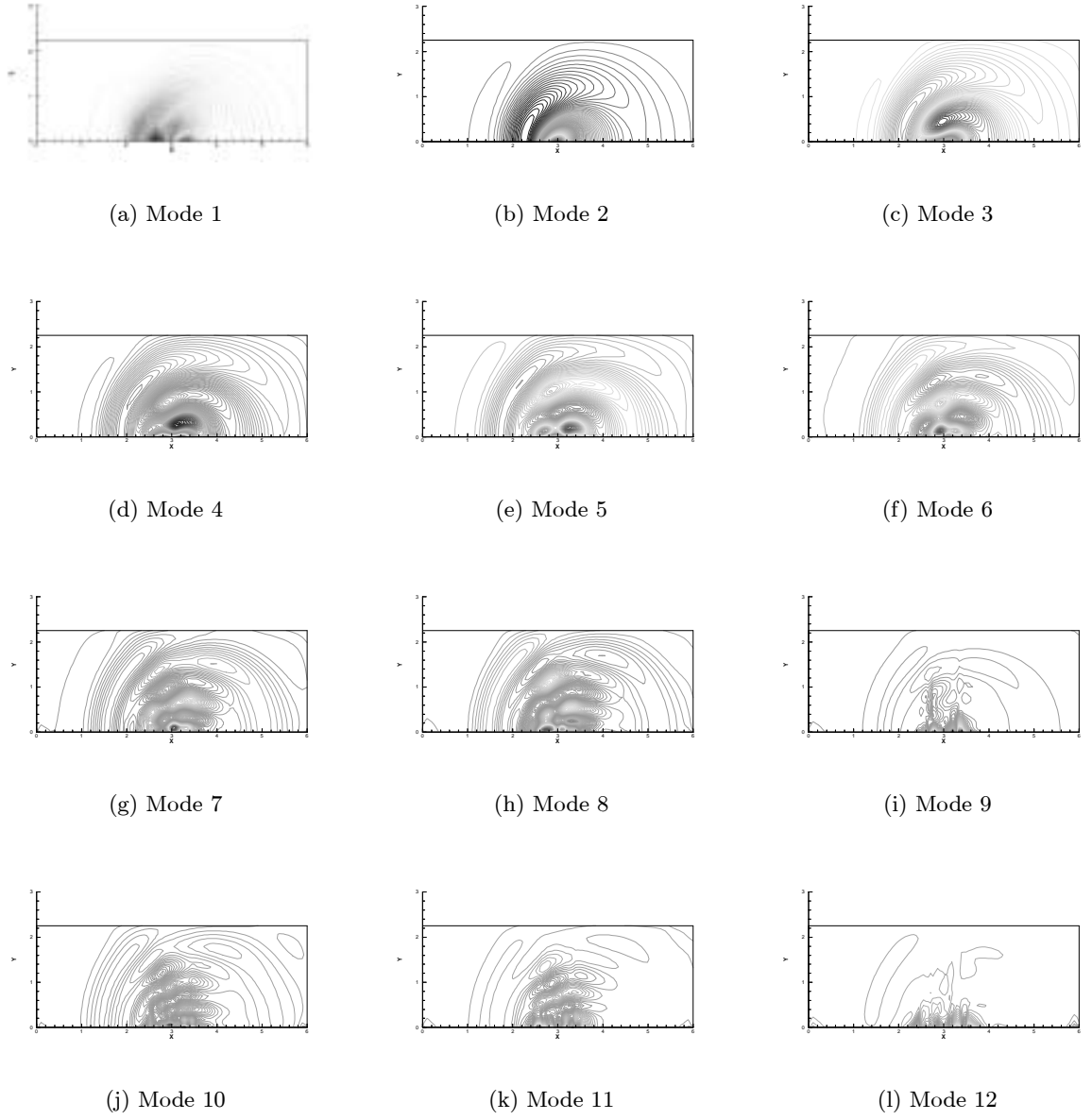


Figure 4.19 POD/ROM/DG Modes ($f = 1.0$, $A = 0.1$)

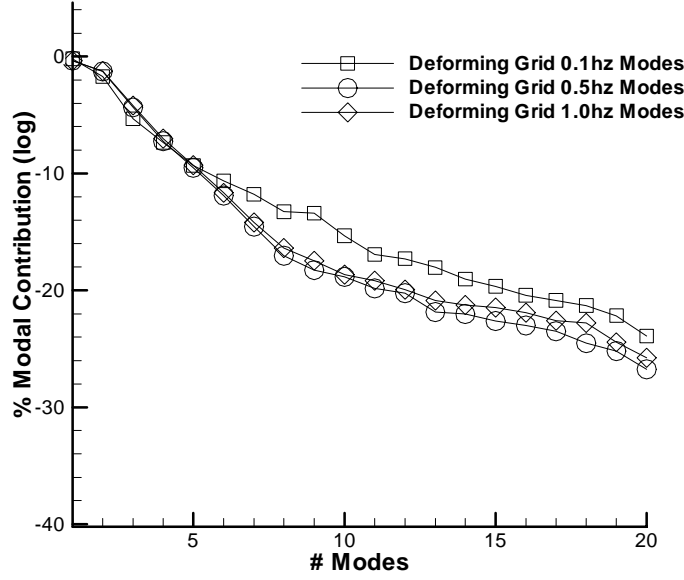


Figure 4.20 POD/ROM/DG Modal Contribution

the static grid was more accurate with fewer modes (Fig. 4.21). The additional modes were due to the relative motion of grid points in the deforming grid. In the deforming grid case, at maximum amplitude grid points were compressed to fit between the deflected panel and the far field. This brought more grid points relatively closer to the panel surface and the higher dynamics of the flow field. In the static grid, the grid points were at a fixed distance from the panel surface (Fig. 4.2). In the transpiration boundary condition case, the far field grid points were 2.25 length units from the panel surface at all times. In the deforming grid case, at maximum amplitude, the far field grid points were 2.15 length units from the panel surface. This relatively closer distance resulted in a wider range of fluid dynamics seen by the far field grid points in the deforming grid case. This effect was similarly repeated in the grid points throughout the deforming region. The result was an increase in modes necessary to model the full-order solution.

Deforming Domain Evaluation: In model problems in which a static grid cannot be used, another method was needed to isolate the effect of deformation on the POD/ROM accuracy. By reducing the number of grid points that are allowed to deform, the accuracy

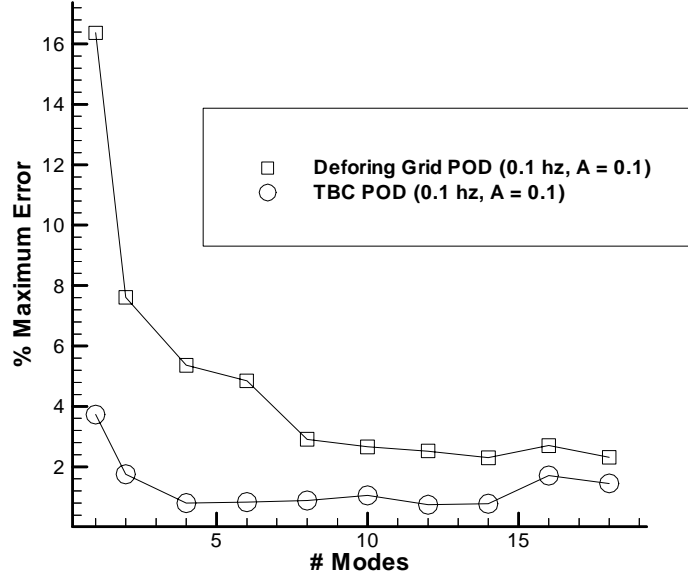


Figure 4.21 Maximum Density Error ($A = 0.1$, 0.1 hz)

Table 4.1 Effect on Error due to Grid Density

	# Moving Pts	% Max Error (2 modes)	% Max Error (10 modes)
100% Deforming Domain	600	7.76	3.52
15% Deforming Domain	100	5.64	3.37
Static Domain	0	1.99	1.67

trend could be observed. Two domains were evaluated: 100% and 15%. The 0.1 amplitude and 0.1 frequency case was used with 2 modes and 10 modes. (Tbl. 4.1). Maximum density error was evaluated.

As the number of modes increased, the difference between the two domains became insignificant ($> 0.5\%$). However, with fewer modes, the domain did have a small effect on accuracy (a reduction of 2.0% error from the 100% deforming domain to the 15% deforming domain. When compared to the static grid case, the trend is similar.

4.2.2 Blended POD/ROM. To evaluate the robustness of POD/ROM/DGs, snapshots were combined for a variety of frequencies to determine if a single POD/ROM/DG could be developed for all frequencies tested. Snapshots from an amplitude of 0.1 and

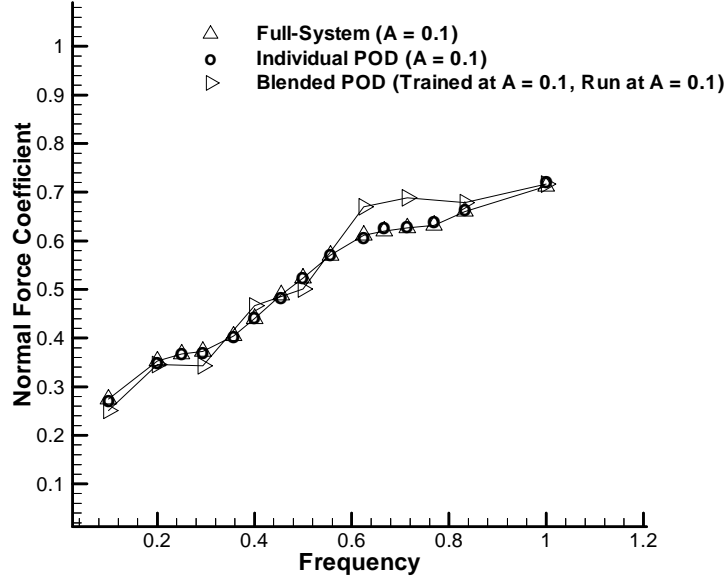
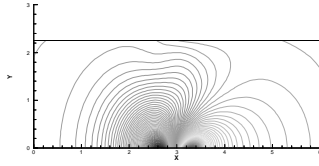
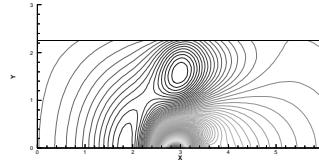


Figure 4.22 Minimum C_N (Blended POD, trained at $A = 0.1$, run at $A = 0.1$, 15 modes)

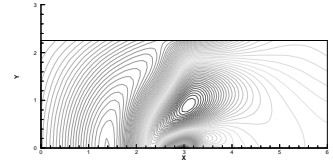
frequencies of 0.1, 0.2, 0.3, 0.4, 0.5, 0.6, 0.7, 0.8, and 1.0 were combined to create a POD/ROM/B10, in a technique called blending. 20 snapshots were taken for each frequency through a single oscillation, resulting in 180 snapshots for the blending. The POD/ROM/B10 was then run at the same frequencies and compared to the respective full-order at fully developed flow. The POD/ROM/B10 was stable at all frequencies (Fig. 4.22) but less accurate than the individual POD/ROM/DG, especially for the higher frequencies. The maximum density error for all frequencies was within 7%. The modes of the POD/ROM/B10 were again unique. The higher energy modes contained wave structures that appeared to be combinations of the wave forms seen in the individual POD/ROM/DG (Fig. 4.23). The primary mode contained 63% of the total eigenvalue energy. The remaining modes decreased in a fashion similar to the higher frequency individual POD/ROM/DG (Fig. 4.24). However, the slope of the POD/ROM/DB10 modal contribution was shallower than that of the individual POD/ROM/DGs, indicating more modes were necessary for an accurate solution.



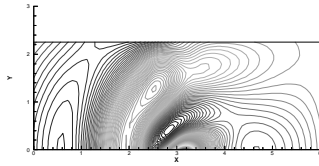
(a) Mode 1



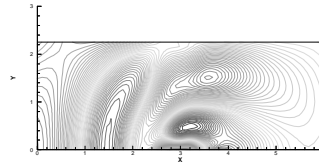
(b) Mode 2



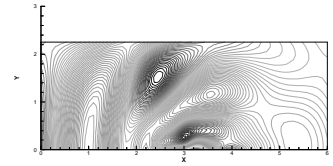
(c) Mode 3



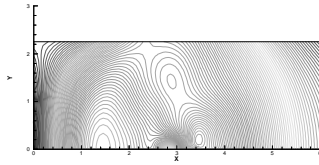
(d) Mode 4



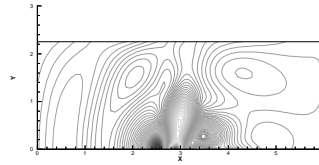
(e) Mode 5



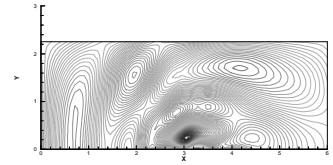
(f) Mode 6



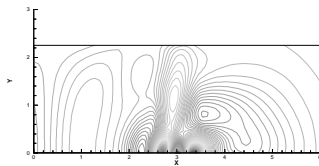
(g) Mode 7



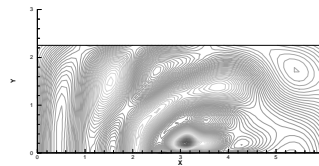
(h) Mode 8



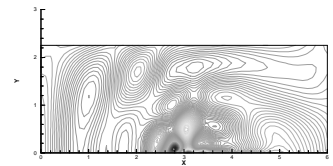
(i) Mode 9



(j) Mode 10



(k) Mode 11



(l) Mode 12

Figure 4.23 POD/ROM/B10 (Blended, $A = 1.0$)

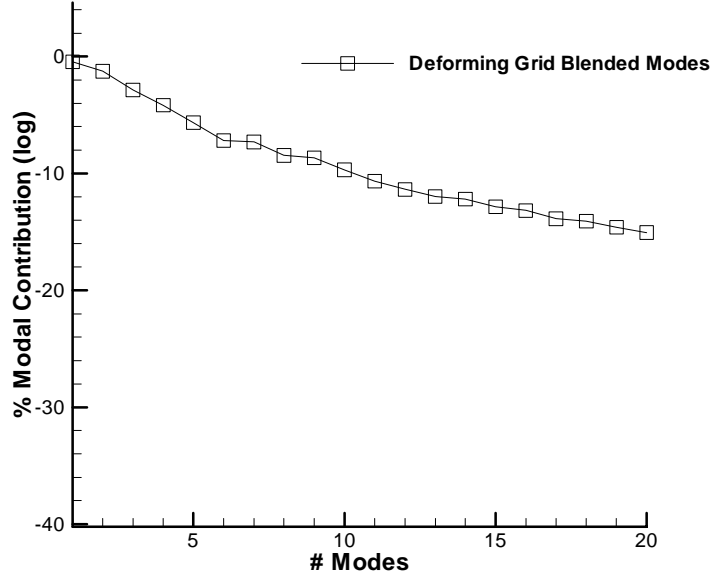


Figure 4.24 POD/ROM/B10 Modal Contribution

4.2.3 Amplitude Variation. To evaluate changes in deformation on the accuracy of deforming grids, the blended POD/ROM trained at an amplitude of 0.1 was run at amplitudes of 0.05 and 0.15. This provided a $\pm 50\%$ variation in the grid deformation. The blended POD/ROM run at the lower amplitude of 0.05 was only slightly less accurate than that run at the amplitude at which it was trained (Fig. 4.25). The maximum density error was 5% for all frequencies. The blended POD/ROM run at the higher amplitude of 0.15 was much less accurate than that run at the amplitude for which it was trained (Fig. 4.26). The maximum density error for all frequencies was $\pm 12\%$. These amplitude variation errors were due to the modes being applied at inappropriate physical locations. To create a single model, a blended POD/ROM using the snapshots from 0.05, 0.1, and 0.15 with all frequencies, was developed. This single model was unstable at all amplitudes and frequencies due to the fact that the modes combined across amplitudes were being applied at inappropriate physical locations. This highlights the issue with deforming grid POD/ROM; snapshots of differing deforming grids cannot be easily combined to produce a blended POD/ROM. As a result some new technique was required.

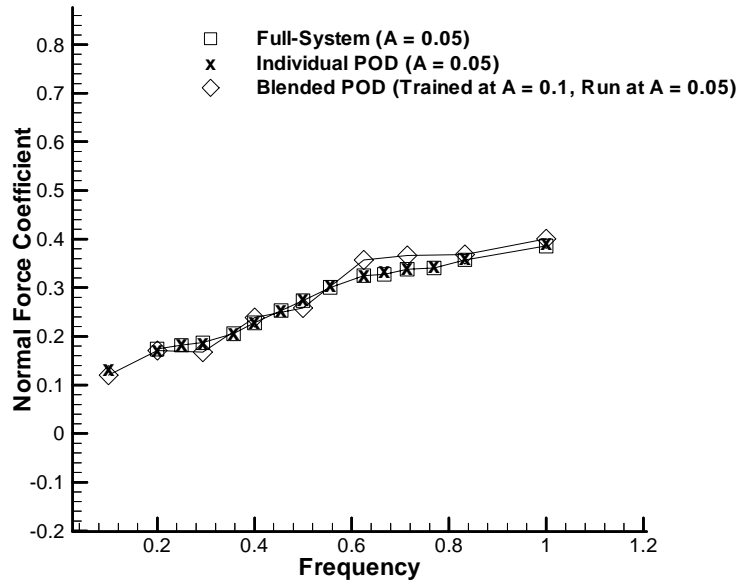


Figure 4.25 Minimum C_N (Blended POD, trained at $A = 0.1$, run at $A = 0.05$, 15 modes)

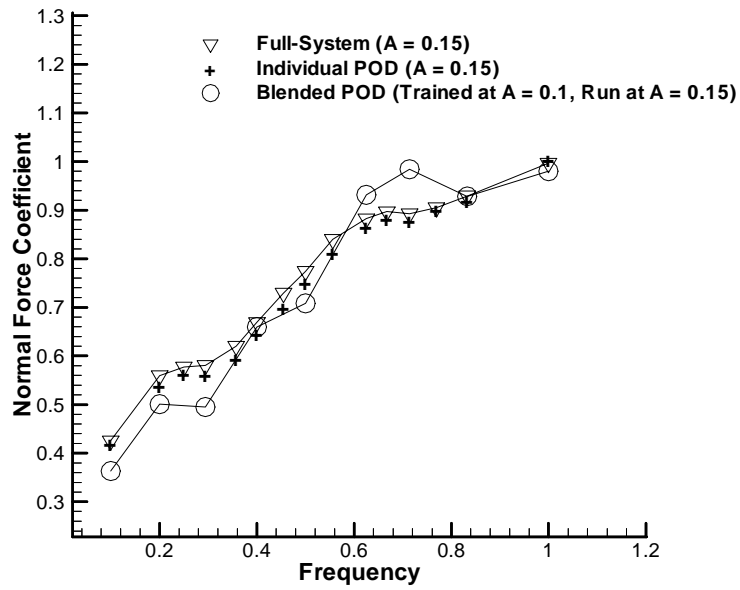


Figure 4.26 Minimum C_N (Blended POD, trained at $A = 0.1$, run at $A = 0.15$, 15 modes)

4.3 Multi-POD

To create a more robust model, a technique that used multiple POD/ROM/B was developed (Multi-POD). In this technique, several independent POD/ROM/DG were developed at various sets of grid deformations. Blended POD/ROM were then created by combining snapshots for the POD/ROM/DG. POD/ROM/B tend to be more effective than individual POD/ROM/DG because they are more robust to variations in input parameters. The accuracy of the Multi-POD is dependant on the accuracy of the POD/ROM/B. Blending was not effective over variations in grid deformations due to the changes in the grid point locations caused by the grid deformation, as seen in the pervious section. Using the deforming grid metric of the L_2 error norm, several POD/ROM/B were used for a single model that had a variety of deformations. As the deformation progressed, the L_2 error norm deforming grid metric was automatically checked. When a user-defined level was exceeded, the algorithm automatically switched to a new POD/ROM/B, more appropriate to the current deformations.

As an example, the amplitude variation errors in the POD/ROM/B10, created in the previous section, when it was run at different amplitudes could be correlated to the differences in the training grids to the run grids. The L_2 norm of the grid error was well correlated to the POD/ROM/B10 error (Fig. 4.27). As the run grids deviated from the training grids, the overall POD/ROM/B10 accuracy decreased, as shown by the L_2 norm leading the density error. The L_2 norm was scaled by 100 to allow a visual comparison. For this model problem, L_2 norms of the grid error of around 0.065 produced maximum density errors of 8.5%. As a comparison, the transpiration boundary condition case would have a grid error of zero at all times, providing no chance to correlate the errors. The L_2 norm of the grid error was provided to the user as a flag on the accuracy of the POD/ROM for the deforming grid.

To test the Multi-POD technique, two blended POD/ROMs, trained at amplitudes of 0.05 and 0.15 (POD/ROM/B5 and POD/ROM/B15), were used to model amplitude deflections from 0.05 to 0.15. In this example, the problem was run at an amplitude of 0.05 for five oscillations, then 0.15 for five oscillations. Starting with POD/ROM/B5, the model proceeded up to an amplitude of approximately 0.1. At this point, the L_2 error

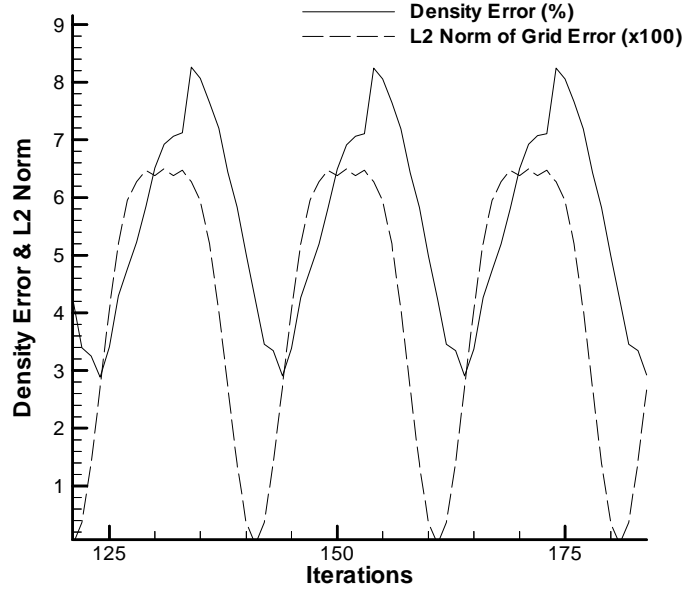


Figure 4.27 Corrolated Grid Error and Density Error, after 8 oscillations (Blended POD, trained at $A = 0.1$, run at $A = 0.15$, 15 modes)

norm exceeded the preset level and POD/ROM/B15 took over. When compared to a single blended POD/ROM (trained at an amplitude of 0.1), the Multi-POD was more accurate (Fig. 4.28). The density error of the POD/ROM/B10 exceeded 8% while the Multi-POD remained below 5%. The L_2 error norm clearly identified the point at which a change in POD/ROM was necessary as shown by the sudden increase in the L_2 error norm plot. This technique required more snapshots than the single blended POD/ROM (double in this example). However, it does provide for a more robust algorithm that can be applied in a design environment. With the multi-POD technique, the entire design space for the example is well modeled with a single algorithm containing two POD/ROMs.

4.4 Conclusions

POD/ROM was shown to be sensitive to grid deformation. When compared to a rigidly attached grid, the deforming grid required more modes for an accurate solution. The relative motion of grid points due to the deformation created modes that did not exist

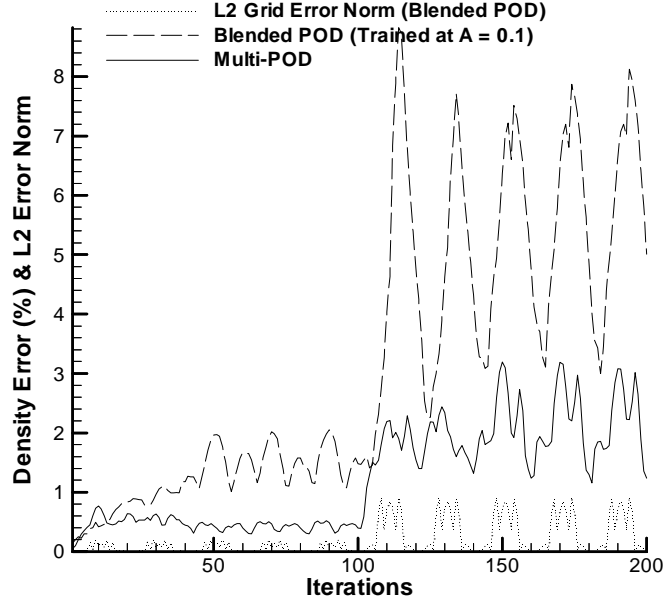


Figure 4.28 Multi-POD (Two POD; trained at $A = 0.1$ and $A = 0.15$, 15 modes)

in the fluid dynamics. The index-based computation of POD/ROM could not account for such changes in grid dynamics.

POD/ROM was shown to accurately reproduce flow solutions with deforming grids for a problem with coupled fluid and grid dynamics. Errors in fluid variables were less than 5% of the full-order system, and thus represent a reasonable level of accuracy for design. POD/ROM accurately reproduced the flow field when applied to a deforming grid model problem when the run grid was identical to the training grid. The maximum density error was 3% for only 15 modes. POD/ROMs of deforming grids required more modes for accuracy than those of static grids, for similar model problems. The additional modes were attributed to the relative motion of the grid points with respect to the boundaries and each other. However, the overall number of modes required for the deforming grid was still relatively small, reducing the order of the problem from 2400 to 15 dof.

The magnitude of the deforming domain provided a technique for evaluating the accuracy of POD/ROM on deforming grids. As the domain was reduced, the accuracy increased for a similar number of modes. The trend became constant as the domain reduced,

indicating the number of modes that were associated primarily with grid deformation. This constant was similar to that of the static grid case.

When the modes were applied at grids that differed from the training grids, POD/ROM accuracy degraded. A POD/ROM trained at 0.1 amplitude and run at 0.15 amplitude had errors of $\pm 12\%$ in maximum density. A metric was developed to track the relative difference in training grids and run grids. A pseudo-inverse technique was implemented from a grid modal matrix based on the training grids and an error term created. The L_2 norm of the error in deformation correlated well with the resulting POD/ROM error. The metric was used interactively to evaluate the accuracy of the deforming grid POD/ROM. A new multi-POD technique was developed to use the grid metric to determine when to switch between POD/ROM of different deforming grids. The complete algorithm used the most appropriate POD/ROM for a variety of grid deformations to provide the most accurate solution.

V. Pitching and Plunging Airfoil

To examine the utility of the Multi-POD technique with a deforming grid, a pitching and plunging airfoil with a loosely coupled structural model governing the pitch and plunge degrees of freedom was analyzed. The structural model allowed the aerodynamics to alter the grid deformation by movement of the structure through imposed air loads. This free pitching and plunging required that the Multi-POD technique be capable of selecting the best available POD/ROM for cases where the pitch and plunge were not well represented in the training. The training of the POD/ROM was performed without the structural model, using cases for which pitch and plunge was forced.

5.1 Application

The application of full-potential flow over a 2-D pitching and plunging airfoil was used to examine the robustness of the Multi-POD technique (Fig. 5.1). Two cases were examined: forced oscillation and free pitch and plunge. For both cases, a NACA 0012 airfoil was used. The airfoil was pitched about the quarter chord point.

The density and velocity were non-dimensionalized using the far-field density, ρ_∞ , and velocity, U_∞ . Pressure was non-dimensionalized using the far-field dynamic pressure, P_∞ (subsequent references to variables assume non-dimensional forms). For both cases, the freestream Mach number was set to 0.5 to prevent the flow over the airfoil from becoming supersonic.

5.1.1 Forced Oscillation Case. In the Forced Oscillation case, both plunge, $h(t)$, and pitch, $\alpha(t)$, were varied in a sinusoidal fashion;

$$\alpha(t) = (\alpha_0 + \alpha_{\max}) \left[\sin \left(2\pi f \frac{t}{t_{\max}} \right) \right], \quad (5.1)$$

$$h(t) = h_{\max} \left[\sin \left(2\pi f \frac{t}{t_{\max}} \right) \right]. \quad (5.2)$$

α_0 was the initial conditions, α_{\max} and h_{\max} were the maximum pitch angle and plunge, f was the non-dimensional frequency of oscillation, t was the time, and t_{\max} the maximum time for the test. The pitching and plunging was synchronous, with the pitch angle zero

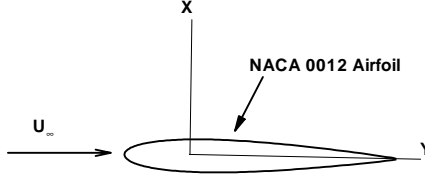


Figure 5.1 Pitching and Plunging Airfoil Model Problem

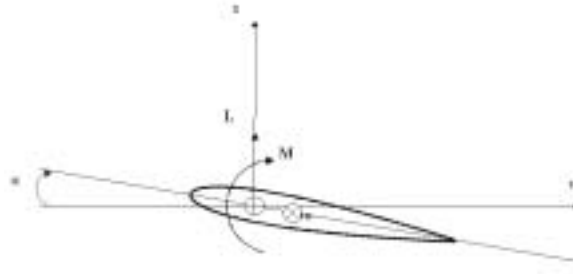


Figure 5.2 Pitching and Plunging 2-D System

at minimum and maximum deflection. The grid was deformed by determining the pitch and plunge of the airfoil and then analytically solving for the grid-points from the airfoil surface to the fixed far-field. For the forced case, the pitch and plunge was explicitly known and not dependant on the fluid dynamics.

5.1.2 Free Pitch and Plunge Case. For the free pitch and plunge case, the structural model was a simple, 2-D, spring model that was loosely coupled to the fluid dynamics model (Fig. 5.2). The fluid dynamics model generated the coefficients of lift and moment. The structural model then used the fluid dynamics loads to determine incremental motion of the airfoil. This model allowed an evaluation of the POD/ROM with the structural dynamics and grid motion fully linked. The airfoil was free to rotate in the $x-y$ plane and free to translate up or down, about the quarter chord point. The motion

of the airfoil was limited by spring effects in torsional and translational displacement. The equations governing the motion of the system are,

$$\ddot{h} + \frac{x_\alpha}{2}\ddot{\alpha} + 2\zeta_h c_2 \dot{h} + c_2^2 h = \frac{2}{\mu_s \pi} C_l \quad (5.3)$$

$$x_\alpha \ddot{h} + \frac{r_\alpha^2}{2}\ddot{\alpha} + \frac{2\zeta_\alpha r_\alpha^2}{\bar{u}}\dot{h} + c_1(\alpha - \alpha_0) = \frac{4}{\mu_s \pi} C_{m_{ea}}. \quad (5.4)$$

where, $c_1 = \frac{1}{2} \left(\frac{2}{\bar{u}}\right)^2 r_\alpha^2$ and $c_2 = \left(\frac{2}{\bar{u}}\right) \left(\frac{\varpi_h}{\varpi_\alpha}\right)$, $\bar{u} = \frac{U_\infty}{b\varpi_\alpha}$, and x_α is the distance from the center of mass to the pitch point, scaled by the semi-chord. The pitch and plunge natural frequencies are defined as, $\varpi_\alpha = \sqrt{\frac{K_\alpha}{I_\alpha}}$ and $\varpi_h = \sqrt{\frac{K_h}{M}}$. The linear and torsional springs are modeled with stiffness coefficients, K_h and K_α , and damping coefficients, D_h and D_α . The static pre-twist, α_0 , defines the unloaded position of the torsional spring. The radius of gyration is, $r_\alpha^2 = \sqrt{\frac{I}{m}}$. The three remaining parameters are the mass ratio, $\mu_s = \frac{m}{\pi \rho_\infty b^2}$, and the damping ratios, $\zeta_\alpha = \frac{D_\alpha}{2\sqrt{I_\alpha K_\alpha}}$ and $\zeta_h = \frac{D_h}{2\sqrt{m K_h}}$. These equations can be rewritten as a system of first-order differential equations by setting $y_1 = h$, $y_2 = \dot{h}$, $y_3 = \alpha$, and $y_4 = \dot{\alpha}$. Following the approach of Beran and Morton (42), with $\det \equiv \frac{1}{2}(r_\alpha^2 - x_\alpha^2)$,

$$\mathbf{S} = f(\mathbf{S}, C_l, C_{m_{ea}}, \bar{u}) = \mathbf{M}^{-1}\mathbf{Q} - \mathbf{M}^{-1}\mathbf{K}\mathbf{S}. \quad (5.5)$$

$$\mathbf{S} = \begin{bmatrix} h \\ \dot{h} \\ \alpha \\ \dot{\alpha} \end{bmatrix}, \quad (5.6)$$

$$\mathbf{M}^{-1} = \frac{1}{\det} \begin{bmatrix} \det & 0 & 0 & 0 \\ 0 & \frac{1}{2}r_\alpha^2 & 0 & -\frac{1}{2}x_\alpha \\ 0 & 0 & \det & 0 \\ 0 & -x_\alpha & 0 & 1 \end{bmatrix}, \quad (5.7)$$

Table 5.1 PAPA Structural Model Parameters

x_{cg}	x_α	$\zeta_h = \zeta_\alpha$	$\frac{\varpi_h}{\varpi_\alpha}$	r_α^2	μ_s	M_∞	α_0
0.5	-0.25	0.0	1.0	0.25	125	0.5	0

$$\mathbf{Q} = \begin{bmatrix} 0 \\ \frac{2}{\mu_s \pi} C_l \\ 0 \\ \frac{4}{\mu_s \pi} C_{m_{ea}} + c_1 \alpha_0 \end{bmatrix}, \quad (5.8)$$

$$\mathbf{K} = \begin{bmatrix} 0 & -1 & 0 & 0 \\ c_2^2 & 2\zeta_h c_2 & 0 & 0 \\ 0 & 0 & 0 & -1 \\ 0 & 0 & c_1 & \zeta_\alpha \left(\frac{2}{u}\right) r_\alpha \end{bmatrix}. \quad (5.9)$$

The above equations may then be then solved using a four-stage Runge-Kutta method. In the structural model, the parameters used were selected to closely match the forced oscillation case in terms of amplitude and frequency (Tbl. 5.1).

The grid was deformed based on the pitch and plunge generated from the above equations and the air loads calculated from the fluid dynamics model. This implicitly linked the fluid dynamics and grid motion. The structural solver was validated using computational data (see Appendix D).

5.1.3 Computational Grid. For both cases, a C-grid was used with a wake cut along the trailing edge that extended to the outflow boundary (Fig. 5.3). The trailing edge of the airfoil was closed. The chord length, c , was normalized to a value of 1.0. The far field was placed at 10 chord lengths from the airfoil. 251×50 grid points were used for the model problem, with 150 grid points spaced on the panel surface. The spacing of the grid at the airfoil surface was 0.05 of the chord length. The grid was smoothed with an elliptical solver that used a tension spline to prevent grid line crossing (Fig. 5.4).

5.1.4 Domain Filtering. In POD/ROM, the most accurate solution is typically generated by the most independent modes. However, with a large region of nearly constant

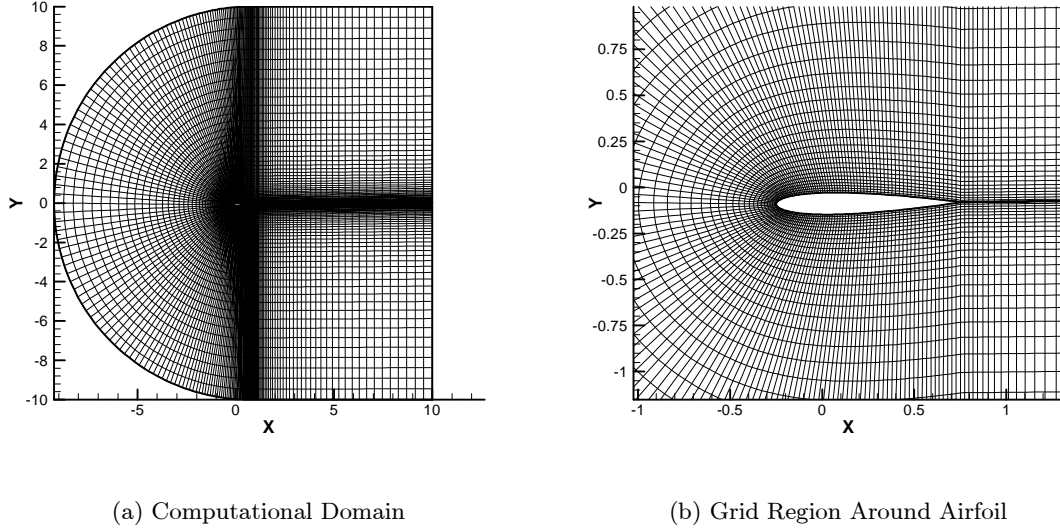
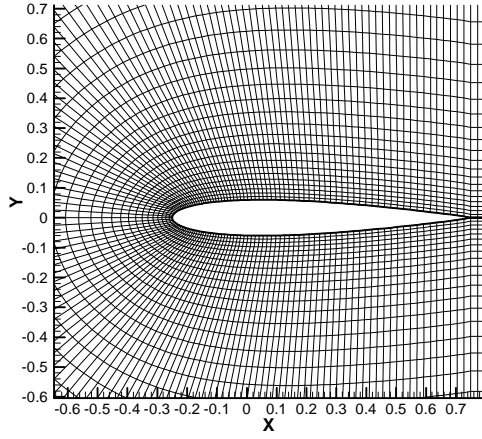


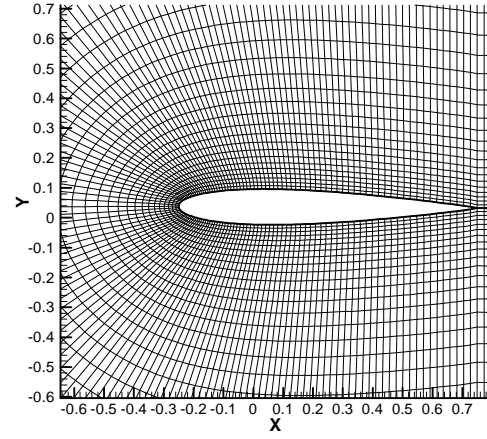
Figure 5.3 C-Grid

flow, large numbers of modes can generate numerical errors. An approach to dealing with this numerical error is to sub-divide the computational domain. For the regions of highest interest (near field), more modes were used. For areas of lower interest (intermediate field), fewer modes were needed. In areas of little change from the freestream (far field), only a few modes were necessary (Fig. 5.5).

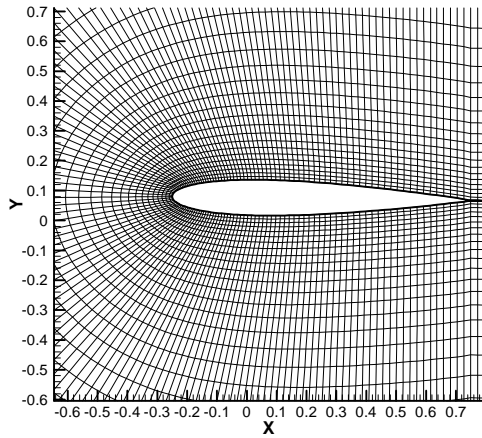
To implement this, a domain-based filtering of the POD modal matrix, Φ , was performed. For the grid-point locations to be filtered, the value of Φ corresponding to the appropriate modes, was set to zero. This truncated the number of modes being applied to various regions of the computational domain. In the near field, the number of modes varied depending on the complexity of the fluid flow (see POD/ROM Results for numbers of modes). For both the intermediate and far fields, it was determined through trial and error the number of modes necessary for an accurate solution. If there was too large a variation in number of modes from the near field to the intermediate field, errors would develop along the internal boundary. In the intermediate field, only 10 modes were necessary. For the far field, only 2 modes were necessary. This domain filtering technique differs from the Domain Decomposition technique of Lucia et al. (43), in that only one POD/ROM was



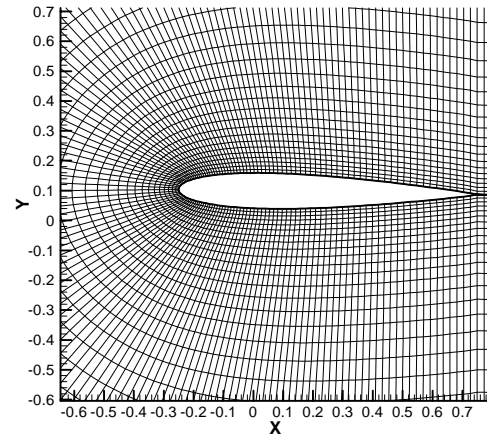
(a) $t = 1$



(b) $t = 2$



(c) $t = 3$



(d) $t = 4$

Figure 5.4 Example of Grid Deformation ($h_{\max} = 0.1$, $a_{\max} = 2.0$ deg)

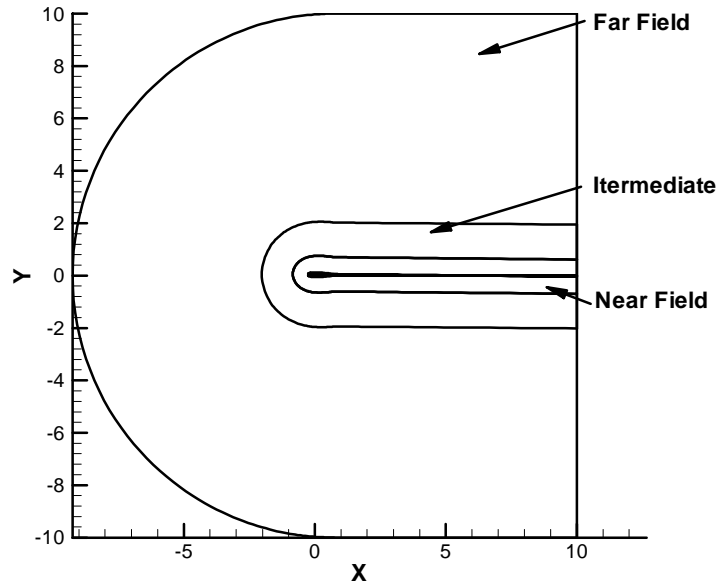


Figure 5.5 Grid Domains

generated for the entire domain. However, the technique of domain filtering required more computations during the actual run time.

Other forms of filtering the domain include weighted filtering. In weighted filtering, the modes are multiplied by weighting factors that decrease with radial distance from the airfoil. In effect, the domain filtering technique is a binary weighted filtering. Weighted filtering could be explored but was not necessary for this model problem.

5.1.5 Full-Order Results for Forced Oscillation. A wide range of input parameters was evaluated. Maximum pitch was varied from 0 to 2.0 degrees in 0.5 degree increments. Maximum plunge was varied from 0 to ± 0.2 of chord length, in 0.05 increments. Oscillation frequency, f , was varied from 0.002 to 0.01, in 0.002 increments. This provided 125 different combinations of input parameters. The model problem showed non-linear behavior in both maximum plunge and maximum pitch. The maximum lift coefficient, C_l , determined after the flow was fully developed, was used as a way to evaluate the non-linear nature of the model problem. Examining the case with maximum plunge of 0.2 and varying pitch magnitude and frequency, the model problem can be seen to be non-linear in pitch for

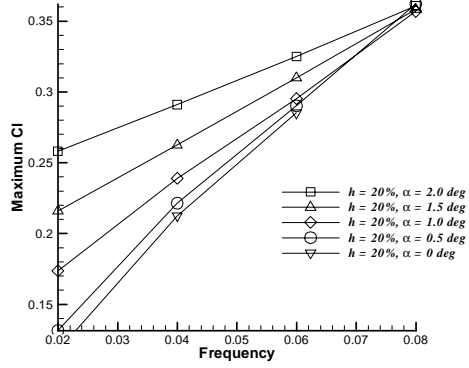
the lower frequencies (Fig. 5.6). As the oscillation frequency increased, the plunge rate became more significant, overshadowing the pitch. Examining the case with maximum pitch of 2.0 degrees and varying plunge and frequency, the model problem can be seen to be non-linear in plunge as well. The rate of plunge causes the apparent angle of attack to be increased with respect to the freestream flow (Fig. 5.7).

5.2 *POD/ROM Results*

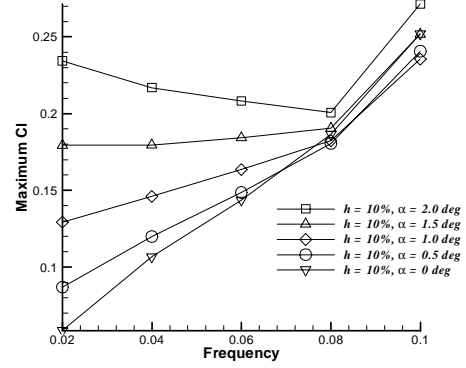
POD/ROMs were created from the forced oscillation cases and then applied to both the forced and free dynamics. Individual and blended POD/ROMs were compared to the forced oscillation case. Then, blended POD/ROMs and Multi-POD were compared to the free pitch and plunge case.

5.2.1 Individual POD/ROM. Individual POD/ROMs were constructed for the full-order solutions computed at pitch angles, $\alpha_{\max} = 0.0 - \pm 2.0$ deg in 0.5 deg increments and plunge depths $h_{\max} = 0.0 - \pm 0.2$ in increments of 0.05 for oscillation frequencies of $f = 0.02 - 0.1$ in increments of 0.02. These parameters gave a varied design space with sufficient non-linear variation in behavior to rigorously test POD/ROM with deforming grids. A total of 125 separate POD/ROMs were developed. The individual POD/ROMs were trained for two oscillations and 50 snapshots were taken during the training period. The POD/ROMs were then compared to their respective full-order solutions for fully developed flow (that occurred after approximately 10 oscillations).

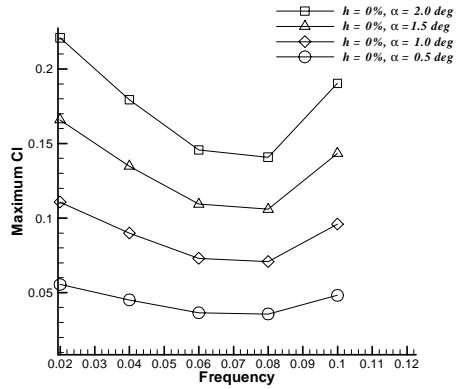
The individual POD/ROMs were able to reproduce the flow field using just 20 modes to an accuracy of 5%, based on density throughout the flow-field. This equated to an order reduction from 12550 to 20 dof. The POD/ROMs were able to capture the non-linearities in both pitch and plunge with excellent accuracy (Figs. 5.8 and 5.9). The lift coefficient was reproduced to an accuracy of 8%. The primary modes of all of the individual POD/ROMs were very similar in magnitude, however, the modal shapes were very different. For low frequency cases ($f = 0.02$ and 0.04) the modes were simpler with little data in the near and far-fields. For the higher frequency cases, the modes showed more information in the far-field. In the case of varying pitch, frequency of plunge determines the mode shapes. For



(a) $h_{\max} = 20\%$

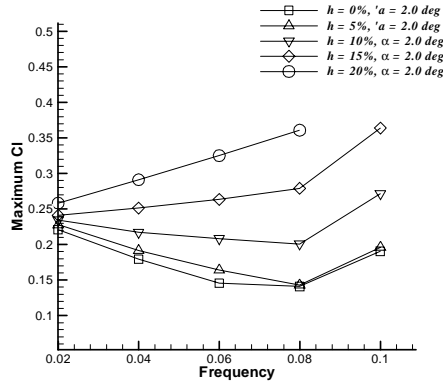


(b) $h_{\max} = 10\%$

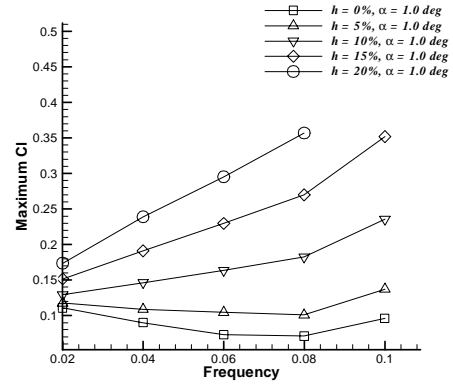


(c) $h_{\max} = 0\%$

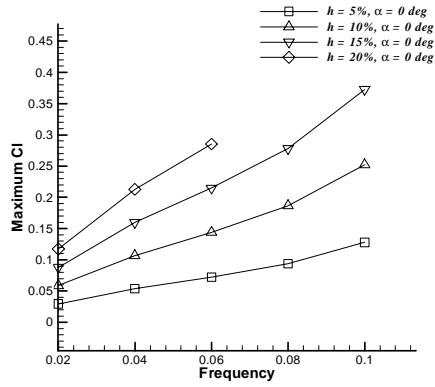
Figure 5.6 Full-Order (Fixed Plunge, Varying Pitch)



(a) $\alpha_{\max} = 2.0$

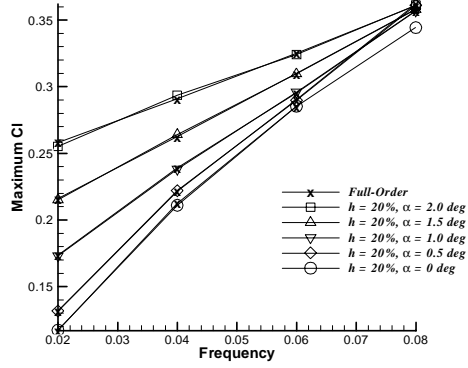


(b) $\alpha_{\max} = 1.0$

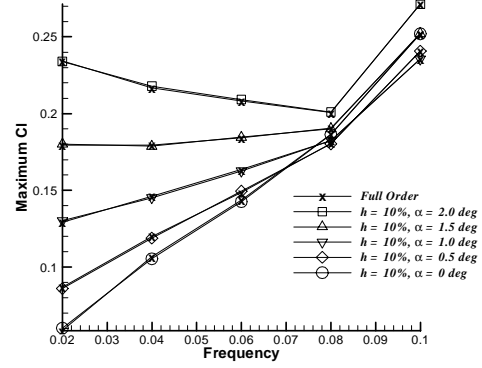


(c) $\alpha_{\max} = 0.0$

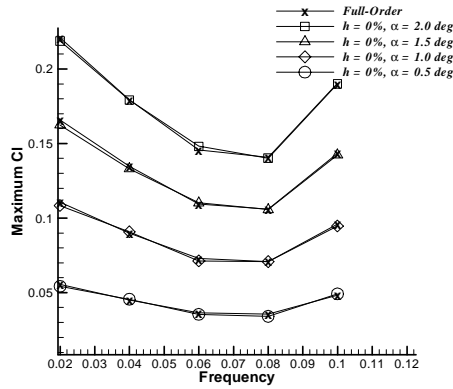
Figure 5.7 Full-Order (Varying Plunge, Fixed Pitch)



(a) $h_{\max} = 20\%$

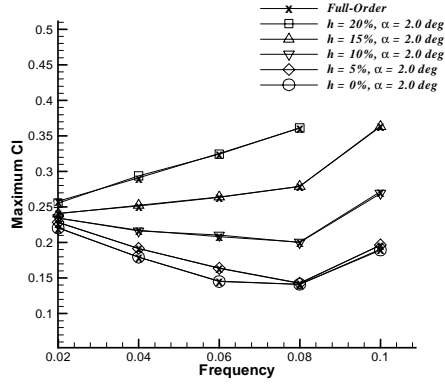


(b) $h_{\max} = 10\%$

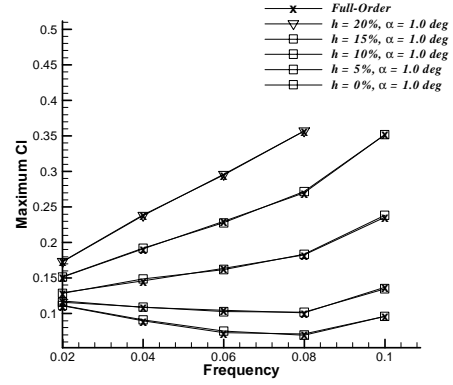


(c) $h_{\max} = 0\%$

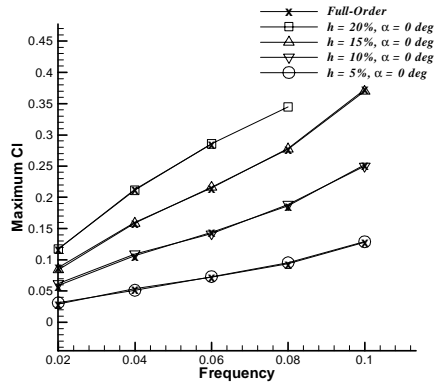
Figure 5.8 Individual POD/ROM (Fixed Plunge, Varing Pitch, 20 modes)



(a) $\alpha_{\max} = 2.0$



(b) $\alpha_{\max} = 1.0$



(c) $\alpha_{\max} = 0.0$

Figure 5.9 Individual POD/ROM (Varying Plunge, Fixed Pitch, 20 modes)

lower frequencies the modes were similar. However, as the frequency increases the modes changed significantly (Figs. 5.10 and 5.11). A similar result was seen in the frequency of pitch. The pitch angle had a less significant impact on the modal shapes. (See Appendix E. for additional modal shape comparisons). The first three modes for all cases had similar magnitude modes (Fig 5.12). The modal contribution for the remaining modes depended on the complexity of the modes. If the modes were less complex, such as in a lower frequency pitch and plunge case, the majority of the modal energy was contained in the primary mode. However, if the modes were more complex, the modal energy is spread out over more modes.

5.2.2 Blended POD/ROM. Blended POD/ROMs were constructed from the individual POD/ROM for plunge depths of $h_{\max} = 0.0$, POD/ROM/B0, $h_{\max} = 0.1$, POD/ROM/B10, and $h_{\max} = 0.2$, POD/ROM/B20. The snapshots for the various oscillation frequencies and pitch angles were combined for each of the three plunge depths. The blended POD/ROMs were then run at the same frequencies and compared to the respective full-order solution at fully developed flow. The maximum flow-field density error of the blended POD/ROMs over their range of oscillation frequency and pitch angle, was within 6% and the lift coefficient accuracy was within 10% using 20 modes (Fig 5.13).

If a blended POD/ROM was run on a grid that did not match it's training grid, the solution was very poor. The results of POD/ROM/B0 when run at $h_{\max} = 0.1$, $f = 0.06$, and $\alpha = 1.0$ deg were very unstable (Fig 5.14). POD/ROM/B0 was unable to accurately reproduce the non-linear behavior of the full-order system and became more unstable as the frequency was increased. The maximum C_l was damped for all frequencies and shifted dramatically as a result of the modes being applied at inappropriate physical locations.

The accuracy of the blended POD/ROM depended on the number of modes used. For the more quasi-steady cases, fewer modes could be used to obtain a reasonable accuracy. In the more non-linear cases, more modes were necessary. POD/ROM/B0, required 10 modes for an accurate solution. POD/ROM/B10 required 15 modes and POD/ROM/B20 needed 25 modes (Fig 5.15). The blended POD/ROM showed significant structures in the far-field where the fluid dynamics was in fact quite small. This was due to blended over

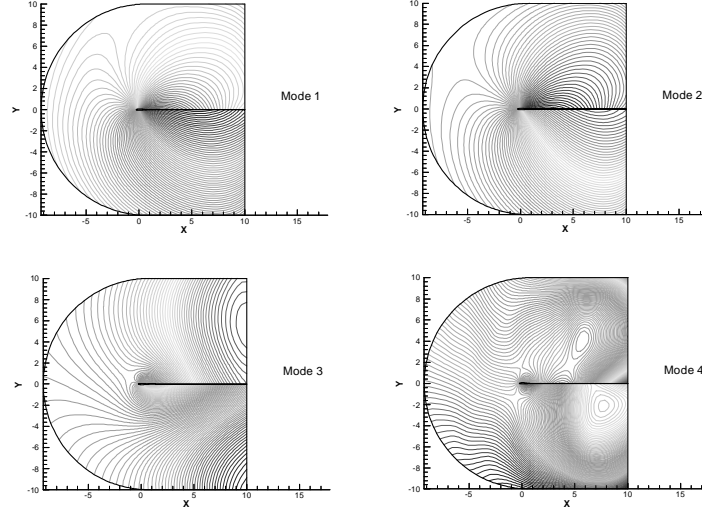


Figure 5.10 Individual POD/ROM Modes ($h_{\max} = 0\%$, $\alpha_{\max} = 1.0$ deg, $f = 0.02$)

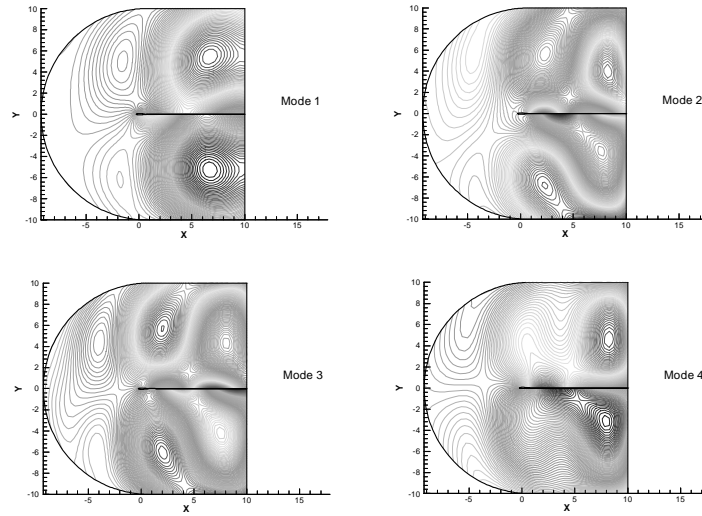


Figure 5.11 Individual POD/ROM Modes ($h_{\max} = 0\%$, $\alpha_{\max} = 1.0$ deg, $f = 0.1$)

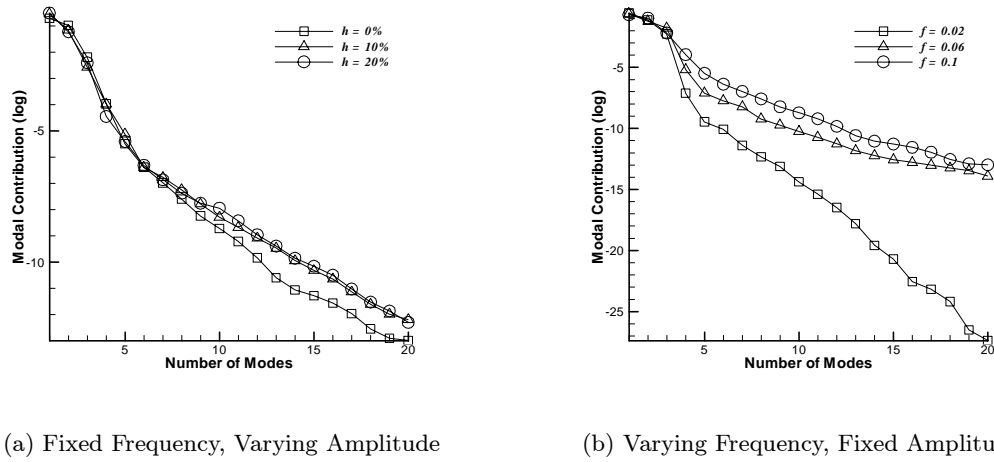
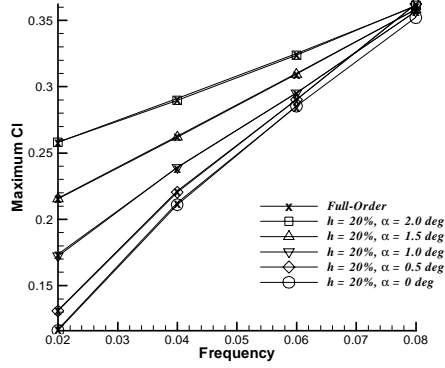


Figure 5.12 Individual POD/ROM Modal Contributions

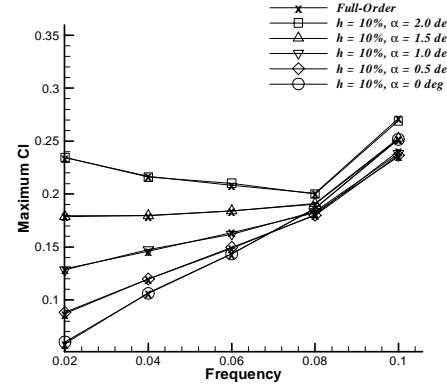
Table 5.2 Computation Times vs. Number of Modes

	100 Iterations (sec)
full-order	100
5 Modes	53
10 Modes	71
15 Modes	94
20 Modes	128
25 Modes	145
30 Modes	223

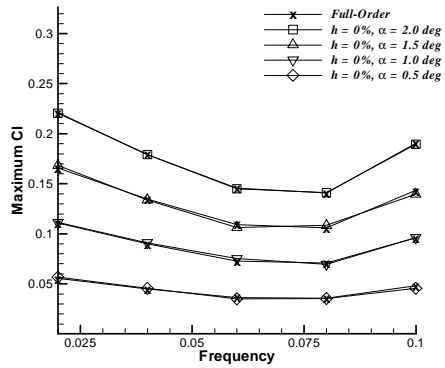
the higher frequency cases that had modes with data in the far-field. While the individual POD/ROM were able to cancel out the modes in the far-field, the blended POD/ROM were not. These blended far-field structures resulted in increasing numerical error in the higher modes. Thus, a practical limit was seen in the number of modes that could be used in a POD/ROM. This was seen when increasing the number of modes actually increased the error. The fewer the modes used in the blended POD/ROMs, the faster the computation of the reduced order model. Tbl. 5.2 shows the computation time for 100 iterations with 5 sub-iterations, on a Pentium III, 933 Mhz, with 512 MB of memory. Therefore, it was more computationally efficient to use blended POD/ROM with the appropriate number of modes.



(a) $h_{\max} = 20\%$



(b) $h_{\max} = 10\%$



(c) $h_{\max} = 0\%$

Figure 5.13 Blended POD/ROM (Fixed Plunge, Varying Pitch, 25 Modes)

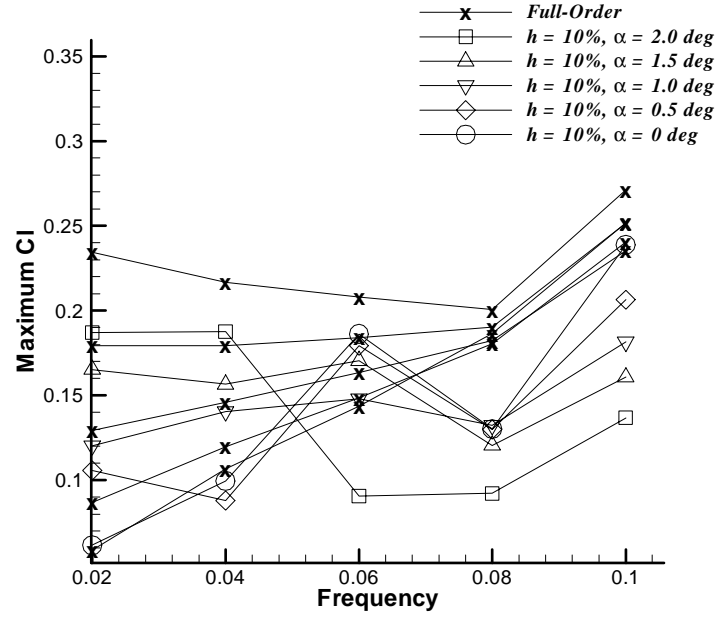


Figure 5.14 Blended POD/ROM (Trained at $h = 0\%$, Run at $h = 10\%$, $f = 0.06$, $\alpha = 1.0$ deg, 25 modes)

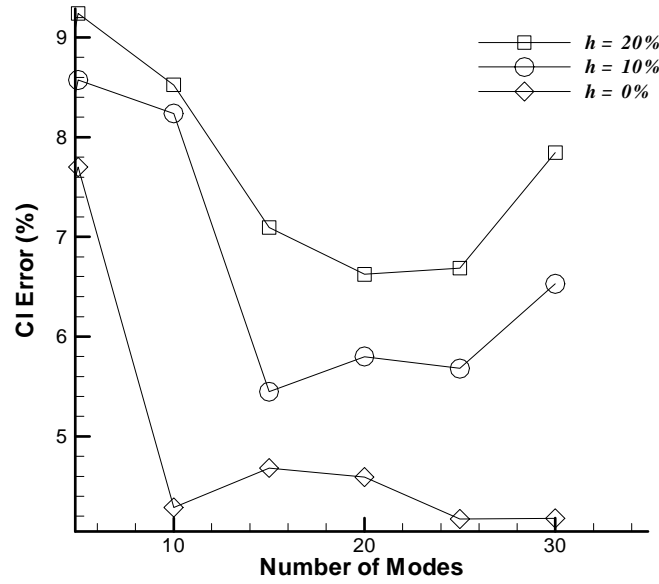


Figure 5.15 Blended POD/ROM Accuracy vs. Number of Modes

The modes of the blended POD/ROMs were more complex than that of the individual POD/ROMs, with large structures in the first eight modes (see Figs. 5.16 to 5.18). The modes showed more structure in the far field. As a result of the large structures in the far-field, the POD/ROM/B were more sensitive than the individual POD/ROM/DG to numerical errors caused by using too many modes. Thus, domain filtering was vital for an accurate solution using blended POD/ROM. The energy of the modes was concentrated in all cases in the first four modes (see Fig. 5.19). For POD/ROM/B20, the remaining modes seemed to drop off quickly in energy content, however, the modes were still vital to an accurate solution. This is due to the fact that more energy is contained in the first four modes than in any other case. For POD/ROM/B10, the modes dropped off in energy more slowly, more like in the case of the individual POD/ROMs.

5.2.3 Multi-POD. To determine the utility of Multi-POD for a practical problem, the blended POD/ROM created using forced pitch and plunge were applied to the free pitch and plunge cases. The three blended POD/ROMs were assigned thresholds for the L_2 of the deforming grid metric. 10 Modes were used for POD/ROM/B0, 15 for POD/ROM/B10 and 20 for POD/ROM/B20.

For the damped case, the model was run with $\bar{u} = 2.0$ and the Multi-POD compared to the full-order solution. The Multi-POD switched to POD/ROM/B0 very quickly as the airfoil came down from $\alpha = 1.0$ deg and then held there until it was fully damped (see Fig. 5.20). The Multi-POD was able to damp the solution but did not match the time accurate response in every detail. The phase of the motion of the pitch and plunge matched well, but the amplitudes of both pitch and plunge were larger than that of the full order solution. The Multi-POD was exact at steady state (fully damped). To test how well a single POD/ROM would have performed, the same test was executed with the POD/ROM/B10. The solution was less accurate during the unsteady portion of the time dependent solution, but exact at steady state (fully damped).

The unstable oscillation case was more challenging. The model was run with $\bar{u} = 5.0$ and the Multi-POD compared to the full-order solution. The Multi-POD started with the POD/ROM/B0 and switched as the amplitude varied slowly to POD/ROM/B10. The

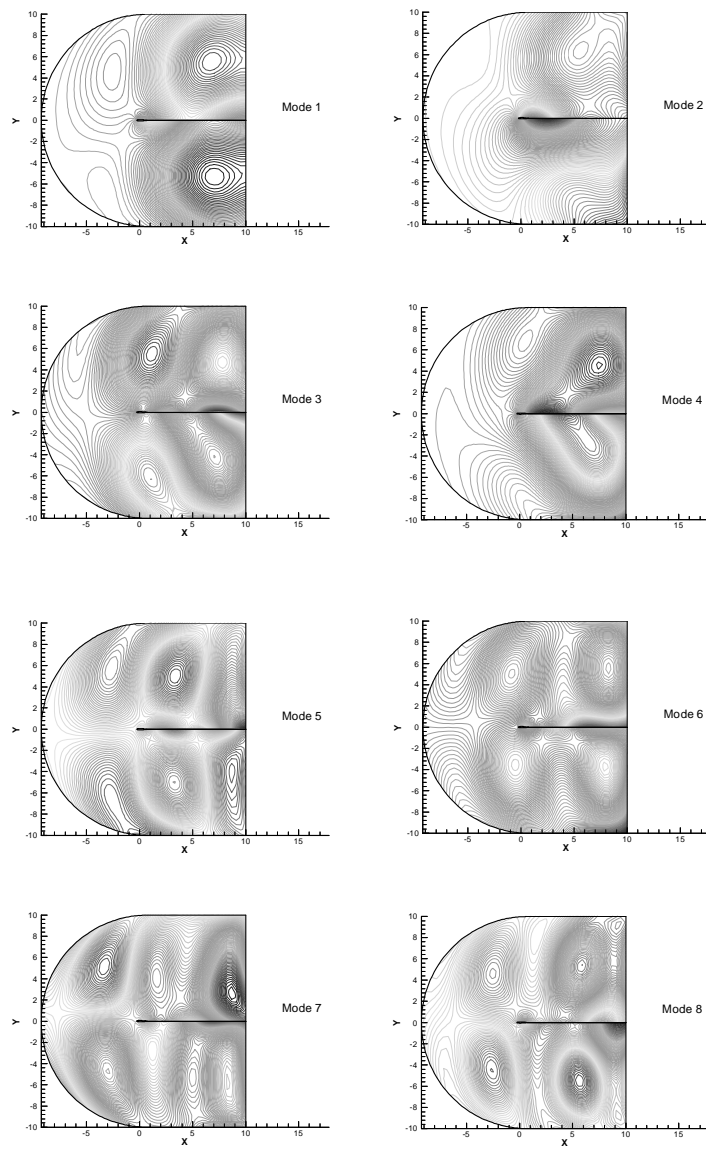


Figure 5.16 Blended POD/ROM Modes ($h_{\max} = 0\%$)

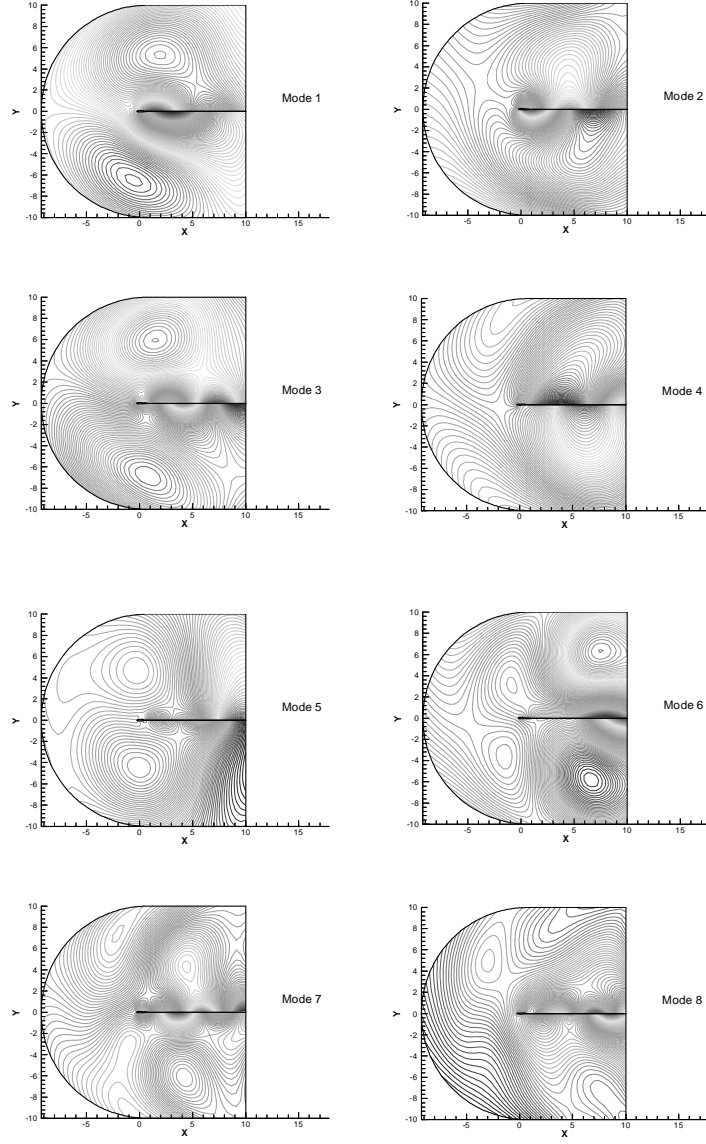


Figure 5.17 Blended POD/ROM Modes ($h_{\max} = 10\%$)

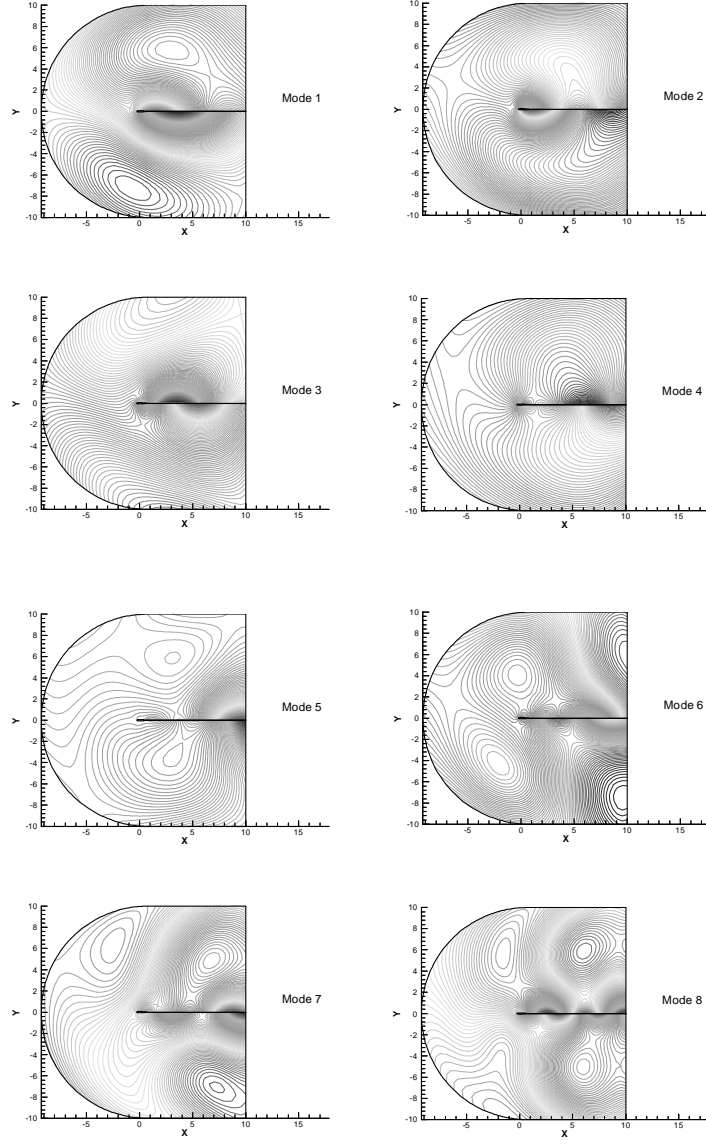


Figure 5.18 Blended POD/ROM Modes ($h_{\max} = 20\%$)

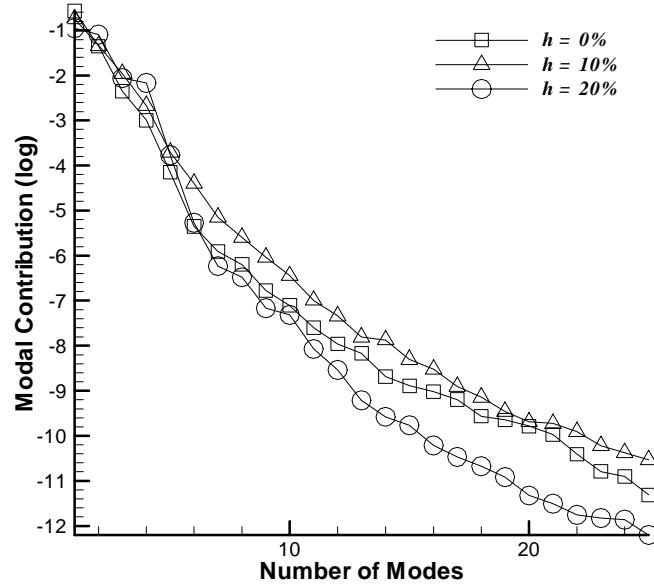


Figure 5.19 Blended POD/ROM Modal Contributions

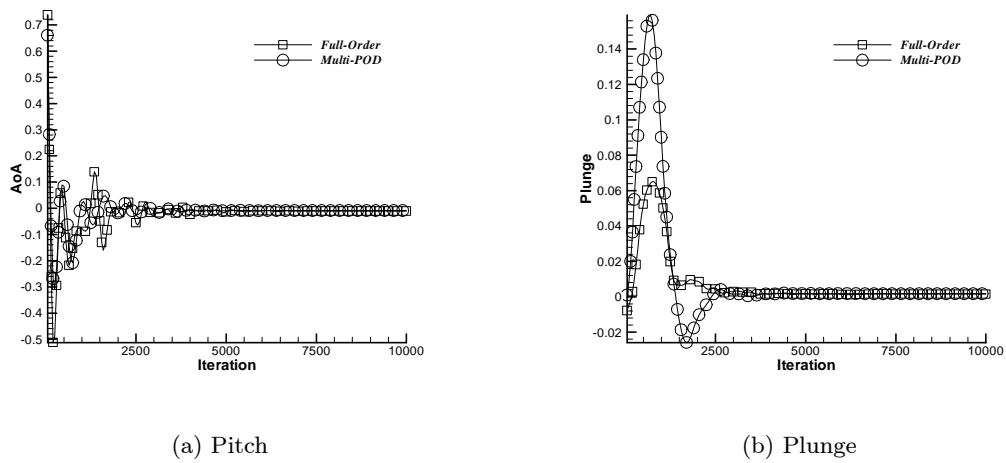


Figure 5.20 Multi-POD, Damped Case ($\bar{u} = 2.0$)

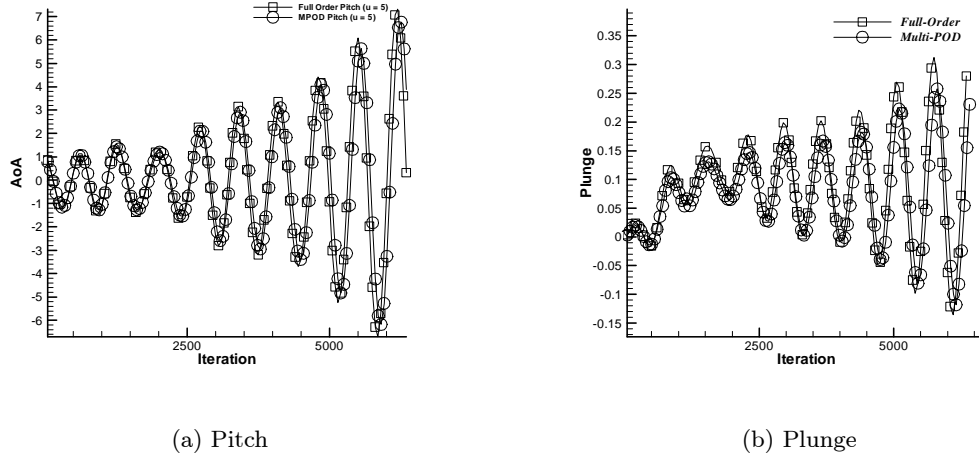


Figure 5.21 Multi-POD, Unstable Case ($\bar{u} = 5.0$)

Multi-POD varied between the two POD/ROMs until it finally switched to POD/ROM/20 as the solution became unstable. The solution was damped, but the non-linear behavior of the full system was accurately modeled (Fig 5.21). The changes between POD/ROMs were smooth and did not materially affect the solution. The Multi-POD accuracy was within 5% for pitch and 10% for plunge. To test how well a single POD/ROM would have performed, the same test was executed with the POD/ROM/B10 solely. The solution was heavily damped and did not match the full-order solution in a time accurate sense (see Fig 5.22 for variations). The errors were significant in pitch (over 100%), and could not capture the dynamics of the full-order solution.

5.3 Conclusions

POD/ROM was shown to be effective for problems with complex, coupled structural and fluid dynamics models. Errors in fluid variables were less than 6% of the full-order system for this model problem, and thus represent a reasonable level of accuracy for design. In the dynamic case of a pitching and plunging airfoil, POD/ROM was able to reproduce the full-order solution to within 6%. Individual POD/ROMs required only 20 modes for an accurate solution, producing a three order of magnitude reduction in dof (12250 to 20). Blended POD/ROM combined a variety of frequency and pitch angles into a single model

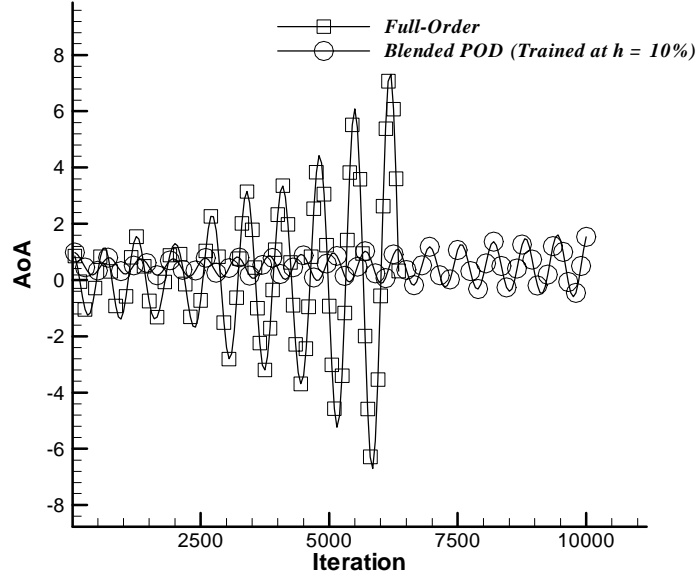


Figure 5.22 Blended POD (Trained at $h_{\max} = 10\%$), Unstable Case ($\bar{u} = 5.0$)

that accurately described a single set of grid deformations. Blended POD/ROMs required slightly more modes for accurate solutions in the higher dynamic cases.

The Multi-POD technique was shown to be effective for practical fluid dynamics problems by use of the model problem. The Multi-POD technique was able to reproduce the free deformation solution very accurately, based on POD/ROM that were developed from forced deformation cases. The Multi-POD was able to switch to the best available POD/ROMs for the deformation created by the loosely coupled structural model.

VI. Summary

The thesis of this dissertation, *POD/ROM can be used to simulate fluid flows accurately on deforming grids*, has been demonstrated through analysis and application to example problems. In POD/ROM, snapshots are taken of the unsteady flow-field data at intervals of time during a process called training. These snapshots are used to generate fluid modes. The modes are then used to create a reduced-order model. If the snapshots represent the fluid dynamics of the problem sufficiently well, the POD/ROM will be accurate. POD/ROM computations are conducted in computational (or index) space and do not directly account for grid deformation. The order of the data in the index space is irrelevant to the process, but must be consistent. At each snapshot in time, the grid is assumed to be identical to all other grids. In a problem with a deforming grid, the physical location of any data point changes from one snapshot to the next, even though its location in index space does not. Therefore, the set of grid point locations captured by the snapshots represent the range of grid deformation for which the problem was trained. In the simplest terms, variations in grids cause variations in modes created by POD/ROM. If two deforming grids are sufficiently different, the modes from one POD/ROM cannot be used with the other grid.

POD/ROM was shown to be sensitive to grid deformation. When compared to a rigidly attached grid for a nearly identical model problem, the deforming grid required more modes for an accurate solution. This shows conclusively that deforming grid POD/ROM differ from rigid grid POD/ROM due to the deformation. The additional modes necessary for accuracy for the POD/ROM/DG on a nearly identical problem were attributed to the relative motion of grid points due to the deformation. As the amount of deformation increased, in terms of the number of moving grid points, the number of modes necessary for an accurate solution increased.

POD/ROM accurately reproduced the flow field when applied to a deforming grid model problem when the run grid was identical to the training grid. The overall number of modes required for the deforming grid was still relatively small, reducing the order of the problem by three orders of magnitude. When the modes were applied at run grids that differed from the training grids, the POD/ROM accuracy degraded.

A technique was developed that evaluated the relative difference in training grids and run grids. The L_2 norm of the error in deformation correlated well with the resulting POD/ROM error. The metric was used in a real-time evaluation of the accuracy of the deforming grid POD/ROM, in a technique called Multi-POD. The Multi-POD technique determined the current relative grid deformation and selected the best POD/ROMs from those available. This resulted in a more robust algorithm that could be used over a variety of deformations and input parameters.

Finally, Multi-POD was applied to a problem where the grid deformation varied based on the fluid dynamics. In this case, separate POD/ROM were trained with forced grid deformation. The number of modes used in each POD/ROM was based on the complexity of the flow, with simpler flow fields requiring fewer modes. Then the model was run with free grid deformation. The Multi-POD technique was able to reproduce the free deformation solution very accurately, switching between POD/ROM as necessary. This demonstrated the robustness of the overall technique to a realistic model problem.

6.1 *Significant Advances*

Three significant advances were made in this work in answering the research questions proposed in the Introduction.

6.1.1 Static vs. Deforming Grid POD/ROM Analysis. In analyzing the amount of error associated with POD/ROM/DG, a technique was developed to compare various amounts of grid deformation by varying the number of deforming grid points. The sensitivity of POD/ROM accuracy to grid deformation is problem dependent. The degradation in accuracy due to grid deformation is based on the extent, relative magnitude, and scale of the deformation. By comparing the accuracy of the POD/ROM/DG created with varying numbers of deforming grid points for the same model problem and number of modes, a trend can be developed that shows the expected decrease in accuracy of the POD/ROM due to grid deformation.

6.1.2 Multi-POD. The Multi-POD approach is a unique technique that allows the best available POD/ROM to be used for a range of grid deformations, by switching between various POD/ROMs based on the deforming grid metric. A metric was developed to compare training and application grid deformation. This makes POD/ROM more robust over a wider range of grid deformation, and consequently over a wider set of applications. Without Multi-POD, POD/ROM/DG would be of limited utility.

6.1.3 Application to Aeroelastic Problem. A unique application was executed using POD/ROM/DG. POD/ROM/DGs were trained using a forced grid deformation and then applied to free grid deformation, where the grid dynamics were fully coupled with the fluid dynamics. The training of a POD/ROM/DG in a forced case is more practical, and allows the user to define a domain of solutions of interest. Then, in applying the POD/ROM/DGs to a free case, a wider range of problems of interest can be evaluated.

6.2 Future Work

There are three directions for proposed future work. First, implement the Domain Decomposition technique of Lucia, et. al. (43). In most practical problems, the deforming grid is restricted to a relatively small region around the body of interest. The domain decomposition technique allows the creation of a large POD/ROM for the deforming domain and smaller POD/ROM for the static grid domains further out from the body. The static grid domains would require fewer modes than the deforming grid domains, due both to the lack of deformation and the less significant fluid dynamics in the far field. Also, only the deforming domain would necessarily require a Multi-POD application. This would significantly save computation time.

Second, the full-order solver should be changed to a Navier-Stokes viscous solver. The full-potential solver is not robust enough to tackle complex model problems and the effect on POD/ROM modes due to viscosity in the deforming region should be explored. A new solver would also allow for an in-depth analysis of the computational savings that could be expected by using POD/ROM with deforming grid problems. The full-potential

solver uses a tri-diagonal matrix inversion that cannot be duplicated by POD/ROM and therefore any computational savings analysis is skewed in favor of the full-order solution.

Finally, the grid dynamics could be incorporated into the POD analysis. The x and y grid point calculations could be treated as fluid variables and incorporated into the implicit Jacobian matrix, allowing POD to be applied to them. In addition, the structural model could be incorporated in the Jacobian matrix, allowing for a fully coupled aeroelastic model. These two changes would allow the POD/ROM to be more robust to changes in the grid deformation, although not eliminating the need for Multi-POD.

Bibliography

1. Holmes, P., Lumley, J. L. and Berkooz, G. *Turbulence, Coherent Structures, Dynamical Systems and Symmetry*. Cambridge University Press, 1996.
2. Berkooz, G., Holmes, P. and Lumley, J. L. "The Proper Orthogonal Decomposition in the Analysis of Turbulent Flows," *Annual Reviews of Fluid Mechanics*, Vol. 25:539–575 1993.
3. Christensen, E. A., Brons, M. and Sorensen, J. N. "Evaluation of Proper Orthogonal Decomposition-Based Decomposition Techniques Applied to Parameter-Dependent Nonturbulent Flows," *SIAM Journal of Scientific Computing*, Vol. 21, No. 4:1419–1434 2000.
4. Beran, P. S., Huttshell, L. J., Buxton, B. J., Noll, C. and Osswald, G. "Computational Aeroelastic Techniques for Viscous Flow." *CEAS/AIAA/ICASE/NASA Langley International Forum on Aeroelasticity and Structural Dynamics*, Williamsburg, VA. June 1999.
5. Rediniotis, O. K., Ko, J., Yue, X. and Kurdila, A. J. "Synthetic Jets, Their Reduced Order Modeling and Applications to Flow Control." *AIAA 99-1000, 37th Aerospace Sciences Meeting and Exhibit*, Reno, NV. January 1999.
6. Kim, T. "Frequency-Domain Karhunen-Loeve Method and Its Application to Linear Dynamic Systems," *AIAA Journal*, Vol. 36, No. 11:2117–2123 November 1998.
7. Park, H. M. and Lee, M. W. "An Efficient Method of Solving the Navier-Stokes Equation for Flow Control," *International Journal for Numerical Methods in Engineering*, Vol. 41:1133–1151 1998.
8. Kim, T., Nam, C. and Kim, Y. "Reduced-Order Aerservoelastic Model with an Unsteady Aerodynamic Eigen Formulation," *AIAA Journal*, Vol. 35, No. 6:1087–1088 1997.
9. Park, H. M. and Cho, D. H. "The Use of the Karhunen-Loeve Decomposition for the Modeling of Distributed Parameter Systems," *Chemical Engineering Science*, Vol. 51, No. 1:81–89 1996.
10. Romanowski, M. C. and Dowell, E. H. "Aeroelastic Analysis of an Airfoil Using Eigenmode Based Reduced Order Unsteady Aerodynamics." *AIAA 95-1380-CP, 36th AIAA/ASME/ASCE/AHS/ASC Structures, Structural Dynamics, and Materials Conference*, New Orleans, LA. April 1995.
11. Hall, K. C. "Eigenanalysis of Unsteady Flows About Airfoils, Cascades, and Wings," *AIAA Journal*, Vol. 32, No. 12:2426–2432 December 1994.
12. Liu, Z. C., Adrian, R. J. and Hanratty, T. J. "Reynolds Number Similarity of Orthogonal Decomposition of the Outer Layer of Turbulent Wall Flow," *Physics of Fluids*, Vol. 6, No. 8:2815–2819 August 1994.
13. Loeve, M. *Functions Aleatoire de Second Ordre*. Paris, France: C. R. Academie des Sciences, 1945.

14. Karhunen, K. *Zur Spektral Theorie Stochastischer Prozesse*. Ann. Acad. Sci. Fennicae, Ser, 1946.
15. Lumley, J. L. "The Structure of Inhomogeneous Turbulence." *Proceedings of the International Colloquium on the Fine Scale Structure of the Atmosphere and its Influence on Radio Wave Propagation*. 166–178. Moscow: Dokl. Akad. Nauk SSSR, 1967.
16. Vigo, G. *The Extension of POD to Complex System with Non-Homogenous Boundary Conditions, Application to a Turbulent Pulsed Jet*. Technical Report N 3945, Institut National De Recherche en Informatique et en Automatique, May 2000.
17. Dowell, E. H. "Eigenmode Analysis in Unsteady Aerodynamics: Reduced Order Models." *AIAA 95-1450-CP, 36th AIAA/ASME/ASCE/AHS/ASC Structures, Structural Dynamics, and Materials Conference, New Orleans, LA*. April 1995.
18. Dowell, E. H. "Eigenmode Analysis in Unsteady Aerodynamics: Reduced-Order Analysis," *AIAA Journal*, Vol. 34, No. 8:1578–1583 August 1996.
19. Dowell, E. H., Hall, K. C. and Romanowski, M. C. "Eigenmode Analysis in Unsteady Aerodynamics: Reduced Order Models," *Applied Mechanical Review*, Vol. 50, No. 6:371–385 1997.
20. Mahajan, A. J., Bakhle, M. A. and Dowell, E. H. "A New Method for Aeroelastic Stability Analysis of Cascades Using Nonlinear, Time Marching CFD Solvers." *AIAA 94-4396, 5th AIAA/NASA/UASF/ISSMO Symposium on Multidisciplinary Analysis and Optimization, Panama City Beach, FL*. September 1994.
21. Romanowski, M. C. and Dowell, E. H. "Reduced Order Euler Equations for Unsteady Aerodynamic Flows: Numerical Techniques." *AIAA 96-0528, 34th Aerospace Sciences Meeting and Exhibit, Reno NV*. January 1996.
22. Florea, R. and Hall, K. C. "Eigenmode Analysis of Unsteady Flows About Airfoils," *Journal of Computational Physics*, Vol. 147:568–593 December 1998.
23. Florea, R., Hall, K. C. and Dowell, E. H. "Eigenmode Analysis and Reduced Order Modeling of Unsteady Transonic Full Potential Flow Around Isolated Airfoils." *CEAS/AIAA/ICASE/NASA Langley International Forum on Aeroelasticity and Structural Dynamics, Williamsburg, VA*. June 1999.
24. Thomas, J. P., Dowell, E. H. and Hall, K. C. "Three-Dimensional Transonic Aeroelastic Using Proper Orthogonal Decomposition." *AIAA 2001-1526, 42nd AIAA/ASCE/AHS/ASC Structures, Structural Dynamics and Materials Conference, Bellevue, WA*. April 2001.
25. Romanowski, M. C. "Reduced Order Unsteady Aerodynamic and Aeroelastic Models Using Karhunen-Loeve Eigenmodes." *AIAA 96-3981-CP, 6th AIAA/USAF/NASA/ISSMO Symposium on Multidisciplinary Analysis and Optimization, Bellevue WA*. September 1996.
26. Ly, H. V. and Tran, H. T. *Proper Orthogonal Decomposition for Flow Calculations and Optimal Control in a Horizontal CVD Reactor*. Technical Report, Center for Research in Scientific Computation, North Carolina State University, March 1998.

27. Iollo, A., Lanteri, S. and Desideri, J-A. *Stablity Properties of POD-Glaerkin Approximations for the Compressible Navier-Stokes Equations*. Technical Report N 3589, Institut National de Recherche en Informatique et en Automatique, December 1998.
28. Iollo, A. *Remarks on the Approximation of the Euler Equations by a Low Order Model*. Technical Report N 3329, Institut National de Recherche en Informatique et en Automatique, December 1997.
29. Beran, P. S. and Pettit, C. L. "Prediction of Nonlinear Panel Response Using Proper Orthogonal Decomposition." *42nd AIAA/ASCE/AHS/ASC Structures, Structural Dynamics and Materials Convergence, Bellvue, WA*. April 2001.
30. Mortara, S. A., Slater, J. C. and Beran, P. S. "An Optimal Proper Orthogonal Decomposition Technique for the Computation of Nonlinear Panel Flutter." *AIAA 2000-1936*. 2000.
31. Arian, E., Fahl, M. and Sachs, E. W. *Trust-Region Proper Orthogonal Decomposition for Flow Control*. Technical Report NASA CR-2000-210124, Institute for Computer Applications in Science and Engineering, NASA Langley Research Center, May 2000.
32. LeGresley, P. A. and Alonso, J. J. "Airfoil Design Optimization Using Reduced Order Models Based on Proper Orthogonal Decomposition." *AIAA 2000-2545, Fluids 2000 Conference and Exhibit, Denver, CO*. June 2000.
33. Shankar, V., Ide, H., Gorski, J. and Osher, S. "A Fast, Time-Accurate Unsteady Full Potential Scheme." *AIAA 84-1512, AIAA 18th Fluid Dynamics, Plasmadynamics, and Lasers Conference, Cincinnati OH*. July 1985.
34. Hall, K. C., Thomas, J. P. and Dowell, E. H. "Reduced-Order Modeling of Unsteady Small-Disturbance Flows Using a Frequency-Domain Proper Orthogonal Decomposition Technique." *AIAA 99-0655, 37th Aerospace Sciences Meeting and Exhibit, Reno, NV*. January 1999.
35. Beran, P. and Silva, W. "Reduced-Order Modeling: New Approaches for Computational Physics." *AIAA 2001-0853, 39th Aerospace Sciences Meeting and Exhibit, Reno, NV*. January 2001.
36. Tannehil, J. C., Anderson, D. A. and Pletcher, R. H. *Computational Fluid Mechanics and Heat Transfer, 2ed*. Washington DC: Hemisphere Publishing Company, 1997.
37. Willcox, K. and Peraire, J. "Balanced Model Reduction Via the Proper Orthogonal Decompostion." *AIAA 2001-2611, 15th AIAA Computational Fluid Dynamics Conference, Anaheim, CA.*. June 2001.
38. Atkinson, K .E. *An Introduction to Numerical Analysis, 2ed*. New York, NY: John Wiley and Sons, 1989.
39. Pettit, C. L. and Beran, P. S. "Reduced-Order Modeling for Flutter Prediction." *AIAA 2000-1446, 41st AIAA/ASCE/AHS/ASC Structures, Structural Dynamics and Materials Conference, Atlanta, GA*. April 2000.
40. Lindsey, W. F. and Daley, Benard N. *Effects of Compressiblity on the Flow Past a Two-Dimensional Bump*. Technical Report NACA TN 2484, NASA, 1952.

41. Sankar, L. N., Ruo, S. Y. and Malone, J. B. "Application of Surface Transpiration in Computational Aerodynamics." *AIAA 86-0511, AIAA 24th Aerospace Sciences Meeting, Reno, NV.* January 1986.
42. Morton, S. A. and Beran, P. S. "Hopf-Bifurcation Analysis of Airfoil Flutter at Transonic Speeds," *AIAA Journal of Aircraft, Vol. 36, No. 2:*421–429 1999.
43. Lucia, D., King, P., Beran, P. and Oxley, M. "Reduced Order Modeling for a One-Dimensional Nozzle Flow with Moving Shocks." *AIAA 2001-2602, 15th AIAA Computational Fluid Dynamics Conference, Anaheim, CA.* June 2001.
44. Bertin, J. J. and Smith, M. L. *Aerodynamics for Engineers.* New Jersey: Prentice-Hall Inc., 1989.
45. Newman, A. J. *Model Reduction Via the Karhunen-Loeve Expansion Part 1: An Exposition.* Technical Report T.R. 96-32, Institute for Systems Research, University of Maryland, 1996.
46. Newman, A. J. *Modeling and Reduction with Applications to Semiconductor Processing.* PhD dissertation, University of Maryland, Department of Electrical and Computer Engineering, 1999.
47. Sirovich, L. "Turbulence and the Dynamics of Coherent Structures. Part 1: Coherent Structures," *Quarterly of Applied Mathematics, Vol. 45, No. 3:*561–571 October 1987.
48. Landon, R. H. *Compendium of Unsteady Aerodynamics.* Technical Report AGARD-R-702, AGARD, 1972.
49. Strang, W. Z. *COBALT Users Manual.* Air Force Research Laboratory, Structures Division, 2000.
50. Kaplan, C. *The Flow of a Compressible Fluid Past a Curved Surface.* Technical Report NACA R-768, NASA, 1944.
51. Buxton, Bradley. *Comparison of Two Shock-Capturing Methods for Calculation of Transonic Airfoil Flutter.* MS thesis, Air Force Institute of Technology, 1995.

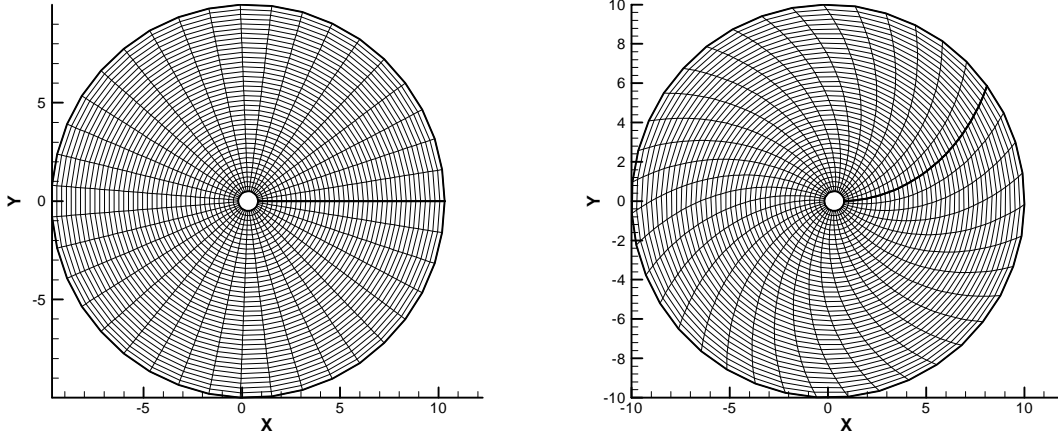
Appendix A. Potential Flow Around a Translating Cylinder

To determine the impact of grid deformation on POD/ROM, an attempt was made to isolate grid deformation effects from a numerical solution of fluid flow. A problem with an analytical solution was selected: potential flow around a cylinder. This allowed the fluid dynamics to be de-coupled from the grid dynamics. The nature and complexity of the grid modes could then be analyzed to see how they might affect the numerical solution. Two grid cases were selected. The first case was a rigid grid fixed to the cylinder and translating with it. This case included no deformation effects. The second case had a fixed outer boundary and the cylinder translated within the boundary, deforming the grid. For each grid case, POD/ROM was applied to snapshots of data obtained by imposing the analytical solution on the grids at selected increments in time. With the analytical solution, difference in the POD/ROM of the two cases could be solely attributed to the grid deformation.

A.1 Model Problem

Two grids were used in the model problem. In the first grid, the cylinder and grid rigidly translated together (Fig A.1). This eliminated any relative motion between the grid points. The cylinder oscillated through still fluid in the x direction and remained constant in the y direction. The center of the cylinder oscillated from $-5.0 \leq x \leq 5.0$ (non-dimensional units). This was done by varying the velocity of the center of the cylinder using a cosine function. Time was divided into 100 units ($0 \leq t \leq 100$). In this grid, at every time increment, each grid point had the same relative distance to the cylinder.

The second grid had an exterior boundary of fixed location, and the cylinder translated within it. The grid deformation was accomplished in three ways (Fig. A.2). First, a simple translation of the cylinder. Second, a rigidly translating grid and outer boundary that rotated. Third, a translating of the cylinder with a stationary in translation but rotating outer boundary. The three sub-cases of the deforming grid were intended to simulate the grid response of typical airfoil motions; plunging (translating), angle of attack (rotation), and combined pitching and plunging (translating/rotating). As in the first grid



(a) Rigidly Attached Grid

(b) Deforming Grid

Figure A.1 Grid Cases for Translating Cylinder

case, the cylinder was oscillated from $-5.0 \leq x \leq 5.0$ (non-dimensional units) by means of varying the velocity of the cylinder. When the outer boundary was rotated, the angle between the outer grid points and the corresponding cylinder points were evenly divided and the intervening grid points rotated incrementally. This resulted in a clocked grid. The cylinder was translated within the grid, causing deformation. This caused compression in the grid as well as rotation relative to the cylinder. The outer boundary is rotated from about $-30^\circ \leq \alpha \leq 30^\circ$,

$$\alpha(t) = b \cos(\theta t). \quad (\text{A.1})$$

Time was divided into 100 units ($0 \leq t \leq 100$). The cylinder, with radius $R = 1$, was translated in the x direction at varying velocity, $U(t)$, through a fluid otherwise at rest, which resulted in the perturbation stream function (44)

$$\Psi = U(t) R^2 \frac{y}{(x - x_0(t))^2 + y^2}, \quad (\text{A.2})$$

$$U(t) = a \sin(\theta t), \quad (\text{A.3})$$

where Ψ was the stream function and $x_0(t)$ the center of the cylinder at time t .

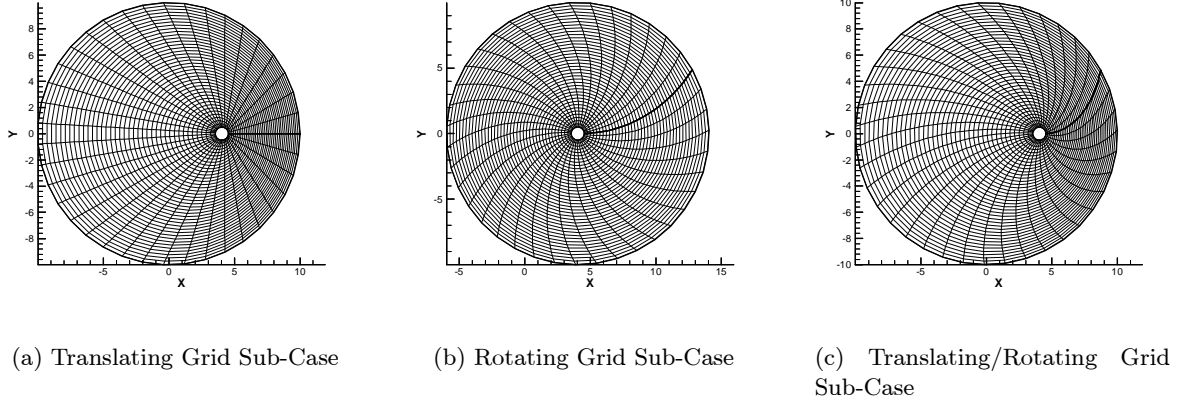


Figure A.2 Grid Sub-Cases for Deformation

To conduct an error analysis of POD/ROM with the deforming grid, snapshots were taken of the solution at various grid positions and cylinder velocities. This recorded data made up the snapshot matrix and was used to generate the modal matrix, Φ ,

$$\Psi \approx \Phi \hat{\Psi}. \quad (\text{A.4})$$

Next, a pseudo-inverse of Φ was needed to compute $\hat{\Psi}$ directly. This was accomplished using the Generalized Inverse (38), by multiplying both sides of Eqn. A.4 by the transformed matrix, Φ^T . This produced a square matrix, $\Phi^T \Phi$ on the RHS of Eqn. A.4. By assuming that the approximation of Ψ is exact, $\Phi^T \Phi$ was inverted and $\hat{\Psi}$ determined. Finally, the error of the POD/ROM was determined by substituting $\hat{\Psi}$ into the original approximation for Ψ :

$$error_{\Psi} = \Psi - \Phi \hat{\Psi}, \quad (\text{A.5})$$

$$error_{\Psi} = \Psi - \Phi (\Phi^T \Phi)^{-1} \Phi^T \Psi. \quad (\text{A.6})$$

The error resulted solely from the loss of information that occurred as the POD/ROM reduced the analytical solution to a smaller subspace. If Φ were square and nonsingular (the number of modes equaling the number of grid points), the error in equation (A.5) would vanish and the POD/ROM would be exact.

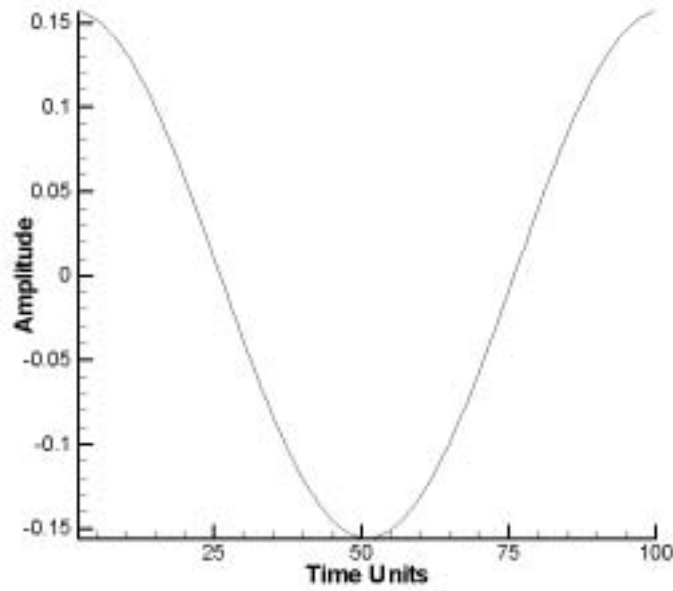
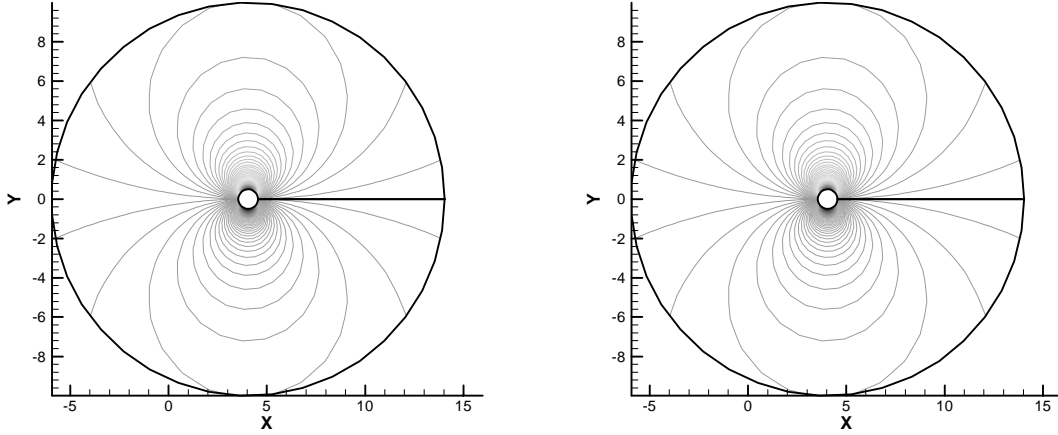


Figure A.3 POD/ROM/RG vs. Analytical Solution (Maximum value of Ψ , lines are identical)

A.2 Results

The POD/ROMs of the two grids were significantly different. The rigid grid case POD/ROM, POD/ROM/RG, was an exact solution and required only a single mode. The deforming grid POD/ROM, POD/ROM/DG, was not an exact solution and required modes for accuracy. The additional modes of the deforming grid were attributed solely to the deforming grid and considered grid modes (modes that represent the deformation of the grid and the subsequent mapping of the undeformed solution to the deformed space).

A.2.1 Rigid Grid Case. The first mode of the POD/ROM/RG contained 100% of the total energy of the eigenvalues. The remaining modes were machine zero (10^{-14}). By plotting the contribution to the maximum value of the stream function for each mode, the relative contribution of each mode could be examined. The first mode and the true solution were identical lines (Fig. A.3). The single mode, when plotted against the rigid grid, was a scalar fraction of the true solution. As the cylinder accelerated, the reduced order variable scaled the mode to match the true solution. When the cylinder came to



(a) Analytical Solution

(b) POD/ROM with 1 mode

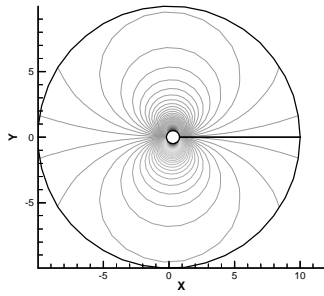
Figure A.4 POD/ROM/RG Contours of Ψ

rest, the reduced order variable scaled to zero. The POD/ROM/RG with one mode was exact (Fig. A.4). The eigenmode could be captured at any time increment with a single snapshot.

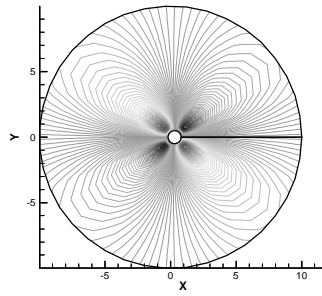
A.2.2 Deforming Grid Case. The three deforming grid sub-sub-cases were compared to determine if the type of deformation affected the accuracy of POD/ROM.

Translating Sub-Case: In the translating sub-case, the cylinder was translated within the outer boundary to create compression and stretching of the cells. The primary mode of the translating sub-case was a scalar fraction of the analytical solution and accounted for 98% of the total eigenvalue energy. The other modes were radial in nature, due to the grid deformation maintaining straight radial grid lines (Fig. A.5). The remaining modes decreased in energy rapidly and were negligible by the 7th mode (10^{-7}) (Fig. A.6). In the translating sub-case, POD/ROM only required four modes for a 99% accurate solution. Using fewer modes resulted in a slightly compressed solution (Fig. A.7).

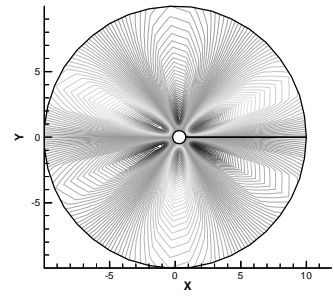
Rotating Sub-Case: In the rotating sub-case, the outer boundary was rotated with respect to the cylinder, creating skewness in the grid cells. As in the translating



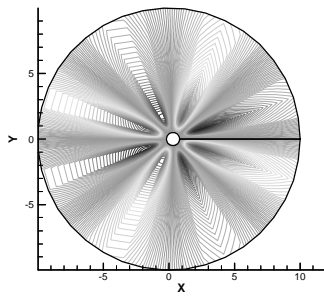
(a) Mode 1



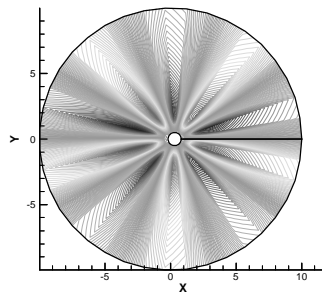
(b) Mode 2



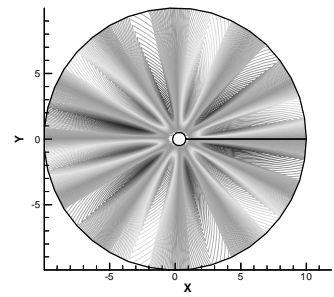
(c) Mode 3



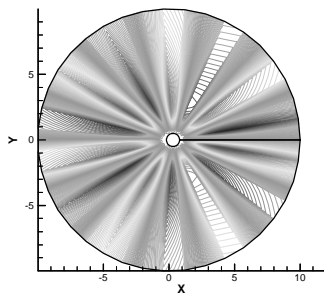
(d) Mode 4



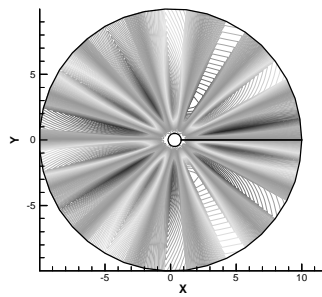
(e) Mode 5



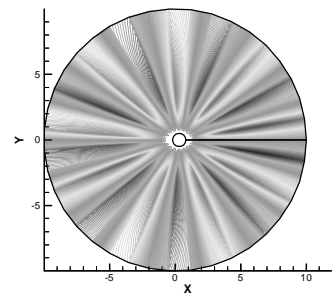
(f) Mode 6



(g) Mode 7



(h) Mode 8



(i) Mode 9

Figure A.5 Translating Grid Sub-Case POD/ROM/DG Modes

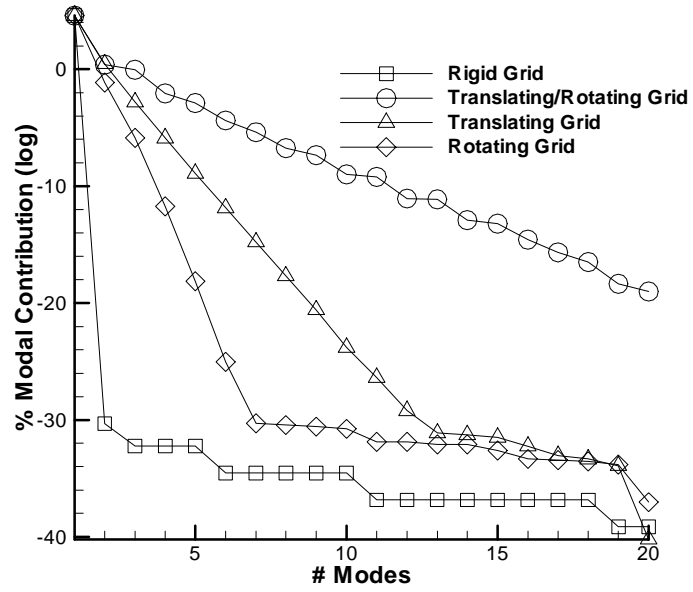
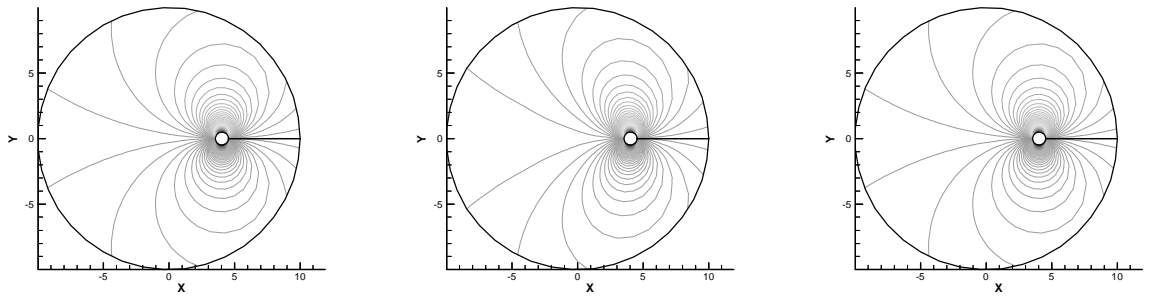


Figure A.6 POD/ROM Modal Contribution (Rigid and Deforming Grid Cases)



(a) Analytical Solution

(b) POD/ROM With 2 modes

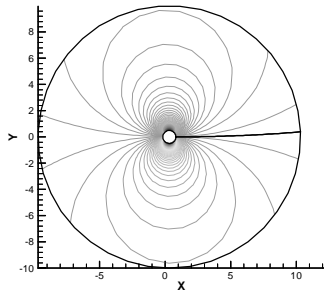
(c) POD/ROM With 4 modes

Figure A.7 Translating Grid Sub-Case POD/ROM/DG Contours of Ψ

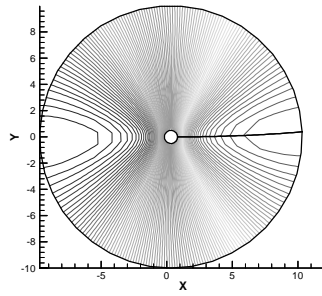
sub-case, the primary mode was a scalar fraction of the analytical solution and accounted for 99.7% of the total eigenvalue energy. The other modes were annular in nature, due to the annular sweep of the grid points as they rotated about the cylinder (Fig. A.8). The remaining modes decreased in energy even more quickly than the translating sub-case and was negligible by the 5th mode (10^{-8}) (Fig. A.6). In the rotating sub-case, POD/ROM required only three modes for a 99% accurate solution. Using only two modes resulted in a small deviation in the areas of highest grid movement (the boundaries) (Fig. A.9).

Translating/Rotating Sub-Case: In the translating/rotating sub-case, the grid was deformed by both translation within the outer boundary, as well as rotation of the outer boundary with respect to the cylinder. The translating/rotating sub-case was the most complex and required the most modes for an accurate solution. The first mode of the deforming grid POD/ROM had 98.7% of the total energy of the eigenvalues. The remaining modes decreased in energy quickly, but were still significant compared to those of the rigid grid POD/ROM (Fig. A.6). The first mode of the translating/rotating sub-case was similar to the rigidly translating case: a scalar fraction of the true solution. The remaining modes for the deforming grid POD/ROM were variations to account for the changes in the physical locations of the grid points (Fig. A.10). Mapping the modes to an undeformed grid, the higher modes appear as corrections from the undeformed grid to the deformed grid. The translating/rotating sub-case POD/ROM required at least 7 modes for a 99% accurate solution. Using fewer modes resulted in a skewed solution (Fig. A.11) where the principle mode is incorrectly mapped to the deformed grid. Using more modes resulted in a more accurate solution.

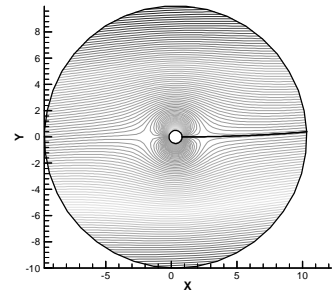
If the POD/ROMs were run on a grid that differed from the training grid, the accuracy diminished. Two cases were tried, that of a synchronous clocking of translation and rotation, and that of an asynchronous clocking. If the boundary was started at zero degrees, the rotation was synchronous with the translation of the cylinder. Thus, the solution started at the undeformed/unrotated state and returned to that state at least twice more. However, when the solution started at the maximum rotation, the rotation was not synchronized with the cylinder movement and the solution never approached the



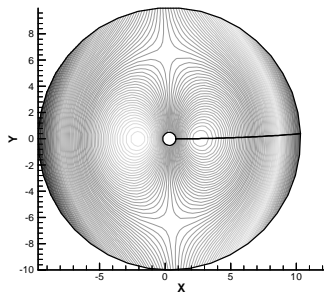
(a) Mode 1



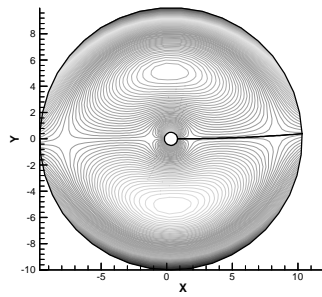
(b) Mode 2



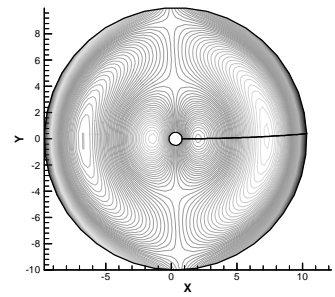
(c) Mode 3



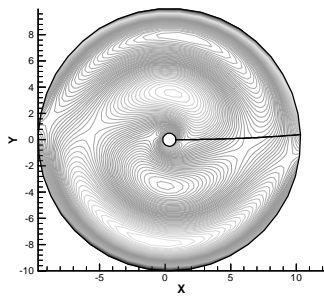
(d) Mode 4



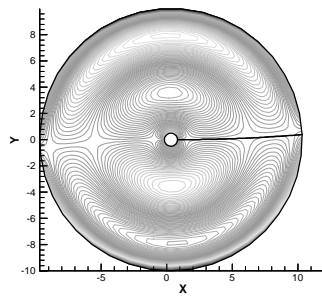
(e) Mode 5



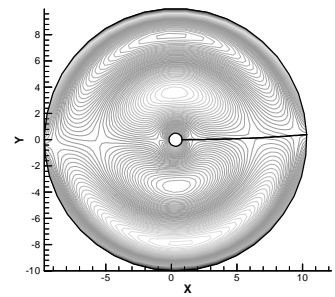
(f) Mode 6



(g) Mode 7



(h) Mode 8



(i) Mode 9

Figure A.8 Rotating Sub-Case POD/ROM/DG Modes

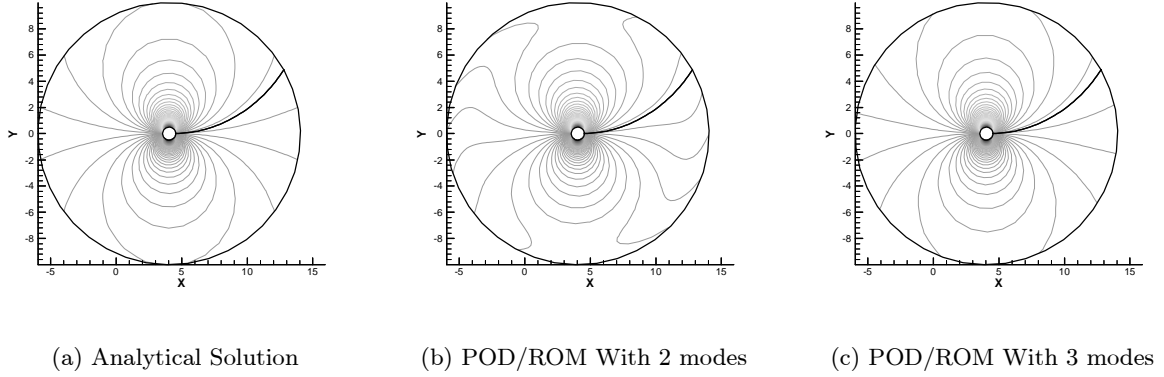


Figure A.9 Rotating Grid Sub-Case POD/ROM/DG Contours of Ψ

undeformed/unrotated state within the time interval considered. In both cases, the grid never underwent the exact position of the training grids.

In the synchronous sub-case, 11 snapshots (and hence 11 modes) could be used before the POD would become unstable due to linear dependence. The 10 grid modes of the system were very small compared to the initial fluid mode and had eigenvalues that were only 3% of the eigenvalue sum. By plotting the contribution of each mode to the maximum value of stream function, the relative magnitudes of the modes can be isolated (Fig. A.12).

In the asynchronous sub-case, 20 snapshots could be taken while maintaining linear independence. The additional number of snapshots (and therefore modes) was due to the more complex interaction between the asynchronous movement of the translation and rotation. The 19 grid modes of the system were very small in magnitude compared to the initial fluid mode, and had eigenvalues totaling only 5% of the eigenvalue sum (Fig. A.13).

In both sub-cases, the greater the number of modes included, the more accurate the solution was (Tbl. A.1). Even with the largest number of modes possible, the maximum error throughout the 100 time units was almost 10%. This error occurred approximately at midpoint in time between two snapshots, during the most rotated and deformed po-

Table A.1 Maximum Percentage Error of Stream Function

Synchronous sub-case		Asynchronous sub-case	
# Modes	% Max Error	# Modes	% Max Error
6	3380.50	14	307.07
8	94.95	16	108.30
10	17.04	18	44.60
11	7.05	20	13.02

Table A.2 Effect on Error due to Mode Truncation

Synchronous sub-case		Asynchronous sub-case	
# Modes	% Max Error	# Modes	% Max Error
6 of 11	1252.14	14 of 20	300.73
8 of 11	240.56	16 of 20	124.84
10 of 11	21.56	18 of 20	63.76
11 of 11	7.05	20 of 20	13.02

sition. The average error over the entire grid of the stream function at this point was approximately 1.0%.

Taking fewer than the maximum allowable number of modes (based on the limitation of the current computational method) resulted in a less accurate solution (Tbl. A.2). Mode truncation at the 99.9% level resulted in errors in excess of 1000%.

A.2.3 Grid Density. Grid density was also examined. Solutions were calculated using the maximum number of modes for each sub-case using grid densities of $I, J = 10 \times 10, 20 \times 20, 30 \times 30$, and 40×40 (Tbl. A.3). As grid density increased, accuracy decreased. This was due to the deformation of each individual grid point being more severe. Each point had to move further relative to its original position in the more dense cases, in terms of index position.

Table A.3 Effect on Error due to Grid Density

	Synchronous sub-case	Asynchronous sub-case
$I \times J$	% Max Error (11 modes)	% Max Error (20 modes)
10×10	0.19	0.32
20×20	0.60	3.07
30×30	7.04	13.02
40×40	22.47	24.47

A.3 Conclusions

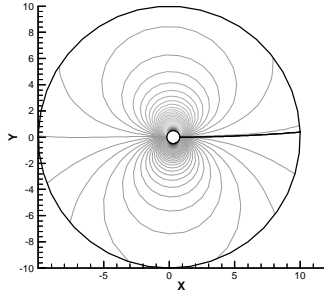
Overall, the use of POD/ROM with a deforming grid was reasonable. An algorithm must be created to ensure that accuracy is maintained, but the basic application of POD/ROM was sound. Of the above issues, the increase in the number of overall modes by the addition of distinct grid modes presents the main research area. As the number of modes increase, the solution time increases, decreasing the effectiveness of using POD/ROM. The additional grid modes cannot be truncated without significantly decreasing accuracy. The sample problem de-coupled fluid dynamics from grid dynamics. In the case of the rigid grid, the POD/ROM was able to return an exact solution with only one mode. In the case of the deforming grid, the POD/ROM was able to reproduce an accurate solution, but required more modes to do so. In all cases, the primary mode was similar regardless of whether or not there was deformation or not. This mode represented the fluid dynamics that was de-coupled from the grid dynamics. For the deforming grid cases, the remaining modes corrected the first mode to the deformed state of the grid.

The magnitudes of the eigenvalues showed that POD/ROM was more sensitive to translation than rotation in this model problem. This was due to the greater scope of movement for all of the grid points in the translating case. The lower energy modes of translation and rotation were also significantly different. The grid modes tended to align themselves along the path of the grid motion.

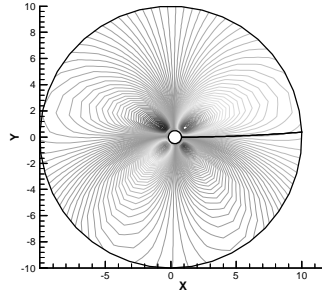
When translation and rotation were combined, the problem became even more complex and required more modes to solve accurately. The lower energy grid modes of the translating/rotating sub-case were not simple additions of the grid modes from the separate translating and rotation sub-cases.

The grid density for any viscous problem will be an issue if a deforming grid is implemented. The grid density necessary for a viscous boundary layer is very large and any deformation will result in a large number of grid modes. As the number of modes necessary for an accurate solution increases with grid density, some method of minimizing the area of grid deformation will be necessary. One approach would be to limit the grid

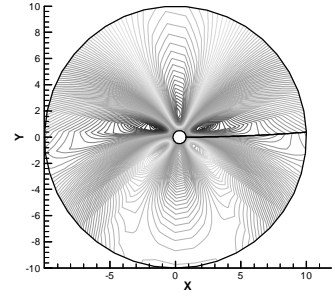
deformation to a percentage change in relative position. If a grid point's location does not change much in a single time increment, it could be kept static.



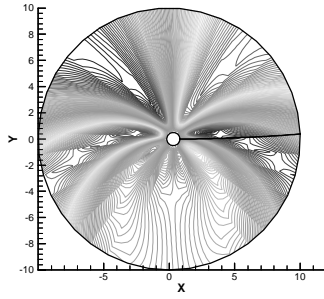
(a) Mode 1



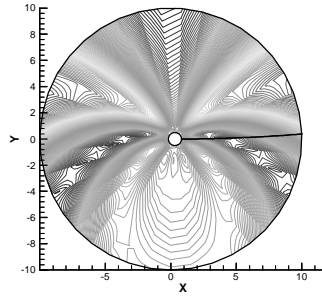
(b) Mode 2



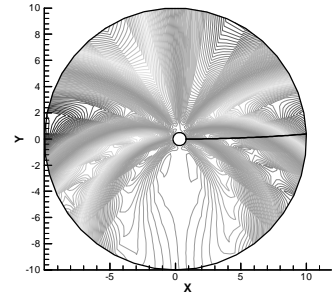
(c) Mode 3



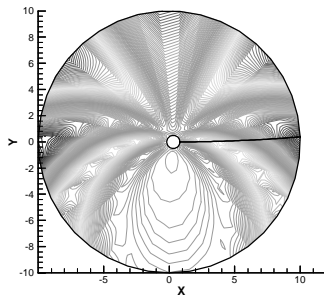
(d) Mode 4



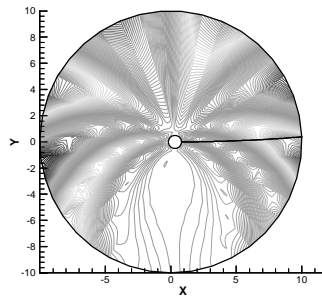
(e) Mode 5



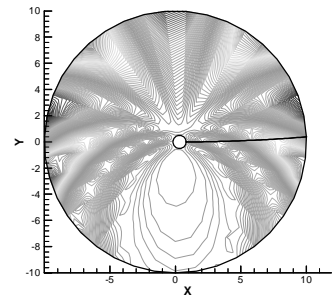
(f) Mode 6



(g) Mode 7



(h) Mode 8



(i) Mode 9

Figure A.10 Translating/Rotating Sub-Case POD/ROM/DG Modes

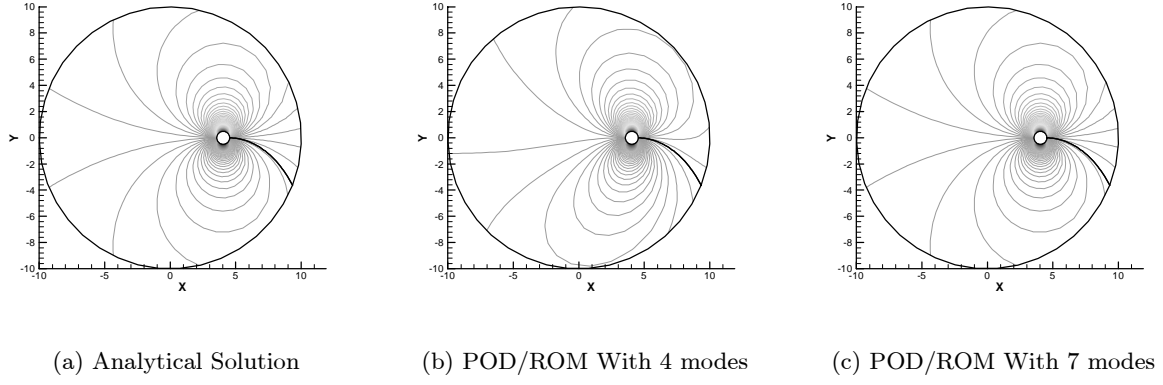


Figure A.11 Translating/Rotating Grid Sub-Case POD/ROM/DG Contours of Ψ

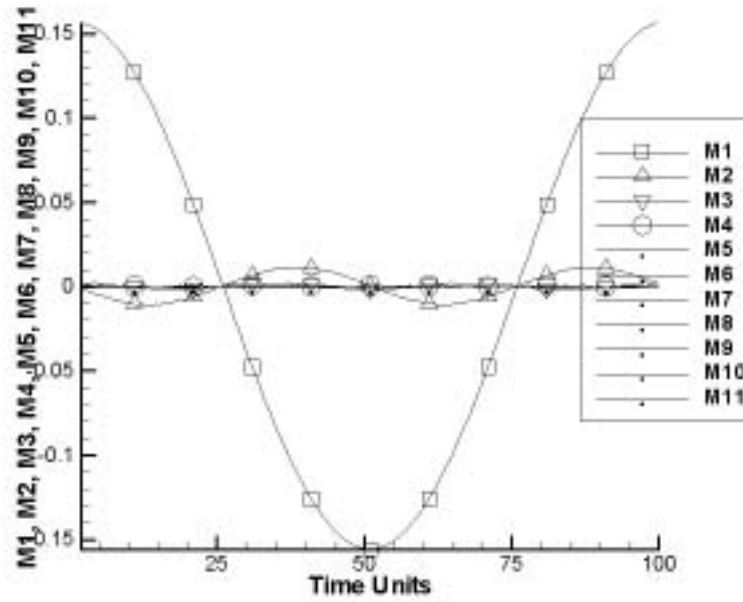


Figure A.12 Max value of Stream Function by mode

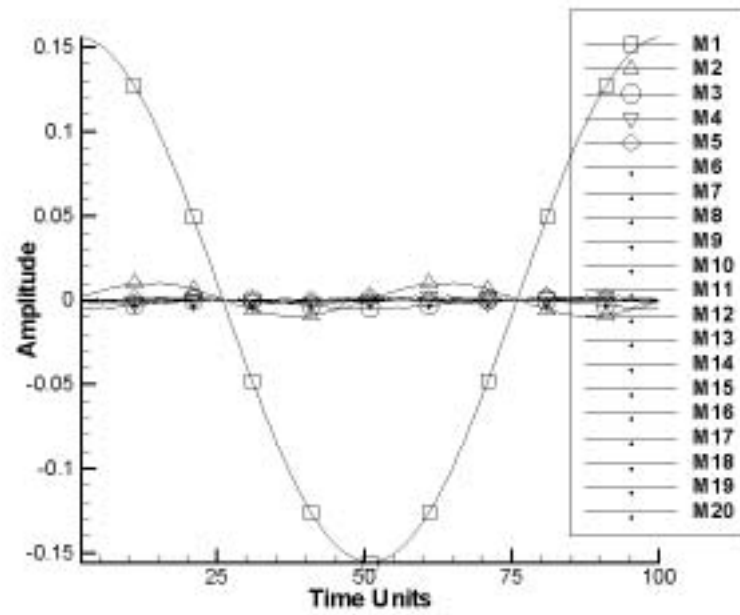


Figure A.13 Max value of Stream Function by mode

Appendix B. Proper Orthogonal Decomposition Theory

Also known as Karhunen-Loève decomposition, principal components analysis, singular systems analysis, and singular value decomposition (1), Proper Orthogonal Decomposition (POD) generates a basis for the modal decomposition of functions and discrete data, such as experimental data. POD is one member of the class of representations known as orthogonal expansions (the Fourier series, or harmonic decomposition, is another example). The POD basis is linearly optimal in that it provides the most efficient way of capturing the dominant components of an infinite-dimensional process of finite dimension modes. The basis functions it yields are called empirical eigenfunctions, empirical basis functions and empirical orthogonal functions (1).

The derivation of POD is recreated in a variety of works (see (1), (45), (14), (13)). However, the most complete derivation in the literature is presented in the dissertation of Newman (46), and it is from this source that the following is section is taken.

B.1 Derivation

A stochastic process is a family (ensemble) of random variables or functions from some measurable space, from which a probability space can project into a state space. Suppose that $\{X^k\}$ is an ensemble of a stationary (no time varying mean values) stochastic process, defined on a spatial domain D . To obtain an accurate representation of the members of $\{X\}$, each is projected onto a set of candidate basis functions. Assume that X belongs to an inner product space (the linear, infinite-dimensional Hilbert space, $\mathcal{L}_2(D)$, of square integrable (complex-valued) functions), the orthogonal representation of $\{X^k\}$

$$X(t, x) = \sum_n^{\infty} a_n(t) \phi_n(x), \quad (\text{B.1})$$

where $\{\phi_n\}$ is the orthonormal basis and $\{a_n\}$ the uncorrelated set of random variables, in time. A reduced-order model (ROM) can be obtained by truncating the series equation (B.1) to N terms.

The assumptions of the inner product space affect how POD is developed. A Hilbert space \mathcal{H} is a vector space over \mathbb{R} or \mathbb{C} together with an inner product $\langle \cdot, \cdot \rangle$ which is complete as a metric space. The norm is defined as $\|\phi\| = \sqrt{\langle \phi, \phi \rangle}$ for $\phi \in \mathcal{H}$ and the metric is defined as $d(\phi, \psi) = \|\phi - \psi\|$ for $\phi, \psi \in \mathcal{H}$. A set of vectors \oplus in a Hilbert space \mathcal{H} is an orthonormal set if any two distinct vectors $\phi_1, \phi_2 \in \oplus$ are orthogonal, i.e., $\langle \phi, \phi \rangle = 0$, and in addition, $\|\phi\| = 1$ for each $\phi \in \oplus$. The $\mathcal{L}_2[a, b]$ space is that of complex-valued (or real-valued) Lebesgue-measurable, square integrable functions on a domain D , and is generally an infinite-dimensional Hilbert space with an inner product on $\mathcal{L}_2(D)$ of

$$\langle f, g \rangle_{\mathcal{L}_2(D)} = \int f(x) g(x) dx. \quad (\text{B.2})$$

Newman provides a detailed derivation of the Hilbert space, \mathcal{H} , and its properties as they relate to POD. The development of POD requires an orthonormal set of basis functions, $\{\phi\}$, for the $\mathcal{L}_2(D)$ subspace. Because it is a Hilbert space, there are an infinite number of orthonormal basis sets. However, Sirovich (47) provides a method of selecting a particular choice.

Theorem 1 *Sirovich: If $\{\phi\}$ is a complete orthonormal set of functions in $\mathcal{L}_2(D)$ such that the expansion can be written as equation (B.1) where both of the sets $\{a_n\}$ and $\{\phi_n\}$ are orthonormal, i.e.,*

$$\langle a_k, a_l \rangle_{\mathcal{L}_2(D)} = E[a_k(t) a_l(t)] = \delta_{lk}, \quad (\text{B.3})$$

and

$$\langle \phi_k, \phi_l \rangle_{\mathcal{L}_2(D)} = \int_D \phi_k(x) \phi_l(x) dx = \delta_{lk}, \quad (\text{B.4})$$

with $E[\cdot]$ as a probabilistic averaging operation (1), then $\{\phi_n\}$ are found in a spectral decomposition of the two-point spatial correlation function

$$R(x, y) = \sum_n \phi_n(x) \phi_n(y). \quad (\text{B.5})$$

This then provides an attractive candidate for the orthonormal basis to use in the expansion, and the goal becomes to determine if such a basis exists. The existence of the

expansion, equation (B.1), that satisfies the above conditions is guaranteed under certain conditions by the Karhunen-Loève expansion theorem (presented below). Moreover, the Karhunen-Loève expansion theorem proves a method for constructing the orthonormal set of basis functions. The proof depends on the existence of the spectral decomposition of the spatial correlation function, which is guaranteed under certain conditions by Mercer's theorem.

Theorem 2 *Mercer: Let $k(\cdot, \cdot)$ be a continuous, Hermitian symmetric, nonnegative definite function on $[a, b] \times [a, b]$. If $\{\phi_n\}$ and $\{\lambda_n\}$ are a basic system of eigenvectors and eigenvalues of the integral operator with kernel $k(\cdot, \cdot)$ then $\forall_{s,t} \in [a, b]$,*

$$k(s, t) = \sum_{n=1}^{\infty} \lambda_n \phi_n(t) \phi_n(s). \quad (\text{B.6})$$

The series converges absolutely and uniformly on $[a, b] \times [a, b]$.

With the Mercer theorem, the Karhunen-Loève theorem defines the continuum of random variables by a countable number of orthonormal random variables.

Theorem 3 *Karhunen-Loève Expansion: Let $\{X_t, t \in [a, b]\}$ be a zero-mean, quadratic-mean continuous second-order stochastic process with covariance function $R(t, s)$. The process X_t has an orthogonal decomposition*

$$X(\omega, t) = \lim_{N \rightarrow \infty} \sum_{i=1}^N \sqrt{\lambda_i} a_i(\omega) \phi_i(t) \quad t \in [a, b], \quad (\text{B.7})$$

with an associated averaging operation

$$E[a_i, a_j] = \delta_{ij}, \quad (\text{B.8})$$

and

$$\langle \phi_i, \phi_j \rangle_{\mathcal{L}_2[a, b]} = \int_a^b \phi_i(t) \phi_j(t) dt = \delta_{ij}, \quad (\text{B.9})$$

if and only if the $\{\phi_1, \phi_2, \dots\}$ are the orthonormal eigenfunctions and the $\{\lambda_1, \lambda_2, \dots\}$ are the corresponding eigenvalues of the integral operator with the kernel $R(\cdot, \cdot)$ i.e.,

$$\int_a^b R(t, s) \phi_i(s) ds = \lambda_i \phi_i(t) \quad t \in [a, b] \quad i = 1, 2, \dots \quad (\text{B.10})$$

In that case, the series converges uniformly on $[a, b]$.

The coefficient functions $\{\phi_n\}$ that correspond to the non-zero eigenvalues $\{\lambda_n\}$ are called the empirical eigenfunctions. They form an orthonormal basis for the subspace $\mathcal{L}_2(D)$. The uncorrelated random variables $\{a_n\}$ are given by

$$a_n(\omega) = \left(\sqrt{\{\lambda_n\}} \right)^{-1} \int_a^b \phi_n(t) X(\omega, t) dt, \quad (\text{B.11})$$

and form the desired orthonormal basis for \mathcal{H} .

To summarize the theorems, if there is a stochastic ensemble and if it can be expressed as equation (B.1), then a ROM can be created by truncating the orthonormal basis vectors $\{\phi_n\}$. If the space is a Hilbert space and the inner product is defined as equation (B.2), then there are infinite orthogonal basis sets. Sirovich's Theorem says that one of those basis sets can be defined using a probabilistic averaging function and the spatial correlation function (kernel). Mercer's theorem defines a kernel and Karhunen-Loève expansion finally defines the orthonormal basis in terms of the original stochastic ensemble and the kernel.

B.2 Discretized Sample Spaces

In discrete applications, the ensemble is sampled in time, space, or both. The discretized Karhunen-Loève expansion relies on the spectral theorem for real symmetric matrices which is the finite-dimension analogue to Mercer's theorem. If the set, $X_i(\omega), i \in [a, b]$, is a zero-mean scalar-valued, discrete-parameter, second-order process with covariance matrix R , then the matrix R can be expressed as $R(j, k) = E[X_j X_k^T]$. The matrix R is real, symmetric, and non-negative definite. The spectral theorem states that every matrix R can be diagonalized by an orthogonal matrix. That is, there exists an orthogonal matrix Φ and a real diagonal matrix Λ such that $R = \Phi \Lambda \Phi^T$. The spectral decomposition of R

can be expressed as

$$R = \sum_{n=1}^{\infty} \lambda_n \phi_n \phi_n^T, \quad (\text{B.12})$$

where each vector ϕ_n is the n -th column of Φ .

Theorem 4 *Sampled Data Karhunen-Loève Expansion: Let $\{X_i(\omega), i \in [a, b]\}$ be a zero-mean scalar-valued discrete-parameter, second-order process with covariance matrix R . The process X_i has an orthogonal decomposition given by*

$$X(\omega, i) = \lim_{N \rightarrow \infty} \sum_{n=1}^N \sqrt{\lambda_n} a_n(\omega) (\phi_n)_i \quad k = 0, 1, \dots \quad (\text{B.13})$$

with

$$E[a_i a_j] = \delta_{ij}, \quad (\text{B.14})$$

and

$$\langle \phi_i, \phi_j \rangle = \phi_i^T \phi_j = \delta_{ij}, \quad (\text{B.15})$$

if and only if $\{\phi_n\}$ are the orthonormal eigenvectors and $\{\lambda_n\}$ are the corresponding eigenvalues of the matrix R :

$$R\phi_n = \lambda_n \phi_n. \quad (\text{B.16})$$

B.3 Optimality

The optimization of POD can be expressed as a minimization of error or, equivalently, as the maximization of the projection of any member of the stochastic ensemble onto the subspaces spanned by the most energetic members of the empirical basis. Consider the ensemble $\{X(\omega, \cdot) : [a, b] \rightarrow \mathbb{R}^n, \omega \in \Omega\}$ and let $\{\phi_n\}$ be the empirical eigenfunctions with corresponding eigenvalues, $\{\lambda_n\}$. Let $\{X(\bar{\omega}, t), \bar{\omega} \in \Omega, t \in [a, b]\}$ be a member of the ensemble with POD

$$X(\bar{\omega}, t) = \sum_{n=1}^N b_n(\bar{\omega}) \phi_n(t), \quad (\text{B.17})$$

where $b_n(\omega) = \sqrt{\lambda_n} a_n(\omega)$. Let $\{\psi_n\}$ be an arbitrary orthonormal set such that for some random variables $\{c_n\}$

$$X(\bar{\omega}, t) = \sum_{n=1}^N c_n(\bar{\omega}) \psi_n(t). \quad (\text{B.18})$$

Then, for each truncation index N

$$\sum_{n=1}^N E[|\langle \phi_n, X_t \rangle|] = \sum_{n=1}^N \lambda_n \geq \sum_{n=1}^N E[|\langle \psi_n, X_t \rangle|], \quad (\text{B.19})$$

and equivalently

$$\sum_{n=1}^N E[\|b_n\|^2] = \sum_{n=1}^N \lambda_n \geq \sum_{n=1}^N E[\|c_n\|^2]. \quad (\text{B.20})$$

To examine the minimization of error, on average, between the members of the ensemble and the truncated orthogonal expansion, observe that the minimum of the mean-square error

$$E \left[\left\| X_t - \sum_{n=1}^{\infty} c_n(\bar{\omega}) \psi_n(t) \right\|^2 \right] = E[\|X_t\|^2] + \sum_{n=1}^N E[\|c_n(\bar{\omega}) \psi_n(t)\|^2] - 2 \sum_{n=1}^N E[\langle c_n(\bar{\omega}) \psi_n(t) \rangle], \quad (\text{B.21})$$

is achieved when $\sum_{n=1}^N E[\langle c_n(\bar{\omega}) \psi_n(t) \rangle]$ is maximized.

B.4 Method of Snapshots

From a practical point of view, data is sampled at discrete values of time. The calculation of the spatial covariance matrix $R = E[X_t X_t^T]$ must use discrete samples or snapshots of data. These sets of snapshots form a snapshot matrix, S , where the sampled ensemble data, $\{X(t_1), X(t_2), \dots\}$, is placed into columns. If the process is assumed to be ergodic or stationary (time average equals ensemble average for each fixed value of X) then the averaging function can be expressed as

$$R = E[X_t X_t^T] = \lim_{T \rightarrow \infty} \frac{1}{M} \int_0^T X_t X_t^T dt. \quad (\text{B.22})$$

R can be further approximated as

$$R \approx \hat{R} = \lim_{M \rightarrow \infty} \frac{1}{M} \sum_{n=1}^M X(t_n) X(t_n)^T. \quad (\text{B.23})$$

Since there are only a finite number of M snapshots available, the approximation, \hat{R} , is further reduced to

$$\hat{R} \approx \hat{R}_M = \frac{1}{M} \sum_{n=1}^M X(t_n) X(t_n)^T. \quad (\text{B.24})$$

\hat{R}_M can be expressed in matrix form as

$$\hat{R}_M = \frac{1}{M} S S^T, \quad (\text{B.25})$$

where S is an $N \times M$ matrix containing M snapshots of $X(t)$, with the data stored as column vectors in the matrix. It is common for authors to ignore the $\frac{1}{M}$ factor and absorb it into the generation of the eigenvalues in the solution of the eigen-problem of equation (B.16), $\hat{R}_M \phi_n = \lambda_n \phi_n$. This particular problem can be solved by Singular Value Decomposition, yet it requires the calculation of the $N \times N$ matrix \hat{R}_M to be explicitly carried out.

In fact, the Method of Snapshots does not use the spatial covariance matrix, \hat{R}_M , but instead a temporal covariance matrix, \hat{C}_M . Assume that the snapshots are linearly independent vectors, i.e., the data matrix S has full column rank, and define the temporal covariance $M \times M$ matrix

$$\hat{C}_M = \frac{1}{M} S^T S. \quad (\text{B.26})$$

Starting with a similar eigen-problem as equation (B.16), and

$$\hat{C}_M \psi_n = \mu_n \psi_n,$$

and using the definition of \hat{C}_M and eigenvectors and values of $\{\psi_n\}$ and $\{\mu_n\}$,

$$\mu_n \psi_n = \frac{1}{M} S^T S \psi_n \quad i \in M, \quad (\text{B.27})$$

$$S\mu_n\psi_n = S\frac{1}{M}S^TS\psi_n, \quad (\text{B.28})$$

The eigen-problems are equivalent if and only if

$$\phi_n = S\psi_n \quad i \in M. \quad (\text{B.29})$$

Resulting in,

$$\mu_n\phi_n = \frac{1}{M}SS^T\phi_n = \hat{R}_M \phi_n \quad i \in M. \quad (\text{B.30})$$

The eigenvalues $\{\mu_n\}$ for \hat{C}_M correspond exactly to the non-zero eigenvalues $\{\lambda_n\}$ of \hat{R}_M , but the computational requirement for \hat{C}_M is much smaller, as for any practical problem $M \ll N$. The relationship of the empirical eigenvectors $\{\psi_n\}$ and the eigenvectors $\{\phi_n\}$ of \hat{C}_M are given as $\phi_n = S\psi_n$.

Appendix C. Full-Potential Equation

The derivation in this appendix is an expansion of the work presented by Shankar, et al. (33). This expansion shows a full step-by-step development of the discretized equations used in this method. The full-potential equation is an approximation to the Euler equations for which the flow is assumed to be irrotational, free of entropy production (36). The potential equation has one fluid variable, Ψ , defined as,

$$u = \frac{\partial \Psi}{\partial x} \quad (\text{C.1})$$

$$v = \frac{\partial \Psi}{\partial y} \quad (\text{C.2})$$

where u and v are the fluid velocity components (Note that ϕ is typically used as the potential variable but has already been assigned in this document). In a 2-D, body-fitted coordinate system represented by $\tau = t$, $\xi = \xi(x, y, t)$, and $\eta = \eta(x, y, t)$, the unsteady full-potential equation is written as

$$\left(\frac{\rho}{J}\right)_\tau + \left(\frac{\rho U}{J}\right)_\xi + \left(\frac{\rho V}{J}\right)_\eta = 0, \quad (\text{C.3})$$

where the $(R)_\xi$ refers to the derivative of R with respect to ξ . U and V are the contravariant velocities, J is the Jacobian of the metrics ($J = \xi_x \eta_y - \xi_y \eta_x$) and the density, ρ , is represented as

$$\rho = \left\{ 1 - \frac{\gamma - 1}{2} M_\infty^2 [2\Psi_\tau + (U + \xi_\tau) \Psi_\xi + (V + \eta_\tau) \Psi_\eta - 1] \right\}^{\frac{1}{\gamma - 1}}. \quad (\text{C.4})$$

The contravariant velocities are defined as follows:

$$U = \xi_\tau + a_{11} \Psi_\xi + a_{12} \Psi_\eta, \quad (\text{C.5})$$

$$V = \eta_\tau + a_{12} \Psi_\xi + a_{22} \Psi_\eta. \quad (\text{C.6})$$

The transformation grid metrics a_{11} , a_{11} , and a_{11} are defined as:

$$a_{11} = \xi_x^2 + \xi_y^2 \quad (\text{C.7})$$

$$a_{22} = \eta_x^2 + \eta_y^2, \quad (\text{C.8})$$

$$a_{12} = \xi_x \eta_x + \xi_y \eta_y. \quad (\text{C.9})$$

The equations above can be solved by a variety of schemes. The scheme selected was developed by Shankar, et, al.(33) and has the benefits of being very stable and easy to implement with POD. It uses an implicit Newton's method to solve Eqn. C.3, in discrete form, for a robust and efficient numerical solver with effective treatment of boundary conditions. In summary, the scheme is as follows: Eqn. C.3 is represented as

$$F(\Psi) = 0, \quad (\text{C.10})$$

where Ψ is the unknown to be solved for at every grid point in the domain for time step $(n+1)$. The Newton iteration for the solution to Eqn. C.10 is,

$$F(\Psi_*) + \left(\frac{\partial F}{\partial \Psi} \right)_{\Psi=\Psi_*} (\Psi - \Psi_*) = 0, \quad (\text{C.11})$$

where Ψ_* is the current guess for Ψ at the $(n+1)$ time step. At convergence (typically less than 10^{-6}), $\Delta\Psi \equiv \Psi - \Psi_*$ will approach zero.

The time derivative, $\left(\frac{\rho}{J}\right)_\tau$, and spatial derivatives, $\left(\frac{\rho U}{J}\right)_\xi$ and $\left(\frac{\rho V}{J}\right)_\eta$, must be treated in a manner consistent with the Newton iteration of Eqn. C.11. The method assumes that any variable may be expressed as a deviation from an assumed state, $f = f(\Psi_*) + \left(\frac{\partial f}{\partial \Psi}\right)_{\Psi=\Psi_*} \Delta\Psi$.

C.1 Treatment of $\left(\frac{\rho}{J}\right)_\tau$

A first-order time discretization is applied,

$$\left(\frac{\rho}{J}\right)_\tau = \frac{\left(\frac{\rho}{J}\right)_{i,j}^{n+1} - \left(\frac{\rho}{J}\right)_{i,j}^n}{\Delta\tau}, \quad (\text{C.12})$$

where $\Delta\tau$ is the change in time from step (n) to $(n+1)$, and (i,j) are the grid-point coordinates. The unknown in Eqn. C.12 is ρ^{n+1} , and can be evaluated in a time-linearized

manner similar to Eqn. C.11:

$$\rho = \rho(\Psi_*) + \left(\frac{\partial \rho}{\partial \Psi} \right)_{\Psi=\Psi_*} \Delta \Psi. \quad (\text{C.13})$$

The differential operator, $\left(\frac{\partial \rho}{\partial \Psi} \right)_{\Psi=\Psi_*}$, can be derived as follows:

$$\left(\frac{\partial \rho}{\partial \Psi} \right)_{\Psi=\Psi_*} \Delta \Psi_\tau = \frac{\partial \rho}{\partial \Psi_\tau} \Delta \Psi_\tau + \frac{\partial \rho}{\partial \Psi_\xi} \Delta \Psi_\xi + \frac{\partial \rho}{\partial \Psi_\eta} \Delta \Psi_\eta. \quad (\text{C.14})$$

Assuming the grid metrics, ξ_τ and, η_τ are small, then:

$$\frac{\partial \rho}{\partial \Psi_\tau} = -\frac{1}{\gamma-1} \left\{ 1 - \frac{\gamma-1}{2} M_\infty^2 [2\Psi_\tau + (U + \xi_\tau) \Psi_\xi + (V + \eta_\tau) \Psi_\eta - 1] \right\}^{\frac{1}{\gamma-1}-1} \frac{\gamma-1}{2} M_\infty^2 2, \quad (\text{C.15})$$

$$\frac{\partial \rho}{\partial \Psi_\xi} = -\frac{1}{\gamma-1} \left\{ 1 - \frac{\gamma-1}{2} M_\infty^2 [2\Psi_\tau + (U + \xi_\tau) \Psi_\xi + (V + \eta_\tau) \Psi_\eta - 1] \right\}^{\frac{1}{\gamma-1}-1} \frac{\gamma-1}{2} U, \quad (\text{C.16})$$

$$\frac{\partial \rho}{\partial \Psi_\eta} = -\frac{1}{\gamma-1} \left\{ 1 - \frac{\gamma-1}{2} M_\infty^2 [2\Psi_\tau + (U + \xi_\tau) \Psi_\xi + (V + \eta_\tau) \Psi_\eta - 1] \right\}^{\frac{1}{\gamma-1}-1} \frac{\gamma-1}{2} V. \quad (\text{C.17})$$

This results in:

$$\frac{\partial \rho}{\partial \Psi_\tau} = -M_\infty^2 \frac{\rho}{\rho^{\gamma-1}}, \quad (\text{C.18})$$

$$\frac{\partial \rho}{\partial \Psi_\xi} = -\frac{\rho}{\rho^{\gamma-1}} \frac{M_\infty^2}{2} U, \quad (\text{C.19})$$

$$\frac{\partial \rho}{\partial \Psi_\eta} = -\frac{\rho}{\rho^{\gamma-1}} \frac{M_\infty^2}{2} V. \quad (\text{C.20})$$

The speed of sound can be defined as, $a = \sqrt{\frac{\rho^{\gamma-1}}{M_\infty^2}}$, resulting in:

$$\frac{\partial \rho}{\partial \Psi_\tau} = -\frac{\rho}{a^2}, \quad (\text{C.21})$$

$$\frac{\partial \rho}{\partial \Psi_\xi} = -\frac{\rho}{2a^2} U, \quad (\text{C.22})$$

$$\frac{\partial \rho}{\partial \Psi_\eta} = -\frac{\rho}{2a^2} V. \quad (\text{C.23})$$

The time derivative is approximated by $\frac{1}{\Delta t}$, and eliminating the constant, 2, results in a final form that is evaluated at $\Psi = \Psi_*$ for the ρ, J, U , and V terms:

$$(\rho)_{i,j}^{n+1} = \rho(\Psi_*) + \left[-\frac{\rho}{a^2} \left(\frac{1}{\Delta \tau} + U \frac{\partial}{\partial \xi} + V \frac{\partial}{\partial \eta} \right) \right]_{\Psi=\Psi_*} \Delta \Psi. \quad (\text{C.24})$$

It may be differentiated using second-order, central-space operators on the half grid point:

$$(\rho)_{i,j}^{n+1} = \rho(\Psi_*) + \left[-\frac{\rho(\Psi_*)_{i,j}}{a(\Psi_*)_{i,j}^2} \left(\begin{array}{c} \frac{\Delta \Psi_{i,j}}{\Delta \tau} + \\ U(\Psi_*)_{i,j} \frac{(\Delta \Psi_{i+1,j} - \Delta \Psi_{i-1,j})}{2} + \\ V(\Psi_*)_{i,j} \frac{(\Delta \Psi_{i,j+1} - \Delta \Psi_{i,j-1})}{2} \end{array} \right) \right]. \quad (\text{C.25})$$

Finally the time derivative is determined to be:

$$\left(\frac{\rho}{J} \right)_\tau = \left[\frac{1}{\Delta \tau} \left(\frac{\rho(\Psi_*)}{J} \right)_{i,j} - \frac{1}{\Delta \tau} \left(\frac{\rho}{J} \right)_{i,j}^n - \left(\frac{\rho(\Psi_*)}{J \Delta \tau^2 a(\Psi_*)^2} \right)_{i,j} \left(\begin{array}{c} \frac{\Delta \Psi_{i,j}}{\Delta \tau} + \\ U(\Psi_*)_{i,j} \frac{(\Delta \Psi_{i+1,j} - \Delta \Psi_{i-1,j})}{2} + \\ V(\Psi_*)_{i,j} \frac{(\Delta \Psi_{i,j+1} - \Delta \Psi_{i,j-1})}{2} \end{array} \right) \right]. \quad (\text{C.26})$$

This is reduced to:

$$\left(\frac{\rho}{J} \right)_\tau = - \left(\frac{\rho(\Psi_*)}{J \Delta \tau a(\Psi_*)^2} \right)_{i,j} \left[\begin{array}{c} \left(\frac{J \Delta \tau^2 a(\Psi_*)^2}{\rho(\Psi_*)} \right)_{i,j} \left[\left(\frac{\rho(\Psi_*)}{J} \right)_{i,j} - \left(\frac{\rho}{J} \right)_{i,j}^n \right] + \\ \Delta \Psi_{i,j} - U(\Psi_*)_{i,j} \Delta \tau \frac{(\Delta \Psi_{i+1,j} - \Delta \Psi_{i-1,j})}{2} - \\ V(\Psi_*)_{i,j} \Delta \tau \frac{(\Delta \Psi_{i,j+1} - \Delta \Psi_{i,j-1})}{2} \end{array} \right]. \quad (\text{C.27})$$

The factor, $\left(\frac{\rho(\Psi_*)}{J \Delta \tau a(\Psi_*)^2} \right)_{i,j}$, that appears in Eqn. C.27 is used in the later development of the Approximate Factorization.

C.2 Treatment of $\left(\frac{\rho U}{J} \right)_\xi$

Again, using the Newton procedure from Eqn. C.11, the spatial derivative $\left(\frac{\rho U}{J} \right)_\xi$ is factored as:

$$\left(\frac{\rho U}{J} \right)_\xi = \frac{\partial}{\partial \xi} \left(f + \frac{\partial f}{\partial \Psi} \Delta \Psi \right), \quad (\text{C.28})$$

where:

$$f = \left(\frac{\rho U}{J} \right)_{\Psi=\Psi_*}. \quad (\text{C.29})$$

By chain rule,

$$\frac{\partial f}{\partial \Psi} = \frac{1}{J} \left(\rho \frac{\partial U}{\partial \Psi} + U \frac{\partial \rho}{\partial \Psi} \right), \quad (\text{C.30})$$

where $\frac{\partial \rho}{\partial \Psi}$ is given by Eqn. C.15 and $\frac{\partial U}{\partial \Psi}$ is developed as follows:

$$\frac{\partial U}{\partial \Psi} = \frac{\partial U}{\partial \Psi_\tau} \Delta \Psi_\tau + \frac{\partial U}{\partial \Psi_\xi} \Delta \Psi_\xi + \frac{\partial U}{\partial \Psi_\eta} \Delta \Psi_\eta, \quad (\text{C.31})$$

$$\frac{\partial U}{\partial \Psi} = a_{11} \Delta \Psi_\xi + a_{12} \Delta \Psi_\eta. \quad (\text{C.32})$$

For mixed flows, where elliptical and hyperbolic regions coexist, the inclusion of $\frac{\partial \rho}{\partial \Psi}$ leads to a pentadiagonal matrix. To preserve a tridiagonal form for efficient matrix inversion, the term $U \frac{\partial \rho}{\partial \Psi}$ appearing in Eqn. C.30 is neglected. This is acceptable in that $U \frac{\partial \rho}{\partial \Psi}$ is multiplied by $\Delta \Psi$ which approaches zero. This results in the spatial derivative term,

$$\left(\frac{\rho U}{J} \right)_\xi = \frac{\partial}{\partial \xi} \left[\left(\rho \frac{U}{J} \right)_{\Psi=\Psi_*} + \frac{\rho}{J} \left(\frac{\partial U}{\partial \Psi} \right) \Delta \Psi \right]. \quad (\text{C.33})$$

This expands to:

$$\left(\frac{\rho U}{J} \right)_\xi = \frac{\partial}{\partial \xi} \left\{ \frac{\rho(\Psi_*)}{J} \left[U(\Psi_*) + a_{11} \frac{\partial \Delta \Psi}{\partial \xi} + a_{12} \frac{\partial \Delta \Psi}{\partial \eta} \right] \right\}. \quad (\text{C.34})$$

Substituting the definition of $U(\Psi_*)$ yields:

$$\left(\frac{\rho U}{J} \right)_\xi = \frac{\partial}{\partial \xi} \left\{ \frac{\rho(\Psi_*)}{J} \left[\xi_\tau + a_{11} (\Psi_* + \Delta \Psi)_\xi + a_{12} (\Psi_* + \Delta \Psi)_\eta \right] \right\}. \quad (\text{C.35})$$

The spatial terms are differences using second-order, central difference operators on the half grid-points,

$$\left(\frac{\rho U}{J} \right)_\xi = \left(\frac{\rho U}{J} \right)_{i+\frac{1}{2},j}^{n+1} - \left(\frac{\rho U}{J} \right)_{i-\frac{1}{2},j}^{n+1}. \quad (\text{C.36})$$

Numerically, the flux terms are calculated in a single sweep and the $i + \frac{1}{2}, j$ points. After substitution, the spatial derivative becomes:

$$\left(\frac{\rho U}{J}\right)_{i+\frac{1}{2},j}^{n+1} = \left(\frac{\rho(\Psi_*)}{J}\right)_{i+\frac{1}{2},j}^{n+1} \left[\begin{aligned} &(\xi_\tau)_{i+\frac{1}{2},j} + (a_{11})_{i+\frac{1}{2},j} [(\Psi_{*i+1,j} - \Psi_{*i,j}) + (\Delta\Psi_{i+1,j} - \Delta\Psi_{i,j})] \\ &+ \frac{(a_{12})_{i+\frac{1}{2},j}}{4} (\Psi_{*i+1,j+1} + \Psi_{*i,j+1} - \Psi_{*i+1,j-1} - \Psi_{*i,j-1}) \\ &+ \frac{(a_{12})_{i+\frac{1}{2},j}}{4} (\Delta\Psi_{i+1,j+1} + \Delta\Psi_{i,j+1} - \Delta\Psi_{i+1,j-1} - \Delta\Psi_{i,j-1}) \end{aligned} \right]^{n+1} \quad (C.37)$$

C.3 Treatment of $\left(\frac{\rho V}{J}\right)_\eta$

The treatment of $\left(\frac{\rho V}{J}\right)_\eta$ is similar to the treatment of $\left(\frac{\rho U}{J}\right)_\xi$, resulting in

$$\left(\frac{\rho V}{J}\right)_\eta = \frac{\partial}{\partial \eta} \left\{ \frac{\rho(\Psi_*)}{J} \left[\eta_\tau + a_{12}(\Psi_* + \Delta\Psi)_\xi + a_{22}(\Psi_* + \Delta\Psi)_\eta \right] \right\}. \quad (C.38)$$

This is differentiated into:

$$\left(\frac{\rho V}{J}\right)_{i,j+\frac{1}{2}}^{n+1} = \left(\frac{\rho(\Psi_*)}{J}\right)_{i,j+\frac{1}{2}}^{n+1} \left[\begin{aligned} &(\eta_\tau)_{i,j+\frac{1}{2}} + (a_{22})_{i,j+\frac{1}{2}} [(\Psi_{*i,j+1} - \Psi_{*i,j}) + (\Delta\Psi_{i,j} - \Delta\Psi_{i,j+1})] \\ &+ \frac{(a_{12})_{i,j+\frac{1}{2}}}{4} (\Psi_{*i+1,j+1} + \Psi_{*i+1,j} - \Psi_{*i-1,j+1} - \Psi_{*i-1,j}) \\ &+ \frac{(a_{12})_{i,j+\frac{1}{2}}}{4} (\Delta\Psi_{i+1,j+1} + \Delta\Psi_{i+1,j} - \Delta\Psi_{i-1,j+1} - \Delta\Psi_{i-1,j}) \end{aligned} \right]^{n+1} \quad (C.39)$$

C.4 Summary of Solution $\left(\frac{\rho}{J}\right)_\tau + \left(\frac{\rho U}{J}\right)_\xi + \left(\frac{\rho V}{J}\right)_\eta = 0$

The overall solution is obtained by substituting the above equations in the Newton iterative equation,

$$F(\Psi_*) + \left(\frac{\partial F}{\partial \Psi}\right)_{\Psi=\Psi_*} (\Delta\Psi) = 0. \quad (C.40)$$

$$\left(\frac{\partial F}{\partial \Psi}\right)(\Delta\Psi) = \begin{bmatrix} \Delta\Psi_{i+1,j+1} \\ \Delta\Psi_{i+1,j} \\ \Delta\Psi_{i+1,j-1} \\ \Delta\Psi_{i,j+1} \\ \Delta\Psi_{i,j} \\ \Delta\Psi_{i,j-1} \\ \Delta\Psi_{i-1,j+1} \\ \Delta\Psi_{i-1,j} \\ \Delta\Psi_{i-1,j-1} \end{bmatrix} \begin{bmatrix} \beta \left[\left(\frac{\rho(\Psi_*)}{J}\right) \left(\frac{a_{12}}{4}\right)_{i+\frac{1}{2},j} - \left(\frac{\rho(\Psi_*)}{J}\right) \left(\frac{a_{12}}{4}\right)_{i,j+\frac{1}{2}} \right] \\ \frac{U(\Psi_*)_{i,j}\Delta\tau}{2} + \beta \left[\left(\frac{\rho(\Psi_*)}{J}\right) (a_{11})_{i+\frac{1}{2},j} + \left(\frac{\rho(\Psi_*)}{J}\right) \left(\frac{a_{12}}{4}\right)_{i,j+\frac{1}{2}} - \left(\frac{\rho(\Psi_*)}{J}\right) \left(\frac{a_{12}}{4}\right)_{i,j-\frac{1}{2}} \right] \\ \beta \left[-\left(\frac{\rho(\Psi_*)}{J}\right) \left(\frac{a_{12}}{4}\right)_{i+\frac{1}{2},j} - \left(\frac{\rho(\Psi_*)}{J}\right) \left(\frac{a_{12}}{4}\right)_{i-\frac{1}{2},j} \right] \\ \frac{V(\Psi_*)_{i,j}\Delta\tau}{2} + \beta \left[\left(\frac{\rho(\Psi_*)}{J}\right) \left(\frac{a_{12}}{4}\right)_{i+\frac{1}{2},j} - \left(\frac{\rho(\Psi_*)}{J}\right) \left(\frac{a_{12}}{4}\right)_{i-\frac{1}{2},j} + \left(\frac{\rho(\Psi_*)}{J}\right) (a_{22})_{i,j+\frac{1}{2}} \right] \\ 1 + \beta \left[-\left(\frac{\rho(\Psi_*)}{J}\right) (a_{11})_{i+\frac{1}{2},j} - \left(\frac{\rho(\Psi_*)}{J}\right) (a_{11})_{i-\frac{1}{2},j} + \left(\frac{\rho(\Psi_*)}{J}\right) (a_{22})_{i,j+\frac{1}{2}} \right] \\ -\frac{V(\Psi_*)_{i,j}\Delta\tau}{2} + \beta \left[-\left(\frac{\rho(\Psi_*)}{J}\right) \left(\frac{a_{12}}{4}\right)_{i+\frac{1}{2},j} + \left(\frac{\rho(\Psi_*)}{J}\right) \left(\frac{a_{12}}{4}\right)_{i-\frac{1}{2},j} + \left(\frac{\rho(\Psi_*)}{J}\right) (a_{22})_{i,j-\frac{1}{2}} \right] \\ \beta \left[-\left(\frac{\rho(\Psi_*)}{J}\right) \left(\frac{a_{12}}{4}\right)_{i-\frac{1}{2},j} - \left(\frac{\rho(\Psi_*)}{J}\right) \left(\frac{a_{12}}{4}\right)_{i+\frac{1}{2},j} \right] \\ -\frac{U(\Psi_*)_{i,j}\Delta\tau}{2} + \beta \left[\left(\frac{\rho(\Psi_*)}{J}\right) (a_{11})_{i-\frac{1}{2},j} - \left(\frac{\rho(\Psi_*)}{J}\right) \left(\frac{a_{12}}{4}\right)_{i,j+\frac{1}{2}} - \left(\frac{\rho(\Psi_*)}{J}\right) \left(\frac{a_{12}}{4}\right)_{i,j-\frac{1}{2}} \right] \\ \beta \left[\left(\frac{\rho(\Psi_*)}{J}\right) \left(\frac{a_{12}}{4}\right)_{i-\frac{1}{2},j} + \left(\frac{\rho(\Psi_*)}{J}\right) \left(\frac{a_{12}}{4}\right)_{i,j-\frac{1}{2}} \right] \end{bmatrix} \quad (C.41)$$

$$F(\Psi_*) = \begin{bmatrix} \Psi_{*i+1,j+1} \\ \Psi_{*i+1,j} \\ \Psi_{*i+1,j-1} \\ \Psi_{*i,j+1} \\ \Psi_{*i,j} \\ \Psi_{*i,j-1} \\ \Psi_{*i-1,j+1} \\ \Psi_{*i-1,j} \\ \Psi_{*i-1,j-1} \\ 1 \end{bmatrix} \beta \begin{bmatrix} \left[\left(\frac{\rho(\Psi_*)}{J} \right) \left(\frac{a_{12}}{4} \right)_{i+\frac{1}{2},j} - \left(\frac{\rho(\Psi_*)}{J} \right) \left(\frac{a_{12}}{4} \right)_{i,j+\frac{1}{2}} \right] \\ \left[\left(\frac{\rho(\Psi_*)}{J} \right) (a_{11})_{i+\frac{1}{2},j} + \left(\frac{\rho(\Psi_*)}{J} \right) \left(\frac{a_{12}}{4} \right)_{i,j+\frac{1}{2}} - \left(\frac{\rho(\Psi_*)}{J} \right) \left(\frac{a_{12}}{4} \right)_{i,j-\frac{1}{2}} \right] \\ \left[- \left(\frac{\rho(\Psi_*)}{J} \right) \left(\frac{a_{12}}{4} \right)_{i+\frac{1}{2},j} - \left(\frac{\rho(\Psi_*)}{J} \right) \left(\frac{a_{12}}{4} \right)_{i-\frac{1}{2},j} \right] \\ \left[\left(\frac{\rho(\Psi_*)}{J} \right) \left(\frac{a_{12}}{4} \right)_{i+\frac{1}{2},j} - \left(\frac{\rho(\Psi_*)}{J} \right) \left(\frac{a_{12}}{4} \right)_{i-\frac{1}{2},j} + \left(\frac{\rho(\Psi_*)}{J} \right) (a_{22})_{i,j+\frac{1}{2}} \right] \\ \left[- \left(\frac{\rho(\Psi_*)}{J} \right) (a_{11})_{i+\frac{1}{2},j} - \left(\frac{\rho(\Psi_*)}{J} \right) (a_{11})_{i-\frac{1}{2},j} + \left(\frac{\rho(\Psi_*)}{J} \right) (a_{22})_{i,j+\frac{1}{2}} \right] \\ \left[- \left(\frac{\rho(\Psi_*)}{J} \right) \left(\frac{a_{12}}{4} \right)_{i+\frac{1}{2},j} + \left(\frac{\rho(\Psi_*)}{J} \right) \left(\frac{a_{12}}{4} \right)_{i-\frac{1}{2},j} + \left(\frac{\rho(\Psi_*)}{J} \right) (a_{22})_{i,j-\frac{1}{2}} \right] \\ \left[- \left(\frac{\rho(\Psi_*)}{J} \right) \left(\frac{a_{12}}{4} \right)_{i-\frac{1}{2},j} - \left(\frac{\rho(\Psi_*)}{J} \right) \left(\frac{a_{12}}{4} \right)_{i+\frac{1}{2},j} \right] \\ \left[\left(\frac{\rho(\Psi_*)}{J} \right) (a_{11})_{i-\frac{1}{2},j} - \left(\frac{\rho(\Psi_*)}{J} \right) \left(\frac{a_{12}}{4} \right)_{i,j+\frac{1}{2}} - \left(\frac{\rho(\Psi_*)}{J} \right) \left(\frac{a_{12}}{4} \right)_{i,j-\frac{1}{2}} \right] \\ \left[\left(\frac{\rho(\Psi_*)}{J} \right) \left(\frac{a_{12}}{4} \right)_{i-\frac{1}{2},j} + \left(\frac{\rho(\Psi_*)}{J} \right) \left(\frac{a_{12}}{4} \right)_{i,j-\frac{1}{2}} \right] \\ \frac{1}{\Delta\tau} \left[\left(\frac{\rho(\Psi_*)}{J} \right)_{i,j} - \left(\frac{\rho}{J} \right)_{i,j}^n \right] \end{bmatrix}. \quad (\text{C.42})$$

where $\beta = \left(-\frac{J\Delta\tau a(\Psi_*)^2}{\rho(\Psi_*)} \right)_{i,j}$.

C.5 Approximate Factorization

The Jacobian matrix, $\left(\frac{\partial F}{\partial \Psi} \right)$, is large ($N \times N$) but sparse and can be simplified using an approximate factorization creating two linear operators,

$$L_\xi = \left[1 + \Delta\tau U \frac{\partial}{\partial \xi} + \left(-\frac{J\Delta\tau^2 a(\Psi_*)^2}{\rho(\Psi_*)} \right) \frac{\partial}{\partial \xi} \left(a_{11} \frac{\rho}{J} \frac{\partial}{\partial \xi} \right) \right], \quad (\text{C.43})$$

$$L_\eta = \left[1 + \Delta\tau V \frac{\partial}{\partial \eta} + \left(-\frac{J\Delta\tau^2 a(\Psi_*)^2}{\rho(\Psi_*)} \right) \frac{\partial}{\partial \eta} \left(a_{22} \frac{\rho}{J} \frac{\partial}{\partial \eta} \right) \right], \quad (\text{C.44})$$

where L_ξ and L_η are $(N \times N)$ tridiagonal matrices that are solved with successive ξ and η sweeps

$$L_\xi L_\eta \Delta \Psi = R, \quad (\text{C.45})$$

$$L_\xi \overline{\Delta \Psi} = R, \quad (\text{C.46})$$

$$L_\eta \Delta \Psi = \overline{\Delta \Psi}, \quad (\text{C.47})$$

where $\overline{\Delta \Psi}$ is an intermediate solution and $R = F(\Psi_*)$ from Eqn. C.11.

The linear operators are discretized in a fashion similar to the full development with second-order, central difference operators on the half grid points:

$$L_\xi \Delta \Psi = \Delta \Psi + \Delta \tau U \frac{\partial}{\partial \xi} \Delta \Psi + \left(-\frac{J \Delta \tau^2 a (\Psi_*)^2}{\rho (\Psi_*)} \right) \left(\frac{\partial}{\partial \xi} a_{11} \frac{\rho}{J} \frac{\partial}{\partial \xi} \Delta \Psi + a_{11} \frac{\rho}{J} \frac{\partial^2}{\partial \xi^2} \Delta \Psi \right), \quad (C.48)$$

$$L_\xi \Delta \Psi = \left[\begin{aligned} & \Delta \Psi_{i,j} + \frac{\Delta \tau U}{2} (\Delta \Psi_{i+1,j} - \Delta \Psi_{i-1,j}) \\ & + \left(-\frac{J \Delta \tau^2 a (\Psi_*)^2}{\rho (\Psi_*)} \right) \left(\begin{aligned} & \frac{1}{2} \left(\left(a_{11} \frac{\rho}{J} \right)_{i+1,j} - \left(a_{11} \frac{\rho}{J} \right)_{i-1,j} \right) \frac{1}{2} (\Delta \Psi_{i+1,j} - \Delta \Psi_{i-1,j}) \\ & + \left(a_{11} \frac{\rho}{J} \right)_{i,j} (\Delta \Psi_{i+1,j} - 2\Delta \Psi_{i,j} + \Delta \Psi_{i-1,j}) \end{aligned} \right) \end{aligned} \right], \quad (C.49)$$

$$L_\eta \Delta \Psi = \Delta \Psi + \Delta \tau V \frac{\partial}{\partial \eta} \Delta \Psi + \left(-\frac{J \Delta \tau^2 a (\Psi_*)^2}{\rho (\Psi_*)} \right) \left(\frac{\partial}{\partial \eta} a_{22} \frac{\rho}{J} \frac{\partial}{\partial \eta} \Delta \Psi + a_{22} \frac{\rho}{J} \frac{\partial^2}{\partial \eta^2} \Delta \Psi \right), \quad (C.50)$$

$$L_\eta \Delta \Psi = \left[\begin{aligned} & \Delta \Psi_{i,j} + \frac{\Delta \tau V}{2} (\Delta \Psi_{i,j+1} - \Delta \Psi_{i,j-1}) \\ & + \left(-\frac{J \Delta \tau^2 a (\Psi_*)^2}{\rho (\Psi_*)} \right) \left(\begin{aligned} & \frac{1}{2} \left(\left(a_{22} \frac{\rho}{J} \right)_{i,j+1} - \left(a_{22} \frac{\rho}{J} \right)_{i,j-1} \right) \frac{1}{2} (\Delta \Psi_{i,j+1} - \Delta \Psi_{i,j-1}) \\ & + \left(a_{22} \frac{\rho}{J} \right)_{i,j} (\Delta \Psi_{i,j+1} - 2\Delta \Psi_{i,j} + \Delta \Psi_{i,j-1}) \end{aligned} \right) \end{aligned} \right], \quad (C.51)$$

C.6 Boundary Conditions

The boundary conditions are broken into three groups: far-field, body surface, and unsteady wake .

C.6.1 Far-Field. The far-field boundary condition uses Riemann invariants that correspond to the positive characteristics with respect to the inward normal. Thus, for the inflow, outflow and far field boundary the positive characteristics are:

$$\frac{U}{\sqrt{a_{11}}} + \frac{2}{\gamma - 1} a = \text{const}, \quad (C.52)$$

$$-\frac{U}{\sqrt{a_{11}}} + \frac{2}{\gamma - 1} a = \text{const}, \quad (C.53)$$

$$-\frac{V}{\sqrt{a_{22}}} + \frac{2}{\gamma - 1} a = \text{const}. \quad (C.54)$$

These can be differentiated with respect to Ψ :

$$\frac{1}{\sqrt{a_{11}}} \frac{\partial U}{\partial \Psi} + \frac{2}{\gamma - 1} \frac{\partial a}{\partial \Psi} = 0, \quad (C.55)$$

$$-\frac{1}{\sqrt{a_{11}}} \frac{\partial U}{\partial \Psi} + \frac{2}{\gamma - 1} \frac{\partial a}{\partial \Psi} = 0, \quad (C.56)$$

$$-\frac{1}{\sqrt{a_{22}}} \frac{\partial V}{\partial \Psi} + \frac{2}{\gamma - 1} \frac{\partial a}{\partial \Psi} = 0. \quad (C.57)$$

Substituting the derivatives for $\frac{\partial U}{\partial \Psi}$ and $\frac{\partial a}{\partial \Psi}$, and setting the residual to the difference in the freestream and the calculated value at the boundary yields,

$$\left[\begin{aligned} & \frac{1}{\sqrt{a_{11}}} \left(a_{11} \frac{\partial}{\partial \xi} + a_{12} \frac{\partial}{\partial \eta} \right) \Delta \Psi + \frac{2}{\gamma-1} \left(\frac{1}{\Delta \tau} + U \frac{\partial}{\partial \xi} + V \frac{\partial}{\partial \eta} \right) \Delta \Psi \\ & = \left(\frac{U}{\sqrt{a_{11}}} + \frac{2}{\gamma-1} a \right)_{freestream} - \left(\frac{U}{\sqrt{a_{11}}} + \frac{2}{\gamma-1} a \right) \end{aligned} \right], \quad (C.58)$$

$$\left[\begin{aligned} & -\frac{1}{\sqrt{a_{11}}} \left(a_{11} \frac{\partial}{\partial \xi} + a_{12} \frac{\partial}{\partial \eta} \right) \Delta \Psi + \frac{2}{\gamma-1} \left(\frac{1}{\Delta \tau} + U \frac{\partial}{\partial \xi} + V \frac{\partial}{\partial \eta} \right) \Delta \Psi \\ & = \left(-\frac{U}{\sqrt{a_{11}}} + \frac{2}{\gamma-1} a \right)_{freestream} - \left(-\frac{U}{\sqrt{a_{11}}} + \frac{2}{\gamma-1} a \right) \end{aligned} \right], \quad (C.59)$$

$$\left[\begin{aligned} & -\frac{1}{\sqrt{a_{22}}} \left(a_{12} \frac{\partial}{\partial \xi} + a_{22} \frac{\partial}{\partial \eta} \right) \Delta \Psi + \frac{2}{\gamma-1} \left(\frac{1}{\Delta \tau} + U \frac{\partial}{\partial \xi} + V \frac{\partial}{\partial \eta} \right) \Delta \Psi \\ & = \left(-\frac{V}{\sqrt{a_{22}}} + \frac{2}{\gamma-1} a \right)_{freestream} - \left(-\frac{V}{\sqrt{a_{22}}} + \frac{2}{\gamma-1} a \right) \end{aligned} \right]. \quad (C.60)$$

The scheme is discretized using first-order forward or backward differences for the normal derivatives and second-order central differences for the parallel derivatives,

Inflow/Outflow:

$$\left[\begin{aligned} & \frac{2}{(\gamma-1)\Delta \tau} \Delta \Psi_{i,j} + \left(\pm \frac{a_{11}}{\sqrt{a_{11}}} + U \right) \frac{(\Delta \Psi_{i+1,j} + \Delta \Psi_{i,j})}{2} + \left(\pm \frac{a_{12}}{\sqrt{a_{11}}} + V \right) \frac{(\Delta \Psi_{i,j+1} + \Delta \Psi_{i,j-1})}{2} \\ & = \left(\pm \frac{U}{\sqrt{a_{11}}} + \frac{2}{\gamma-1} a \right)_{freestream} - \left(\pm \frac{U}{\sqrt{a_{11}}} + \frac{2}{\gamma-1} a \right) \end{aligned} \right] \quad (C.61)$$

Far Field:

$$\left[\begin{aligned} & \frac{2}{(\gamma-1)\Delta \tau} \Delta \Psi_{i,j} + \left(-\frac{a_{12}}{\sqrt{a_{22}}} + U \right) \frac{(\Delta \Psi_{i+1,j} + \Delta \Psi_{i+1,j})}{2} + \left(-\frac{a_{22}}{\sqrt{a_{22}}} + V \right) \frac{(\Delta \Psi_{i,j+1} + \Delta \Psi_{i,j})}{2} \\ & = \left(\frac{V}{\sqrt{a_{22}}} + \frac{2}{\gamma-1} a \right)_{freestream} - \left(\frac{V}{\sqrt{a_{22}}} + \frac{2}{\gamma-1} a \right) \end{aligned} \right] \quad (C.62)$$

C.6.2 Body. The body boundary condition requires flow tangency for inviscid flow. The contravariant velocity, V , must be zero at the body. By definition,

$$V = \eta_\tau + a_{12}\Psi_\xi + a_{22}\Psi_\eta = 0, \quad (C.63)$$

$$\Psi_\eta = -\frac{\eta_\tau}{a_{22}} - \frac{a_{12}}{a_{22}}\Psi_\xi. \quad (C.64)$$

By assuming:

$$\left(\frac{\rho V}{J} \right)_{i,j+\frac{1}{2}} = - \left(\frac{\rho V}{J} \right)_{i,j-\frac{1}{2}}, \quad (C.65)$$

where the $i, j - \frac{1}{2}$ point is a ghost point within the body, the governing equation can be modified for a body point. For the Approximate Factorization scheme, the implementation of the body boundary condition must be done in both of the linear operators, L_ξ, L_η , as well as in the right hand side term, R . The linear operators are modified as follows;

$$L_\xi = \left[1 + \Delta\tau U \frac{\partial}{\partial \xi} + \left(-\frac{J\Delta\tau^2 a(\Psi_*)^2}{\rho(\Psi_*)} \right) \frac{\partial}{\partial \xi} \left(\left(a_{11} - \frac{a_{11}^2}{a_{22}} \right) \frac{\rho}{J} \frac{\partial}{\partial \xi} \right) \right], \quad (\text{C.66})$$

$$L_\eta = \left[1 + \left(-\frac{J\Delta\tau^2 a(\Psi_*)^2}{\rho(\Psi_*)} \right) \frac{2}{\Delta\eta} \left(a_{22} \frac{\rho}{J} \frac{\partial}{\partial \eta} \right)_{i,j+\frac{1}{2}} \right]. \quad (\text{C.67})$$

They are then discretized as above. The right hand side term, R , is modified in the $\left(\frac{\rho U}{J} \right)$ term.

$$\left(\frac{\rho U}{J} \right)_\xi = \frac{\partial}{\partial \xi} \left\{ \frac{\rho(\Psi_*)}{J} \left[U(\Psi_*) + a_{11} \frac{\partial \Delta \Psi}{\partial \xi} + a_{12} \frac{\partial \Delta \Psi}{\partial \eta} \right] \right\}, \quad (\text{C.68})$$

$$\left(\frac{\rho U}{J} \right)_\xi = \frac{\partial}{\partial \xi} \left\{ \frac{\rho(\Psi_*)}{J} \left[U(\Psi_*) + a_{11} \frac{\partial \Delta \Psi}{\partial \xi} + a_{12} \left(-\frac{\eta_\tau}{a_{22}} - \frac{a_{12}}{a_{22}} \frac{\partial \Delta \Psi}{\partial \xi} \right) \right] \right\}, \quad (\text{C.69})$$

$$\left(\frac{\rho U}{J} \right)_\xi = \frac{\partial}{\partial \xi} \left\{ \frac{\rho(\Psi_*)}{J} \left[U(\Psi_*) + \left(a_{11} - \frac{a_{12}^2}{a_{22}} \right) \frac{\partial \Delta \Psi}{\partial \xi} - \frac{\eta_\tau}{a_{22}} \right] \right\}. \quad (\text{C.70})$$

The $\left(\frac{\rho V}{J} \right)$ term cancels.

C.6.3 Unsteady Wake. The wake cut behind the trailing edge of the airfoil must be properly modeled in an unsteady flow. The modeling is done through the vorticity convection equation,

$$\Gamma_t + (a_{11} \Psi_{\xi,u} - \xi_{t,l}) \Gamma_{\xi,u} + (\xi_{t,u} + \xi_{t,l}) \Psi_{\xi,u} = 0 \quad (\text{C.71})$$

where the u, l subscripts indicate upper and lower wake boundaries. The vorticity convection equation assumes that $[V\Psi_\eta] \cong 0$, where $[f]$ is the jump in the quantity f across the wake. Also, a_{12} is assumed to be zero for all wake points by proper construction of the wake grid. The vorticity equation is integrated via a direct marching scheme from the trailing edge to the outflow boundary condition. It is begun with the assumption that $\Gamma = \Psi_u - \Psi_l$ at the trailing edge. Finally, after the vorticity distribution is determined,

the lower wake potential function values are overwritten,

$$\Psi_l = \Psi_u - \Gamma \quad (\text{C.72})$$

To maintain symmetry and preserve accuracy, on every odd time count the potential function on the lower wake cut is preserved and the upper overwritten,

$$\Gamma_t + (a_{11}\Psi_{\xi,l} - \xi_{t,u})\Gamma_{\xi,l} - (\xi_{t,u} + \xi_{t,l})\Psi_{\xi,l} = 0. \quad (\text{C.73})$$

In addition to the vorticity distribution, the unsteady solution also requires Ψ_η on the wake points. This is determined via a Taylor's expansion,

$$\Psi_\eta = \frac{\Psi_\eta - \left(\Psi_\eta + \Gamma + \frac{[\Psi_{\eta\eta}]}{2}\right)}{2}, \quad (\text{C.74})$$

where:

$$[\Psi_{\eta\eta}] = -\frac{\left(\frac{\rho a_{11}\Gamma_\xi}{J}\right)_\xi}{\left(\frac{\rho a_{22}\Gamma}{J}\right)}. \quad (\text{C.75})$$

C.7 Density Biasing

All of the density terms in $\left(\frac{\rho U}{J}\right)$ and $\left(\frac{\rho V}{J}\right)$ are density biased to account for shocks. Several density biasing techniques were proposed by Shankar, et. al. The directional flux biasing was selected to provide a fully rotated solution.

$$\tilde{\rho} = \frac{1}{q} \left(\rho q \mp \Delta\xi \frac{\partial}{\partial\xi} (\rho q)^- \right), \quad (\text{C.76})$$

where q is the local total velocity and is defined to be $(\rho q)^- = \rho q - \rho^* q^*$ if $q > q^*$ and $(\rho q)^- = 0$ if $q \leq q^*$. For $U \geq 0$, the positive sign and forward differencing is used. For $U < 0$ the negative and backwards differencing is used. The quantities $\rho^* q^*$ represent sonic values of density and total velocity. These are given using the speed of sound relationships

as:

$$(q^*)^2 = \frac{1 + \frac{\gamma-1}{2} M_\infty^2 [1 - 2\Psi_\tau - 2\xi_\tau \Psi_\xi - 2\eta_\tau \Psi_\eta]}{\frac{\gamma+1}{2} M_\infty^2}, \quad (\text{C.77})$$

$$\rho^* = (q^* M_\infty)^{\frac{2}{\gamma-1}}. \quad (\text{C.78})$$

Appendix D. Validation

Validation of the Shankar full-potential code used for the full-order solver was done by comparison to experimental surface pressure data and the results of previously validated computer codes for two cases; steady flow over a 2-D stationary bump (40) and unsteady flow past a NACA 0012 airfoil (48). For additional comparison, inviscid and viscous results from the COBALT computer code (49) were compared to the steady case.

D.1 Steady Flow

The results of the Shankar code compared well with the experimental subsonic data and with the subsonic and transonic COBALT code. In the transonic cases, the Shankar code provided accurate integrated surface pressure as compared to the experimental data. The experimental data was taken for a smooth bump in the Langley rectangular high-speed wind tunnel (1952). Pressure measurements were taken for two bumps of thickness to chord ratios of 0.05 and 0.15 (Note that Lindsey and Daley list ratios of 0.1 and 0.3, but their definition of chord length is from the midpoint to leading edge). Mach numbers from 0.25 to choking flow were tested at zero angle of attack. The tunnel had a four by eighteen inch test section, with four-inch models. The tests were made on one surface of each model. The models were placed in the section together, back-to-back, assuring a zero angle of attack and dividing the channel into two separate test sections. The upper boundary was approximately 2.25 chord-lengths from the surfaces. Each model had one chord-wise row of static pressure orifices installed on the model surface at the semi-span station. The profile of the bump was made smooth such that reasonable agreement could be made between experimental data and potential flow at low speeds. The equations of the x and y coordinates of the surface were (50),

$$x = \cos \theta - \frac{t}{4} (\cos \theta - \cos 3\theta), \quad (\text{D.1})$$

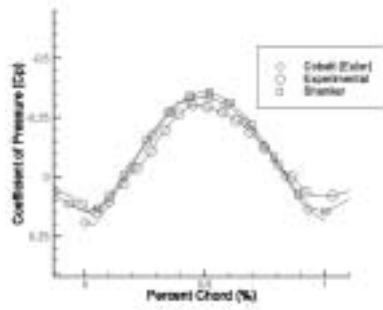
$$y = \frac{t}{4} (3 \sin \theta - \sin 3\theta), \quad (\text{D.2})$$

where θ runs from $0 - \pi$ and t is the thickness at the midpoint of the bump.

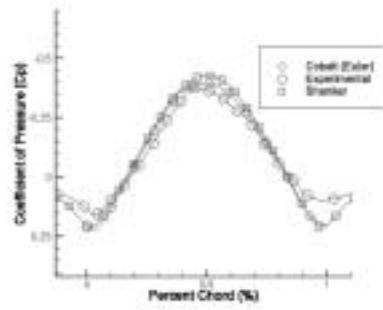
The results from the 0.05 ratio model were used for comparison to the Shankar code. The results of the Shankar code were slightly faster in maximum Mach numbers than the experimental data for the subsonic flow. This was to be expected, as the full-potential equation does not take into account the effects of viscosity. The increased velocity translated into a decrease in pressure on the surface of the bump (i.e. larger negative C_p). The same result was seen in the COBALT (Euler) cases and the two computational codes were within 5% of each other (see Fig. D.1). The fully subsonic cases show good agreement between potential, Euler, and experimental results. The subsonic profiles were symmetric for the Euler and potential codes. The experiential profile was not symmetric due to viscous effects over the rear half of the bump. At an inlet Mach of 0.759, the flow becomes transonic at the top of the bump. Both the Euler and the potential results begin to show a shock, however the experimental result does not. In the experimental results, the shockwave does not show up in pressure data until about Mach 0.789. This is due to the effects of the boundary layer altering the effective shape of the bump. At Mach numbers greater than about 0.8, the experimental flow fully separates behind peak of the bump. Therefore, it is impossible to compare the potential results to the experimental data. However, the Euler and potential results continue to be very similar (Fig. D.2).

D.2 Unsteady Flow

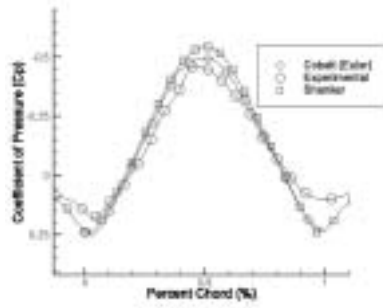
The results of the Shankar code compared well unsteady experimental NACA 0012 airfoil data. The experimental data was transonic with a weak shockwave on the body of the airfoil. Oscillation was forced in both pitch and plunge and pressure data was recorded, then converted to non-dimensional coefficient of pressure and lift coefficient. The Shankar code showed excellent comparison to the experimental data, in fully developed flow (Fig. D.3), and matched the original data presented by Shankar et. al. (33). The Shankar solver clearly reproduced the Euler results and reproduced the experiential results within the limitations of the full-potential equation.



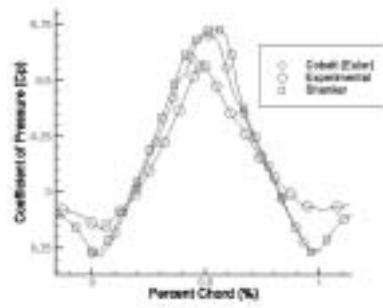
(a) Mach = 0.226



(b) Mach = 0.519

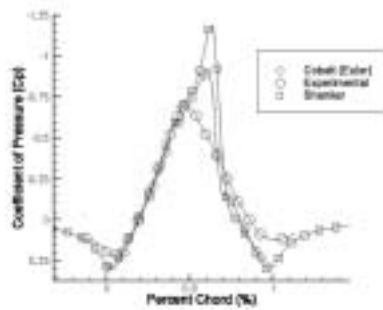


(c) Mach = 0.680

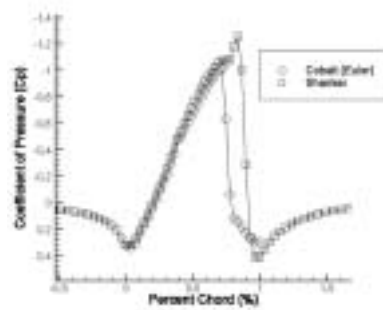


(d) Mach = 0.759

Figure D.1 Sub-Sonic Cases



(a) Mach = 0.789



(b) Mach = 0.829

Figure D.2 Trans-Sonic Cases

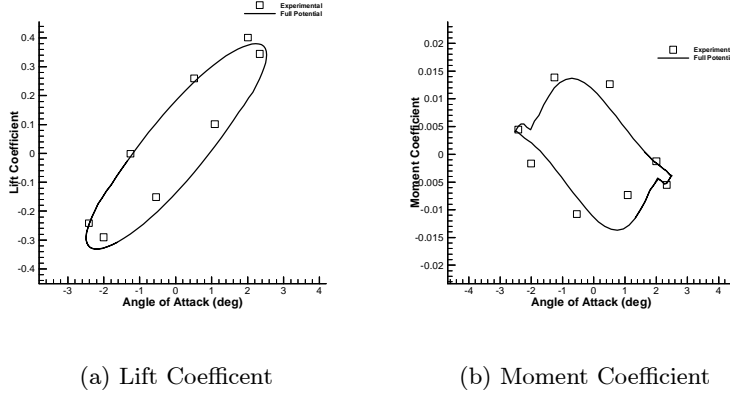


Figure D.3 Unsteady Case

Table D.1 PAPA Structural Model Parameters For Validation

x_{cg}	x_α	$\zeta_h = \zeta_\alpha$	$\frac{\bar{\omega}_h}{\bar{\omega}_\alpha}$	r_α^2	μ_s	M_∞	α_0
0.5	-0.25	0.0	0.2	0.25	125	0.8	0

D.3 Structural Model

To validate the loosely coupled structural and fluid model, flutter boundaries were evaluated for the NACA 0012 airfoil. Data from the ENS3DAE CFD code and the TVD-ntiAE CFD code were used as baselines for comparison (51). The flutter boundary was expected between $\bar{u} = 6.6$ and $\bar{u} = 7.0$. The structural parameters selected were based on those used in the references (Tbl. D.1).

Time integration was used to bracket the flutter onset speed. The results showed reasonable comparison to the TVDntiAE and ENS3DAE codes. The flutters onset speed was found to be between $\bar{u} = 6.8$ and $\bar{u} = 6.9$ (Tbl. D.2). The flutter onset stabilized after several hundred non-dimensional time units (see Fig. D.4).

Table D.2 Flutter Onset Cases

\bar{u}	Comments
6.0	Damped
6.5	Damped
7.0	LCO
6.75	Damped
6.9	LCO
6.8	Damped

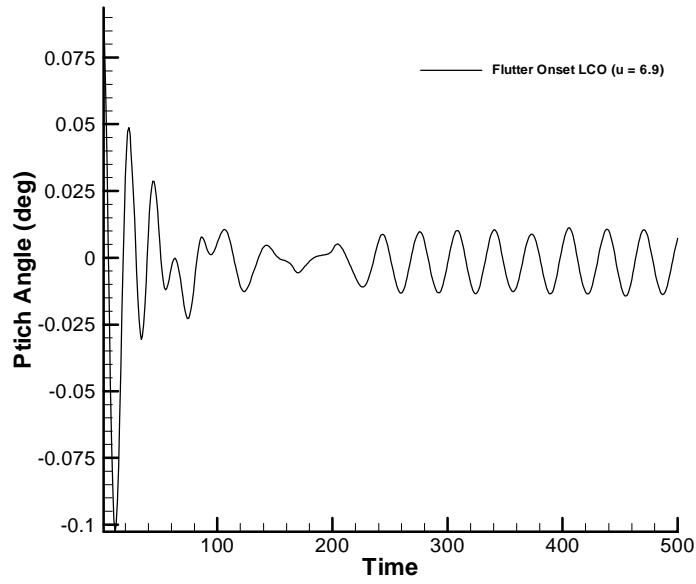


Figure D.4 Flutter Onset

Appendix E. Pitching and Plunging Airfoil Mode Shapes

The following are mode shapes for the individual POD/ROM of the Pitching and Plunging Airfoil application. They are presented for greater detail in examining the nature of the mode shapes when varying pitch, plunge or maximum angle of attack. The first four modes are presented for several different input parameters: Figs. E.1 to E.5 $h = 0$, $a = 1.0$ deg, $f = 0.02 - 0.1$, and 20 modes; Figs. E.6 to E.8 $h = 0 - 20$, $a = 1.0$ deg, $f = 0.06$, and 20 modes; Figs. E.9 to E.11 $h = 10$, $a = 0.0 - 2.0$ deg, $f = 0.06$, and 20 modes.

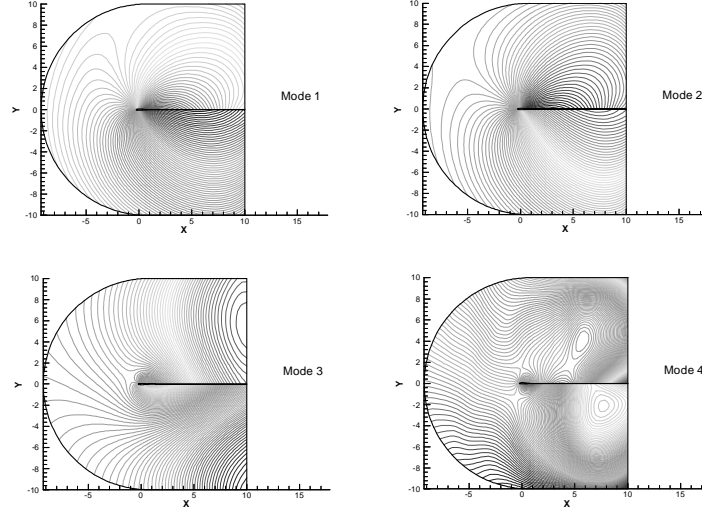


Figure E.1 Individual POD/ROM Modes ($h = 0$, $a = 1.0$ deg, $f = 0.02$, 20 modes)

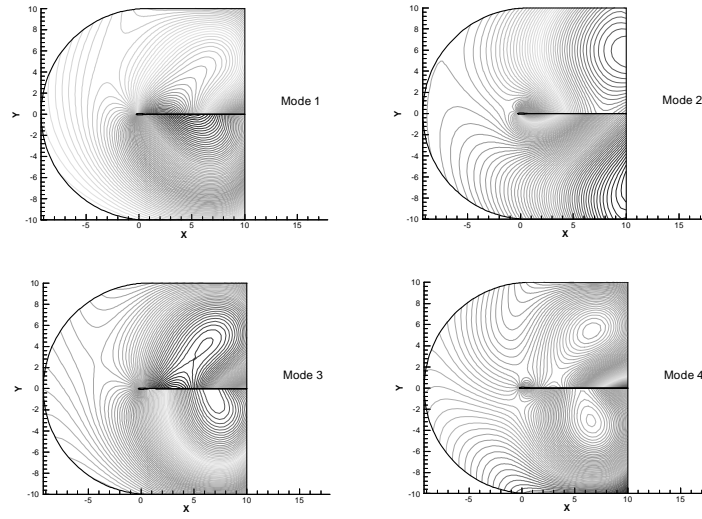


Figure E.2 Individual POD/ROM Modes ($h = 0$, $a = 1.0$ deg, $f = 0.04$, 20 modes)

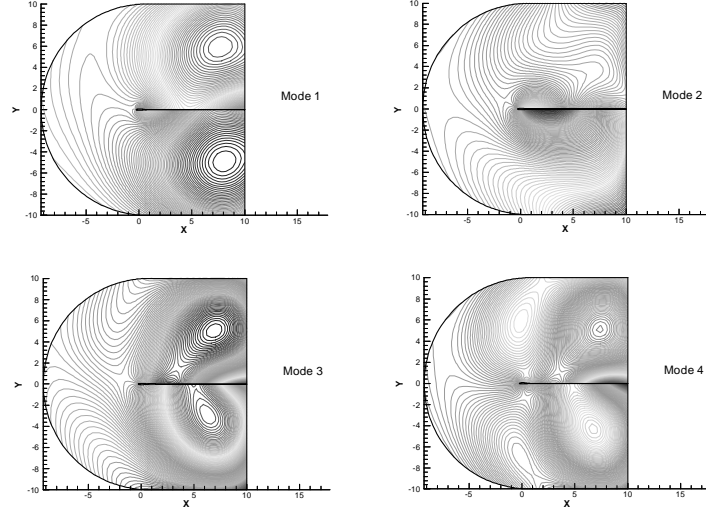


Figure E.3 Individual POD/ROM Modes ($h = 0$, $a = 1.0$ deg, $f = 0.06$, 20 modes)

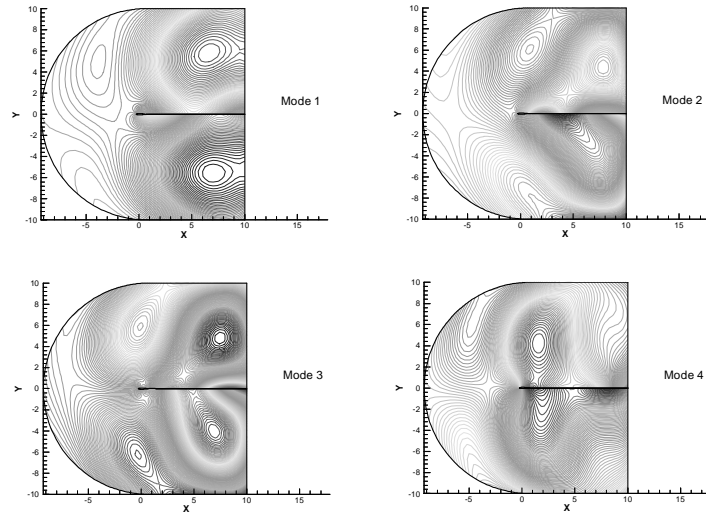


Figure E.4 Individual POD/ROM Modes ($h = 0$, $a = 1.0$ deg, $f = 0.08$, 20 modes)

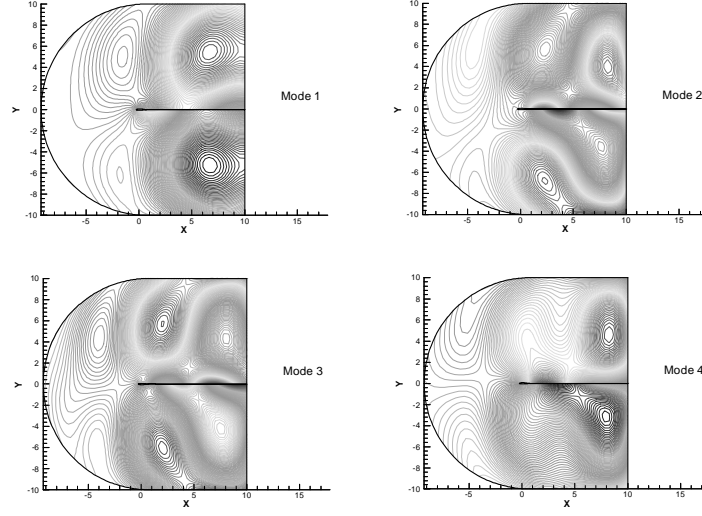


Figure E.5 Individual POD/ROM Modes ($h = 0$, $a = 1.0$ deg, $f = 0.1$, 20 modes)

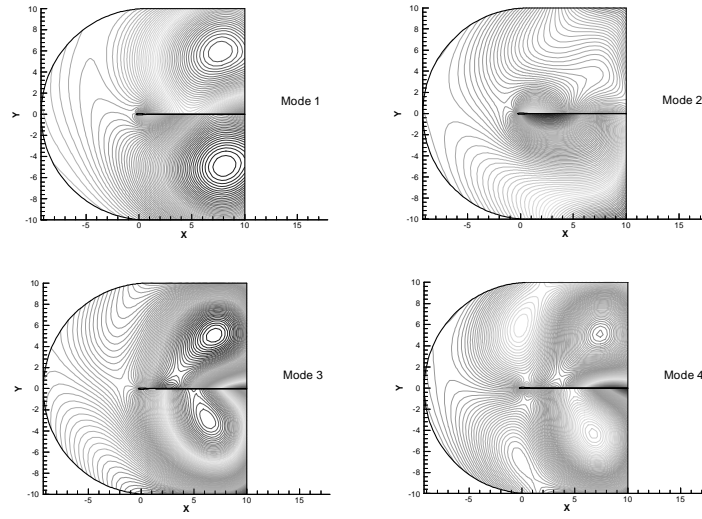


Figure E.6 Individual POD/ROM Modes ($h = 0$, $a = 1.0$ deg, $f = 0.06$, 20 modes)

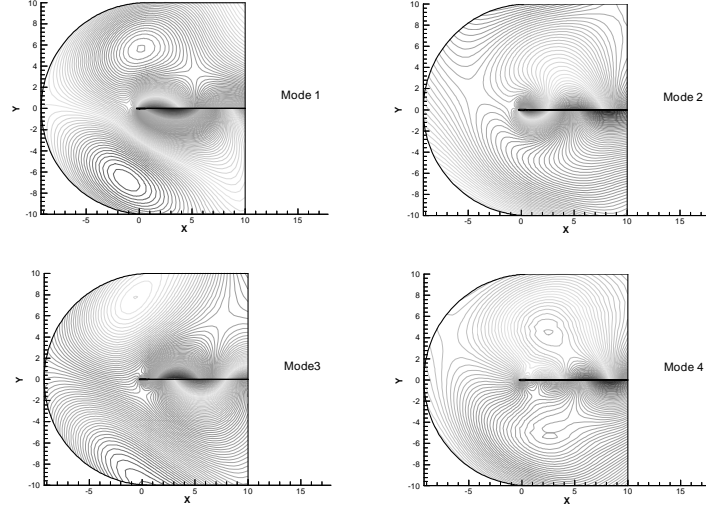


Figure E.7 Individual POD/ROM Modes ($h = 10$, $a = 1.0$ deg, $f = 0.06$, 20 modes)

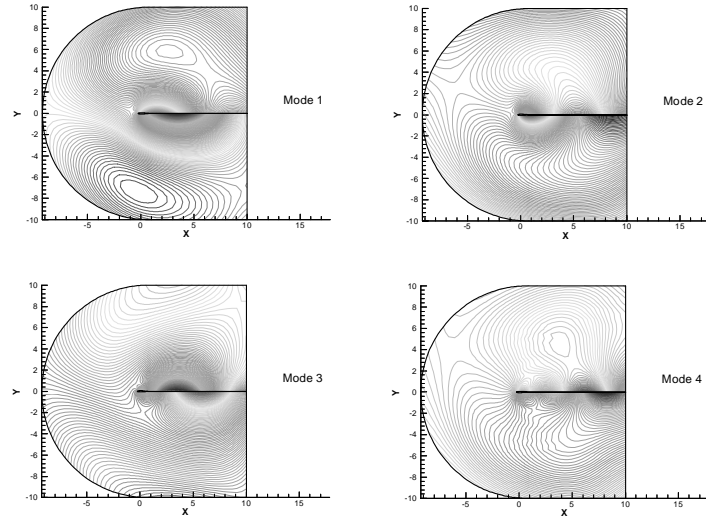


Figure E.8 Individual POD/ROM Modes ($h = 20$, $a = 1.0$ deg, $f = 0.06$, 20 modes)

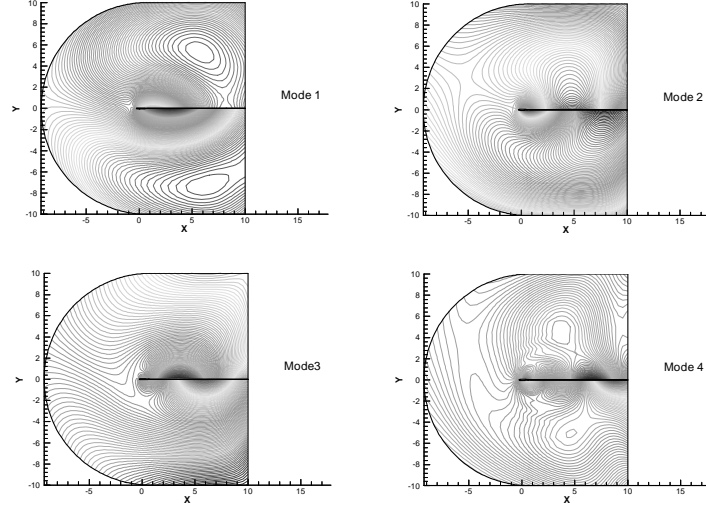


Figure E.9 Individual POD/ROM Modes ($h = 10$, $a = 0$ deg, $f = 0.06$, 20 modes)

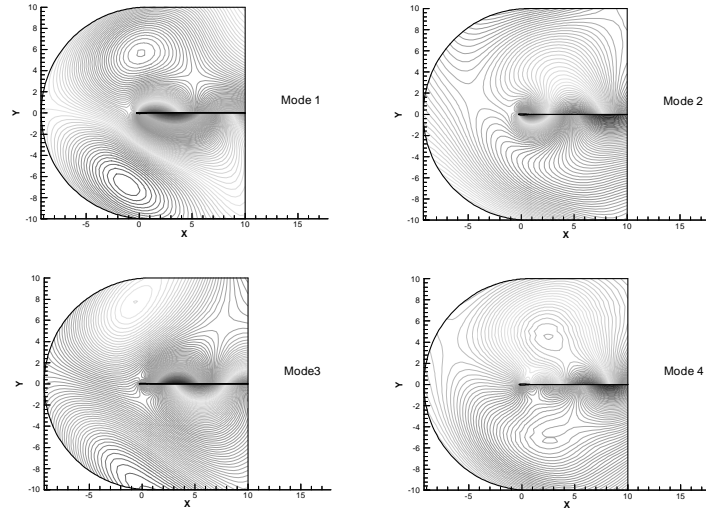


Figure E.10 Individual POD/ROM Modes ($h = 10$, $a = 1.0$ deg, $f = 0.06$, 20 modes)

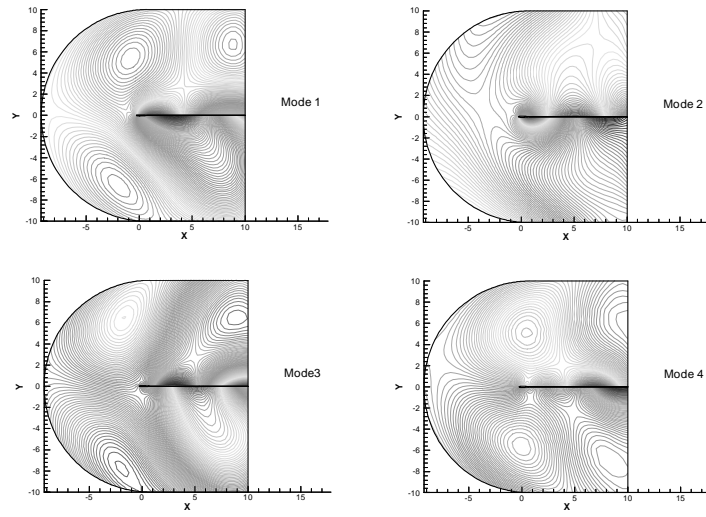


Figure E.11 Individual POD/ROM Modes ($h = 10$, $a = 2.0$ deg, $f = 0.06$, 20 modes)

Appendix F. Summary of Computational Runs

The location and nomenclature of the archived computational runs are described in this appendix. Archives are presented for each of the three model problems: Translating Cylinder, Oscillating Panel, and Pitching and Plunging Airfoil.

The Oscillating Panel zipped archives are named based on the amplitude of deflection and the percentage of deforming area, i.e. DG075100 would be a maximum amplitude $A = 0.75$ and a 100% deforming domain. Within each archive the files are broken down in the following fashion: filename_ f _.plt. The frequency of oscillation, f , is used to differentiate the separate files. Restart files are not used for the Oscillating Panel problem. The following zipped archives are stored for the Oscillating Panel problem:

- DG05100.zip
- DG075100.zip
- DG10100.zip
- DG1075.zip
- DG125100.zip
- DG15100.zip
- DG2100.zip
- DG1050.zip

To execute a particular run, the user must locate the appropriate amplitude and deforming area. Within the zipped archive, the snapshot_ f _.plt and the gridsnap_ f _.plt files must be copied into the directory with the executable. Blended runs must have their snapshot files recreated using option (3) of the executable. Multi-POD runs must have all blended snapshot files stored in the same directory and then identified during execution.

The PAPA zipped archives are named based on the amplitude of deflection, i.e. A10 would be a maximum amplitude $A = 0.1$. Within each archive the files are broken down in the following fashion: filename_ f_a _.plt. The frequency of oscillation, f , and AoA, a , is used to differentiate the separate files. Restart files are named in the following convention;

restart_ M _a_.plt, where M identifies the inlet Mach number and a the initial AoA of the airfoil. All airfoils are assumed to start at a plunge depth of $h = 0$. The following zipped archives are stored for the PAPA problem:

- A005.zip
- A010.zip
- A015.zip
- A020.zip
- RestartM0510.plt
- RestartM050.plt
- RestartM0801.plt
- RestartM0810.plt

To execute a particular run, the user must locate the appropriate amplitude and deforming area. Within the zipped archive, the snapshot_ f _a_.plt and the gridsnap_ f _a_.plt files must be copied into the directory with the executable. In addition the appropriate restart file must be copied to the same directory. Blended runs must have their snapshot files recreated using option (3) of the executable. Multi-POD runs must have all blended snapshot files stored in the same directory and then identified during execution.

The source codes are stored in separate directories, with each code variation the name of a different sub-directory. The files types are stored within the zipped archive are identified in Tbl. F.1.

An example case is stored in a separate directory, including all necessary data files and executable code. The example is a forced pitching and plunging airfoil at an oscillation frequency of 0.1, a plunge depth of 0.1, and a pitch angle of 2.0 deg. To execute the example, perform the following steps:

1. Run Unsteady.exe
2. Select option 5

Table F.1 Archived File Names and Descriptions

File Name	Description
full_x_.plt	full: Full-order results
cl_x_.plt	cl: Full-order lift (normal) coefficient values
reduced_x_.plt	reduced: POD/ROM Results
clred_x_.plt	clred: POD/ROM lift (normal) coefficient values
phifield_x_.plt	phifield: Modal matrix, Φ , plotted on the computational domain
snapshot_x_.plt	snapshot: Snapshots for individual amplitude and frequency combinations
gridsnap_x_.plt	gridsnap: Grid snapshots for individual amplitude and frequency combinations
error_x_.plt	error: Time accurate error between full-order and POD/ROM results
maxerror_x_.plt	maxerror: Peak error values over time

- (a) Select sub-option 1
 - (b) Enter initial plunge depth of 0.0
 - (c) Enter initial AoA of 0.016
 - (d) Enter restart file name of RestartM05A0016.plt
3. Select option 6
4. Select option 4
- (a) Select sub-option 1
 - (b) Select sub-option 1
 - (c) Enter snapshot file name of snapshot.plt
 - (d) Enter number of modes 25
 - (e) Select sub-option 1
 - (f) Enter number of modes 25
 - (g) Select sub-option 1
5. Select option 7
- (a) Enter number of iterations 10000
 - (b) Enter number of oscillations 10
 - (c) Enter plunge depth 0.1

- (d) Enter pitch angle 2.0
 - (e) Enter delta time 0.01
 - (f) Enter number of sub-iterations 5
 - (g) Enter accuracy of sub-iterations 0.000001
 - (h) Enter data recording spacing 500
6. Select option 99 for program end

Vita

Major John S.R. Anttonen graduated from Reedsport High School, in Reedsport, Oregon in June 1985. He entered undergraduate studies at Oregon State University in Corvallis, Oregon where he graduated with a Bachelor of Science degree in Mechanical Engineering in December 1989. While at Oregon State University, John was commissioned as a second lieutenant through the Air Force ROTC program, Detachment 685.

His first assignment was as a Missile Engineering officer for the 4393rd Civil Engineering Squadron, Vandenberg AFB, California, where he was the Mechanical design engineer in support of Minuteman II, III and Peacekeeper programs. While there, he received his Professional Engineering license in Mechanical Engineering from the State of California. In 1993, he transferred to Detachment 9, Space and Missile Systems Center (SMC), Vandenberg AFB, as the propulsion test engineer for Taurus space launch vehicle. He was assigned as the Chief of the Propulsion Test Section in 1994. John attended West Coast University, graduating in 1994 with a Master of Science degree in Engineering. In 1995, John transferred to SMC Test and Evaluation, at Kirtland AFB, New Mexico, as the Chief of Test Resources Branch. In 1996, John became the Chief of Technology Development Branch, Military Spaceplane Program Office, Phillips Laboratory, Kirtland AFB, New Mexico. In September of 1998, he entered the Graduate School of Engineering and Management, Air Force Institute of Technology. Upon graduation, he will be assigned to the Air Force Research Laboratory, Eglin AFB, Florida.

REPORT DOCUMENTATION PAGEForm Approved
OMB No. 0704-0188

Public reporting burden for this collection of information is estimated to average 1 hour per response, including the time for reviewing instructions, searching existing data sources, gathering and maintaining the data needed, and completing and reviewing the collection of information. Send comments regarding this burden estimate or any other aspect of this collection of information, including suggestions for reducing this burden to Washington Headquarters Services, Directorate for Information Operations and Reports, 1215 Jefferson Davis Highway, Suite 1204, Arlington, VA 22202-4302, and to the Office of Management and Budget, Paperwork Reduction Project (0704-0188), Washington, DC 20503.

PLEASE DO NOT RETURN YOUR FORM TO THE ABOVE ADDRESS.

1. REPORT DATE (DD-MM-YYYY) 01102001		2. REPORT TYPE Dissertation		3. DATES COVERED Sep 1999 - Oct 2001	
4. TITLE AND SUBTITLE Techniques for Reduced Order Modeling of Aeroelastic Structures with Deforming Grids				5a. CONTRACT NUMBER	
				5b. GRANT NUMBER	
				5c. PROGRAM ELEMENT NUMBER	
6. AUTHOR(S) John Anttonen				5d. PROJECT NUMBER	
				5e. TASK NUMBER	
				5f. WORK UNIT NUMBER	
7. PERFORMING ORGANIZATION NAME(S) AND ADDRESS(ES) Air Force Institute of Technology AFIT/ENY 2950 P St, Bldg 640 Wright-Patterson AFB, OH 45433-7531				8. PERFORMING ORGANIZATION REPORT NUMBER AFIT/DS/ENY01-01	
9. SPONSORING/MONITORING AGENCY NAME(S) AND ADDRESS(ES) Air Force Research Laboratory Bldg. 146, 2210 8th Street Wright-Patterson AFB, OH 45433-7531				10. SPONSOR/MONITOR'S ACRONYM(S) AFRL/VASD	
				11. SPONSOR/MONITOR'S REPORT NUMBER(S)	
12. DISTRIBUTION/AILABILITY STATEMENT Distrubution Unlimited					
13. SUPPLEMENTARY NOTES					
14. ABSTRACT Reduced order modeling (ROM) seeks to make the modeling of aeroelastic behavior practical by reducing computation time for design codes. Deforming grids are often used in aeroelastic problems to account for the deformation of the structure. Proper Orthogonal Decomposition (POD/ROM) is a ROM technique that operates in an index-space for computations, not accounting for changes in grid dynamics, and must be modified to reflect grid deformation properly. To investigate and account for the effects of grid deformation on POD/ROM, a new algorithm is developed that incorporates modifications to the usual formulation. Evaluation of the new algorithm is accomplished through application to three fluid-structure models, each adding an increased level of grid dynamics. Deforming grid POD/ROMs are found to require more modes for an accurate solution than POD/ROM for rigidly moving grids. In addition, for deforming grids, POD/ROMs are less accurate when the grid deformation is significantly altered from the deformations seen in the development of the POD/ROM. A technique, called Multi-POD, is developed that evaluates the relative grid motion between how the POD/ROM is created and how it is executed. The Multi-POD technique determines the current relative grid deformation and selects the best POD/ROM from those available.					
15. SUBJECT TERMS Proper Orthogonal Decomposition, POD, Reduced Order Modeling, ROM, POD/ROM, Deforming Grids					
16. SECURITY CLASSIFICATION OF:			17. LIMITATION OF ABSTRACT	18. NUMBER OF PAGES	19a. NAME OF RESPONSIBLE PERSON
a. REPORT	b. ABSTRACT	c. THIS PAGE			Paul King
U	U	U	UP	157	19b. TELEPHONE NUMBER (Include area code) 937-255-3636 x 4628